

Stony Brook University



OFFICIAL COPY

The official electronic file of this thesis or dissertation is maintained by the University Libraries on behalf of The Graduate School at Stony Brook University.

© All Rights Reserved by Author.

Multiscale Particle-Based Modeling of Mechanotransduction Process in Flow-Induced Platelet Activation using Dissipative Particle Dynamics and Coarse Grained Molecular Dynamics

A Dissertation Presented

by

Chao Gao

to

The Graduate School

in Partial Fulfillment of the

Requirements

for the Degree of

Doctor of Philosophy

in

Biomedical Engineering

Stony Brook University

December 2016

Copyright by
Chao Gao
2016

Stony Brook University

The Graduate School

Chao Gao

We, the dissertation committee for the above candidate for the

Doctor of Philosophy degree, hereby recommend

acceptance of this dissertation.

Danny Bluestein, Ph.D. – Dissertation Advisor
Professor of Biomedical Engineering

Wei Yin, Ph.D. - Chairperson of Defense
Assistant Professor of Biomedical Engineering

Gabor Balazsi, Ph.D.
Associate Professor of Biomedical Engineering

Robert J. Harrison, Ph.D.
Professor of Applied Mathematics and Statistics

This dissertation is accepted by the Graduate School

Nancy Goroff

Interim Dean of the Graduate School

Abstract of the Dissertation

Multiscale Particle-Based Modeling of Mechanotransduction in Flow-Induced Platelet Activation using Dissipative Particle Dynamics and Coarse-Grained Molecular Dynamics

by

Chao Gao

Doctor of Philosophy

in

Biomedical Engineering

Stony Brook University

2016

Thrombosis in cardiovascular diseases and prosthetic cardiovascular devices can be potentiated by pathological flow patterns that enhance hemostatic responses including platelet activation, aggregation, and adhesion. Platelets upon activation react to pathological shear stresses with complex biochemical and morphological changes, aggregate, and adhere to blood vessels or device surfaces to form thrombi.

Computational modeling and simulation are extensively employed to study the shear-induced platelet activation. Numerical simulations of this complex process based on Computational Fluid Dynamics (CFD) treat blood as a continuum and solve the Navier-Stokes equations to resolve the process to μm scales level. Due to the limited scales range, CFD is not able to address the subsequent biomechanical interactions of blood's individual constituents, and molecular mechanisms governing platelet activation which occur at the nm scales.

To bridge the gap from the 10 nm to the 100 μm between cellular/molecular scales and macroscopic flow scales, this dissertation presents a novel multiscale modeling approach based on discrete particle methods that permits the investigation of such complex phenomena by coupling the macroscopic flow conditions with the cellular and molecular effects of platelet activation. The multiscale approach incorporates (i) top scale blood plasma model with DPD method, with length scales down to μm , where multiple platelets – each composed of an ensemble of particles – are suspended in a discrete particle medium with viscous fluid properties; and (ii) bottom scale platelet

model employing CGMD method down to *nm* scale, in which platelet with multiple sub-components (actin filaments cytoskeleton, bilayer membrane, and cytoplasm) evolves during activation characterized by pseudopodia formation and shape change. The fully interactive micro-nano multiscale model transmits the mechanical stress across the scales: individual platelet is activated in response to fluid shear stress at the bottom scale, where the actin filaments exposed to the highest mechanical stresses elongate and induce pseudopodia formation; the blood plasma dynamics at the top scale is then affected by the activated platelet with morphological changes. Aided with state-of-the-art HPC techniques, this multiscale shear-induced platelet activation model offers a significant contribution to elucidate the underlying mechanisms of thrombus formation agonized by mechanical stimuli.

Table of contents

Table of contents	v
List of Figures	viii
List of Tables	xiii
Vita	xiv
List of Publications	xv
Acknowledgements	xviii
I. Introduction	1
1.1 Fluid-shear induced platelet activation	1
1.2 Numerical modeling of blood flow based on multiscale approach	4
1.3 Dissertation outline	7
II. Modeling platelet suspensions flowing through stenotic microchannel	9
2.1 Introduction	9
2.2 Methods	10
2.2.1 Modeling viscous fluids with DPD	10
2.2.2 Study of fluid flow properties using counter-Poiseuille flow	11
2.2.3 Development of no-slip boundary condition in 3D complex geometries	13
2.2.4 Modeling platelet suspensions through 3D stenotic microchannel	15
2.2.5 Development of inflow-outflow boundary condition	16
2.2.6 Parallel performance measurement on supercomputers	19
2.3 Results	22
2.3.1 Viscous fluid flow properties under counter-Poiseuille flow	22
2.3.2 Fluid development with no-slip boundary condition	25
2.3.3 Platelet suspensions in stenotic microchannel	26
2.3.4 Validation of DPD viscous fluid flow dynamics under inflow/outflow BC	27
2.3.5 Performance analysis of DPD fluid flow through five geometries	30
2.4 Discussion and conclusions	32
III. Improving the compressible effect of DPD-based blood flow simulations through severe stenotic microchannel	35

3.1	Introduction-----	35
3.2	Methods-----	36
3.2.1	DPD-Morse fluid model-----	36
3.2.2	Parameterization of DPD-Morse potential using counter-Poiseuille flow-----	38
3.2.3	Stenotic microchannel simulations with no-slip boundary condition-----	42
3.2.4	Two-dimensional continuum fluid simulation -----	44
3.2.5	Unit conversion from dimensionless to physical units -----	45
3.3	Results -----	45
3.3.1	Fluid flow properties in counter-Poiseuille flow -----	46
3.3.2	Fluid flow properties in the 67% stenotic microchannel flow-----	46
3.3.3	Platelet transport dynamics in 67% stenotic microchannel flow -----	52
3.3.4	Fluid stress accumulation along platelet flowing trajectory -----	56
3.4	Discussion and conclusions-----	58
IV.	Modeling blood plasma-platelet interaction using multiscale DPD-CGMD approach-----	61
4.1	Introduction-----	61
4.2	Methods-----	62
4.2.1	Fluid-platelet interaction model -----	62
4.2.2	Platelet flipping dynamics under shear flow-----	63
4.2.3	Platelet surface stress analysis -----	66
4.2.4	Physical unit conversion-----	68
4.3	Results -----	71
4.3.1	Viscous blood plasma modeling-----	71
4.3.2	Platelet flipping dynamics -----	72
4.3.3	Effects of platelet deformability on platelet flipping dynamics-----	74
4.3.4	Effects of platelet deformability on platelet membrane surface stress distribution ($\theta = 0$) --	77
4.3.5	Spatial-temporal averaging -----	78
4.4	Discussion and conclusions-----	80
V.	Multiscale model of shear-induced platelet activation-----	83
5.1	Introduction-----	83
5.2	Methods-----	84
5.2.1	Multiscale platelet mechanotransduction model-----	84
5.2.2	Cytoskeleton stress accumulation-----	86

5.2.3	Pseudopodia formation -----	87
5.2.4	Validation by in-vitro experiment-----	90
5.3	Results -----	90
5.3.1	Shear-induced platelet activation-----	90
5.3.2	Morphological analysis of pseudopodia formation -----	93
5.4	Discussion and conclusions-----	95
VI.	Conclusions and future work-----	98
	References-----	103
	Appendix – build, run, and debug LAMMPS -----	110

List of Figures

Figure I-1. Shear-induced platelet activation at multiple spatial-temporal scales. CFD covers mm in length and seconds in time. DPD covers 1 μm to 100 μm in length and μs to ms in time. CGMD covers nm to μm in length and ns to μs in time.....	4
Figure II-1. Schematic of implementation of no-slip boundary condition. (a) Particles within one cutoff distance to the wall are subject to extra DPD forces arising from the interactions between real and fictitious particles. The repulsive force is included to mimic the existence of fluid particles outside of computational domain. The addition of dissipative and random forces aims to create an equilibrated shear layer across the wall such that no-slip boundary condition is achieved at the wall. (b to d) Particles moving across the wall are reflected back with specular reflection.....	14
Figure II-2. Stenotic microchannel constructed with triangular wall elements. A fine mesh is imposed on stenotic region with large curvature, and coarse mesh on straight cylindrical region.	15
Figure II-3. Coarse grained platelet model with 444 particles, with pairwise DPD interaction and bond potential between the connected particles, as well as dihedral potentials between neighboring triangular elements. (a) Platelet model in ellipsoidal shape; (b) Schematic of bond and dihedral potentials with bond length r_{23} and dihedral angle ϕ_{1234}	16
Figure II-4. 2D schematic of three-dimensional inflow/outflow BC model. The upstream, middle, and downstream fluid particles are illustrated in RGB color. Periodic boundary condition is applied to both upstream and downstream domains. Inflow/outflow boundary condition is applied to the middle fluid domain.	18
Figure II-5. Schematic of boundary force enforcement in imaginary flow domain and middle fluid domain. (a) Imaginary flow domain: region A and B include particles within one cutoff distance from the periodic boundary. Ghost particles are copied from A to A' and from B to B' to interact with real fluid particles on the opposite side. (b) Middle fluid domain: particles within one cutoff distance to the inlet/outlet interact with upstream/downstream fluid particles.....	19
Figure II-6. Implementation of no-slip boundary condition. The boundary condition profile is loaded to the root processor with rank 0, and is broadcasted to the rest of processors. Each processor loops its local particles and determines if it resides inside any specific triangles.....	20
Figure II-7. Wall geometries for five simulation cases, 50%, 75%, 150%, C, and S shapes.....	22
Figure II-8. Determination of μ through numerical fitting method.	23
Figure II-9. Velocity, shear stress and density profiles developed with periodic Poiseuille flow under different body forces (dots – numerical simulations, lines – exact solutions). The DPD fluids breaks down in approximating incompressible fluid flow as the Reynolds number reaches 750 - though the velocity profile still matches the analytical solution, shear stress is badly estimated and mild density gradient develops.	24

Figure II-10. Poiseuille and Couette flow development in channels enclosed by solid walls. (a) Velocity development of two types of fluid flows. (b) Schematic of simulation setup with upper and lower walls.	25
Figure II-11. Flow development in stenotic microchannel. Fully developed flow is achieved at 100, 000 time steps. (a) Cross-section view ($z = 0$) of velocity profile. Averaged velocity profile at upstream (b), stenotic (c), and downstream (d) region in $z = 0$ plane.	26
Figure II-12. Platelet suspension through stenotic microchannel. No-slip boundary condition is imposed on the walls, and periodic boundary condition on inlet and outlet. (a) Construction of stenotic microchannel; (b) Snapshot of platelet suspension in stenotic microchannel.	27
Figure II-13. Fluid velocity and density plot in x-y cross section of fluid domain. Left column: inflow/outflow BC is applied; fluid domain is between the dotted lines at $x = 5$ and $x = 30$; P represents the upstream and downstream periodic domain. Right column: periodic BC is applied on entire fluid domain.	28
Figure II-14. Fluid velocity plot in x-z plane at three distinct locations along flow direction, $x = 10$, $x = 17.5$, and $x = 25$. Upper row represents fluid velocity in domain with applied inflow/outflow BC. Lower row represents results from periodic BC simulation.	29
Figure II-15. Fluid pressure gradient and shear stress along flow direction for inflow/outflow and periodic fluid domain. A linear pressure gradient results from addition of inflow/outflow BC, whereas a flat pressure gradient comes from periodic BC. The shear stress distribution is the same for both cases.	30
Figure II-16. Fully developed velocity profile for five geometries.	31
Figure II-17. Speedup and strong scalability for five geometries with system size 1 million and 10 million.	31
Figure III-1. Velocity (left) and pressure (right) distribution of DPD-Morse fluid under counter-Poiseuille flow.	40
Figure III-2. Counter-Poiseuille flow of DPD and DPD-Morse fluids. The system dimensions are $30 \times 30 \times 30$, number density $n=3.0$. A body force $g_y = \pm 2.0$ is applied along the y direction. The system is divided into 60 vertical bins along the x direction with side length of 0.5, and fluid particle velocity, number density, shear stress, and pressure are averaged in each bin for 5000 timesteps after the flow is fully developed (all numbers appear in dimensionless units).	41
Figure III-3. Stenotic microchannel of $120 \mu\text{m}$ length, $30 \mu\text{m}$ height, and $0 \mu\text{m}$ width. The upstream is $44 \mu\text{m}$ in length, $30 \mu\text{m}$ in height, and $30 \mu\text{m}$ in width; the downstream section has the same dimensions as the upstream section; the stenotic section is $32 \mu\text{m}$ in length, $10 \mu\text{m}$ in height, and $30 \mu\text{m}$ in width. The fluid flow is along x direction driven by a body force g_x . No-slip boundary condition is applied on the top walls composed of 10 triangular elements, and the bottom walls with 2 triangular elements. The platelet is modeled as a rigid ellipsoid particle with dimensions of $4 \times 4 \times 2 \mu\text{m}$	44
Figure III-4. No-slip boundary condition for the DPD-Morse fluid. Fluid velocities and number densities are shown at five time points: 82.62, 165.24, 247.86, 330.48 and 413.1 μs . The velocity	

profiles are compared to the analytical solution (blue solid line). The blood plasma density is 1060 kg/m³. 48

Figure III-5. Fluid density comparison of the DPD and the DPD-Morse fluids in 67% stenotic microchannel. (a) and (b) show an xy cross-section of the fluid density of the DPD-Morse and the DPD fluids, correspondingly. (c) shows the observations of fluid density gradient along flow direction at y=5.5, where the blue line represents the DPD fluid, and the red line represents the DPD-Morse fluid. 49

Figure III-6. Velocity comparison of CFD, DPD-Morse, and DPD fluids in the 67% stenotic microchannel. (a-c) represent xy cross-section view of velocity v_x of the three fluid models. (d) shows the velocity change long flow direction at y=5.5 (green (CFD), red (DPD-Morse), and blue (DPD))..... 50

Figure III-7. Fluid viscosity change along a platelet flow trajectory in reference to blood plasma viscosity of 1.197 mPa·s (the blue and red lines represent the DPD and DPD-Morse fluids, respectively.). The mean squared error for the DPD-Morse fluid is 0.08, and for the DPD fluid is 0.39..... 51

Figure III-8. Shear stress comparison of the CFD, DPD-Morse and DPD fluids in the 67% stenotic microchannel. (a-c) represent xy cross-section of the shear stress of the three fluid models. (c) shows the shear stress change along the flow direction at y=5.5. (green (CFD), red (DPD-Morse), and blue (DPD))..... 52

Figure III-9. (a) shows the x-component of platelet flowing velocity vx. (b) shows the platelet transport trajectory and (c) y-component of platelet flowing velocity vy. 54

Figure III-10. Snapshots of platelet passing through the stenotic microchannel at different time points. The red platelet is immersed in the DPD-Morse fluid, and the yellow one in the DPD fluid. At 0 ms (i.e., the first subplot), the red and yellow platelets are overlapped..... 55

Figure III-11. (a) Scalar fluid stress along the platelet flow trajectory in the DPD and DPD-Morse fluids. (b) Fluid stress accumulation (SA) along the platelet flow trajectory. 57

Figure IV-1. Simulation setup to study platelet flipping dynamics under linear shear flow. Parallel flow chamber is constructed with upper and lower walls moving in opposite directions. The platelet is positioned at the center..... 64

Figure IV-2. Platelet rotation: (a) along z axis, where ϕ is the deviated angle with respect to x axis; (b) along x axis, where θ is the deviated angle with respect to z axis; (c) along y axis, where ψ is the deviated angle with respect to x axis. Shear flow is applied in x-y plane along x direction. 65

Figure IV-3. Platelet flipping in x-y plane with (a) $\theta = 0$ and (b) $\theta = \frac{\pi}{2}$. Rotation angle ϕ is monitored as a function of time. 65

Figure IV-4. Mesh network of rigid and deformable platelet membrane. 68

Figure IV-5. Blood plasma viscosity as a function of dissipative parameter γ and cutoff distance rc, measured with counter-Poiseuille flow method. (a) viscosity versus γ when rc = 1.0; (b) viscosity versus rc when $\gamma = 90$ 72

Figure IV-6. Flipping angle ϕ as a function of dimensionless time γt in half flipping period. (a) effect of σ_{LJ} on ϕ . When $\sigma_{LJ} > 1.0$, platelet does not flip under shear flow; when $\sigma_{LJ} < 0.4$, fluid particles penetrate into platelet through membrane. σ_{LJ} is selected finally to be 0.6. (b) effect of ε_{LJ} on ϕ . An increase of ε_{LJ} leads to a closer match to analytical solution. The closest match is achieved when $\varepsilon = 6$. (c) effect of γ_{DPD} on ϕ . (d) effect of r_c on ϕ . γ_{DPD} and r_c do not have impact of platelet flipping. 73

Figure IV-7. (a) Platelet flipping in linear shear flow. (b) Angular velocity $\phi_{\gamma t}$ vs. the strain γt for Jeffery's orbits and numerical solutions using the rigid and deformable platelet models. (c) Angular acceleration $\phi_{\gamma t}$ vs. the strain γt for Jeffery's orbits and numerical solutions using the rigid and deformable platelet models. 74

Figure IV-8. Platelet surface velocity profile during flipping. Top row: rigid platelet model. Bottom row: deformable platelet model. The velocity profiles at five discrete time points are illustrated, 70 μs , 140 μs , 210 μs , 280 μs and 350 μs . The maximum velocity on platelet surface for both cases is approximately 1.125 cm/s. Rigid platelet flips faster than deformable platelet. Bending of membrane is observed in deformable platelet model. 75

Figure IV-9. Platelet surface velocity distribution at $\theta = \frac{\pi}{2}$. (a) Rigid platelet. (b) Deformable platelet. 76

Figure IV-10. Platelet surface stress distribution. (a) 3D perspective. (b) 2D perspective. In both (a) and (b), top row: rigid platelet model, bottom row: deformable platelet model. Higher stress is observed in membrane of rigid platelet model, with maximum value approximately 1000 $dyne/cm^2$ 77

Figure IV-11. Coarse-graining effect along spatial and temporal scales. Rows represent spatial coarse-graining, where the first row is the velocity profile based the original membrane construction, and second to fourth row are averaged velocity profile on a coarse-grained platelet membrane. Columns represent temporal coarse-graining, where the first column is the description on 1 ns, and the last column presents velocity profile on 10 μs 79

Figure V-1. Atom types of platelet. The platelet is viewed from above its top surface. Type 1 is the cytoplasm, type 2 and 3 are membrane, type 4 to 14 are cytoskeleton, and type 15 are fluids. In cytoskeleton construction, only backbone particles play a role in pseudopodia formation. 86

Figure V-2. One cytoskeleton filament of platelet. Helical structure is based on polypeptide chain. The tip starts with Nitrogen atom, and repeats in a pattern of N-CA-C. The dynamics of the filament is governed by bond, angle and dihedral potentials. 88

Figure V-3. Shear-induced platelet activation process. The platelet flips and deforms under linear shear flow with 85.76 $dyne/cm^2$. The stress accumulation of 44 actin filaments is computed during 1.1 ms simulations, and five filaments with most highest values are selected for protrusion (filament No. 7, 12, 19, 34, and 43). The protrusible actin filaments transit from initial helical structure to elongated filaments to induce pseudopodia formation. 91

Figure V-4. Illustration of platelet activation model. (a) Cytoskeleton with five elongated actin filaments. (b) A single protrusible filament. (c) Whole activated platelet model with five pseudopodia. (d) Description of actin network composed of non-protrusible filaments..... 92

Figure V-5. Two pseudopodia formation on top and bottom surfaces of platelet. The pseudopodia lengths are 0.567 and 0.422 μm , respectively. The diameter of platelet remains 4 μm 93

Figure V-6. (a) Time-lapse sequence of two pseudopodia formation (arrowheads). The platelet membrane initially maintains ellipsoidal shape (0 us). Two microspikes protrude from platelet membrane (0.24 us), continue to elongate and transit to short pseudopodia (0.24 to 1.44 us). Bars, 1 μm . (b) Pseudopodia growth length. Microspikes form as result of initial protrusion of actin filament bundles (0.2 to 0.3 μm). Withdrawal is observed during the protrusion process (lower pseudopodia). Microspikes then transit to pseudopodia formation with end length of 0.5 to 0.6 μm .
..... 94

List of Tables

Table 1. Blood flow properties through cardiovascular system and prosthetic devices	2
Table 2. Number of particles and triangular elements.....	21
Table 3. Reference units used in the DPD simulations; model parameters and translation of various input and output data from the dimensionless to real units.....	71
Table 4. Platelet spatial coarse-graining level.....	78

Vita

Education

M.S., Biomedical Engineering, Stony Brook University, NY, USA, 2012.

B.E., Biomedical Engineering, Northeastern University, Liaoning, China, 2010.

Experience

Graduate Research Assistant, Stony Brook University. 09/2011 to 12/2016

Graduate Teaching Assistant, Stony Brook University. 08/2010 to 05/2011

Conference Presentations

2nd IEEE International Conference on High Performance and Smart Computing (HPSC 2016), New York, NY, April 9-10, 2016.

BME Annual Research Symposium Podium Presentation, Dept. of Biomedical Engineering, Stony Brook University, Sep. 2015.

BME Annual Research Symposium Poster Presentation, Dept. of Biomedical Engineering, Stony Brook University, Sep. 2014.

Doctoral Research Showcase on SC13 - The International Conference for High Performance Computing, Networking, Storage and Analysis, Denver, CO.

Podium presentation on 2013 Biomedical Engineering Society Annual Meeting, Seattle, WA.

Podium presentation on 2012 Biomedical Engineering Society Annual Meeting, Atlanta, GA.

Awards

Tianhe-2 HPC Resource Award (20,000 core-hours), Guangzhou, China, 2015.

Best poster presentation, BME Annual Graduate Research Symposium, Stony Brook, NY, 2014.

IACS Travel Award, SC13 Doctoral Research Showcase, Denver, CO, 2013.

List of Publications

Peer-Reviewed Journal Publications

- **Gao, C.**, Zhang, P., Marom, G., Deng, Y., Bluestein, D., “Reducing the effects of compressibility in DPD-based blood flow simulations through severe stenotic microchannel.” (to be submitted)
- Zhang, P., **Gao, C.**, Sheriff, J., Zhang, N., Zhang, L., Slepian, M., Deng, Y., Bluestein, D., “A Predictive Multiscale Model for Simulating Flow-Induced Platelet Activation: Correlating Numerical Simulations with In Vitro Results.” (to be submitted)
- Zhang, P., Zhang, N., **Gao, C.**, Zhang, L., Gao, Y., Deng, Y., Bluestein, D., “Scalability Test of Multiscale Fluid-Platelet Model for Three Top Supercomputers.” *Computer Physics Communications*, online April 2016.
- Zhang, P., **Gao, C.**, Zhang, N., Deng, Y., Bluestein, D., "Multiscale Particle-Based Modeling of Flowing Platelets in Blood Plasma Using Dissipative Particle Dynamics and Molecular Dynamics." *Cellular and Molecular Bioengineering*, December 2014, Volume 7, Issue 4, pp 552-574.
- Bluestein, D., Soares, J.S., Zhang, P., **Gao, C.**, Pothapragada, S., Zhang, N., Slepian, M.J., and Deng, Y. (2014) "Multiscale Modeling of Flow Induced Thrombogenicity with Dissipative Particle Dynamics (DPD) and Molecular Dynamics (MD)". *ASME J. Med. Devices*. 8(2): 0209541-209542.
- Soares, J.S., **Gao, C.**, Alemu, Y., Slepian M., Bluestein, D., “Simulation of Platelets Suspension Flowing through a Stenosis Model Using a Dissipative Particle Dynamics Approach.” *Annals of Biomedical Engineering*, November 2013, Volume 41, Issue 11, pp 2318-2333.

Conference Proceedings

- **Gao, C.**, Zhang, P., Bluestein, D., “Multiscale Modeling of Mechanotransduction Processes in Flow-Induced Platelet Activation”, *Proceedings of the 2nd IEEE International Conference on High Performance and Smart Computing (HPSC 2016)*, NY, April 9-10, 2016.

Abstracts

- Zhang, P., **Gao, C.**, Zhang, N., Slepian, M.J., Deng, Y., Bluestein, D. "A Predictive Multiscale Model for Simulating Flow-Induced Platelet Activation: Correlating with In-Vitro Results." *The 8th International Bio-Fluid Symposium*, CalTech Pasadena, California, February 12-14, 2016.
- Zhang, P., **Gao, C.**, Sheriff, J., Slepian, M.J., Deng, Y., Bluestein, D. "A Predictive Multiscale Model

for Simulating Flow-Induced Platelet Activation: Correlating with In-Vitro Results." Summer Biomechanics, Bioengineering and Biotransport Conference (SB3C), National Harbor, MD, June 29-July 2, 2016.

- Zhang, P., **Gao, C.**, Zhang, N., Slepian, M.J., Deng, Y., Bluestein, D. "A Predictive Multiscale Model for Simulating Platelets Activation in Shear Flows." BMES Annual Fall Meeting, Tampa, Florida, United States, 2015.
- Zhang, P., **Gao, C.**, Zhang, N., Slepian, M.J., Deng, Y., Bluestein, D. "A Predictive Multiscale Model for Simulating Platelets Activation in Shear Flows.", Presentation at the *2015 IMAG Multiscale Modeling (MSM) Consortium Meeting*, Lister Hill Auditorium, NIH Campus, United States, September 8-9, 2015.
- Zhang, P., **Gao, C.**, Zhang, N., Zhang, L., Pothapragada, S., Deng, Y., Bluestein, D., "Cloud Supercomputing: Multiscale Simulation Techniques and Optimization for Biomedical Research." . New York Scientific Data Summit (NYSDS), New York, NY, United States, 2015.
- Zhang, P., **Gao, C.**, Zhang, N., Pothapragada, S., Slepian, M.J., Deng, Y., Bluestein, D. "Multiscale Simulation of Shear-Induced Platelet Activation: Correlating Numerical with Experimental Results." SB3C 2015, Summer Biomechanics, Bioengineering and Biotransport Conference, Snowbird Resort, Utah, United States, 2015.
- Zhang, P., Sheriff, J., **Gao, C.**, Livelli, M., Pothapragada, S., Zhang, N., Zhang, L., Slepian, M.J., Deng, Y., Bluestein, D. "A Multiscale Particle Based Model of Platelets in Shear Flows: Correlating Numerical Simulations with In Vitro Results." BMES Annual Fall Meeting, San Antonio, Texas, United States, 2014.
- Bluestein, D., Zhang, P., **Gao, C.**, Sheriff, J., Pothapragada, S., Zhang, N., Livelli, M., Soares, J.S., Slepian, M.J., Deng, Y. "Multiscale modeling of flow induced thrombosis using dissipative particle dynamics (DPD) and coarse grained molecular dynamics (CGMD)." The 7th World Congress of Biomechanics. Boston, MA, United States, 2014.
- **Chao Gao**, Danny Bluestein. "Multiscale Modeling of Fine-Grained Platelet Suspension in CoarseGrained Blood Flow using Molecular Dynamics and Dissipative Particle Dynamics." SC13 Doctoral Research Showcase, Denver, CO, United States, 2013.
- **Gao, C.**, Zhang, P., Livelli, M., Sheriff, J., Soares, J., Pothapragada, S., Zhang, N., Deng, Y., Bluestein, D. "Multiscale Modeling of Fine-Grained Platelet Suspension in Coarse-Grained Shear Flow Using Molecular Dynamics and Dissipative Particle Dynamics." BMES Annual Fall Meeting, Seattle, WA, United States, 2013.

- Chiu, W-C., Alemu, Y., **Gao, C.**, Lynch, B., Einav, S., Slepian, M.J., Bluestein, D. "Comparative Studies of Ventricular Assist Devices and the Effect of Inflow and Outflow Cannulations." BMES Annual Fall Meeting, Seattle, WA, United States, 2013.
- Zhang, P., Sheriff, J., Soares, J.S., **Gao, C.**, Pothapragada, S., Zhang, N., Deng, Y., Bluestein, D. "Multiscale Modeling of Flow Induced Thrombogenicity Using Dissipative Particle Dynamics and Coarse Grained Molecular Dynamics." in *Proceedings of the ASME 2013 Summer Bioengineering Conference*, Sunriver, Oregon, June 26-29, 2013.
- Bluestein, D., Soares, J.S., Zhang, P., **Gao, C.**, Pothapragada, S., Zhang, N., Slepian, M.J., Deng, Y. "Multiscale Modeling of Flow Induced Thrombogenicity with Dissipative Particle Dynamics (DPD) and Molecular Dynamics (MD)." 2013 1st Annual ASME/FDA 2013 Frontiers in Medical Devices: Applications of Computer Modeling and Simulation, Washington, D.C., United States, 2013.
- Bluestein, D., Soares, J.S., Zhang, P., **Gao, C.**, Pothapragada, S., Zhang, N., Slepian, M.J., Deng, Y. "Multiscale Modeling of Flow Induced Thrombogenicity Using Dissipative Particle Dynamics and Molecular Dynamics," in *Proceedings of the ASME 2013 2nd Global Congress on NanoEngineering for Medicine and Biology*, Boston, Massachusetts, USA, February 4–6, 2013.
- Soares, J.S., **Gao, C.**, Sheriff, J., Alemu, Y., Zhang, P., Pothapragada, S., Yu, G., Deng, Y., Bluestein, D. "Multiscale Modeling of Shear Induced Platelet Activation Using Dissipative Particle Dynamics and Molecular Dynamics." BMES Annual Fall Meeting, Atlanta, GA, United States, 2012.

Acknowledgements

I would like to express my deepest gratitude to my Ph.D. advisor Dr. Danny Bluestein for his generous guidance and support during my doctoral research at Biofluids Research Group, Stony Brook University. He provided me the opportunity to explore the research topic of fluid-shear induced platelet activation based on multiscale modeling approach, from which I gained a comprehensive understanding of biofluids phenomena from macroscopic hemodynamics to cellular and molecular biomechanics. Dr. Bluestein's insight in biofluids research and his determination in tackling the most challenging biomedical problems encouraged me to overcome difficulties and elevate my research work to a higher level.

I would like to thank Professor Wei Yin for serving as chair of my doctoral dissertation committee, along with Professor Gabor Balazsi and Professor Robert Harrison for serving as my committee members. They shared their expertise and knowledge with me that enriched my research and dissertation. I also want to thank Professor Yuefan Deng for providing me sufficient supercomputer resources to conduct my research.

Great support to my research also come from the members of Biofluids Research Group. Particularly, I would like to thank Dr. Peng Zhang for his guidance to me in molecular dynamics and high performance computing. I want to thank Dr. Jawaad Sheriff for discussion with me the platelet biology and experiments, Dr. Gil Marom and Dr. Oren Rotman for providing expertise in computational fluid dynamics and experimental biofluids mechanics. I want to thank Dr. Joao Soares, Dr. Seetha Pothapragada, Dr. Na Zhang, and Li Zhang for collaboration with me in multiscale modeling. Joy and happiness are also brought by my fellow PhD students Philip Chiu, Matteo Bianchi, and Ram Ghosh.

I would like to acknowledge the funding support of:

- NIH NHLBI R21 HL096930-01A2 (DB)
- NIH NIBIB Quantum Award Phase I R01 EB008004-01 (DB)
- NIH Quantum Award Implementation Phase II-U01 EB012487-0 (DB)

and computational resources of:

- Sunway Bluelight System, Jinan Supercomputing Center, China

- Tianhe-2, Guangzhou Supercomputing Center, China
- Comet, San Diego Supercomputing Center, US
- Stampede, Texas Advanced Supercomputing Center, US

Warm thanks to the faculties and staff of Biomedical Engineering Department that helped me for everything during my graduate study.

Finally, I would like to extend my deepest gratitude to my parents Xiaohui Xie and Wenyi Gao, and my girlfriend Jianjin Xu for their constant love, support, and encouragement that accompanied me to go through this great journey.

I. Introduction

1.1 Fluid-shear induced platelet activation

Cardiovascular diseases (CVD) remain the leading cause of death in the US. An estimated 80 million adults suffer from one or more types of CVD, including high blood pressure (HBP), coronary heart disease (CHD), heart failure (HF), stroke, etc.⁴⁷. Among all types of CVD, heart failure is the final common pathway in which there is significant ventricular dysfunction due to progressive atherothrombotic events. The advent of implantable mechanical circulatory support such as ventricular assist device (VAD) and prosthetic cardiovascular device such as prosthetic heart valve (PHV) provide life-saving solutions for treating patients with severe heart failure and helping to extend their life expectancy. The total number of annual procedures involving implantations of these devices in the US is several millions per year.

One of the major culprits in such devices is emergence of pathological flow patterns that enhance hemostatic responses including platelet activation, aggregation, and adhesion. The thromboembolic complications that such devices promote remain an impediment to the device recipients. VAD recipients have approx. 16% stroke rate, of which 25% prove fatal. Mechanical heart valves (MHV) patients develop thromboembolic complications at a rate of 0.7% to 6.4% per patient year. In all these devices, platelets undergo repeated passages, and are prone to be activated when exposed to cumulative high shear stresses during these passages. As a consequence, thrombus or clot may form after implantation. To prevent this, patients must take life-long anticoagulant drugs, which, as a side effect, induce vulnerability to hemorrhage. To minimize the thrombogenic potential of these devices, it is critical to elucidate the underlying mechanisms of shear-induced platelet activation that then could be used for effective design optimization.

The cardiovascular system is an internal flow loop with blood vessels of various lengths, cross-section areas and curvatures, and multiple branches⁹⁹ (Table 1). By systemic and pulmonary circulations, the blood is carried to the capillaries of the tissues and returned to the heart via different levels of arteries and veins⁷. Aorta is the largest blood vessel with diameter of ~ 20 mm that traverses the abdomen and bifurcates into left and right common iliac arteries^{98,99}. Carotid artery (~ 6 mm) delivers blood to the brain, and coronary artery (~ 4 mm) mediates the blood supply to the heart⁷⁴. Microcirculation constitutes vascular network of arterioles (~ 10 to 100 μm) and capillaries (less than 10 μm).

Table 1. Blood flow properties through cardiovascular system and prosthetic devices

	Diameter (mm)	Velocity (mm/s)	Reynolds number	Wall shear stress (dyne/cm ²)	Wall shear rate (s ⁻¹)
Aorta ^{68,98}	20	400	2800	4.3	150
Common carotid artery ⁷²	6.5	300	700	15	1000
Arteriole ^{8,45,87,94}	0.015	1.1	0.006	25	700
Capillary ^{10,35,49}	0.005	2	0.7	20	1800
SJM regular ⁸⁰	0.15	3500	150	6515	

Blood is composed of blood cells suspended in blood plasma. The blood cells include red blood cells, white blood cells and platelets. The hematocrit describes the volume percentage of red blood cells in blood. It drops from 40 to 45% in arteries of normal adults to 10 to 20% in small capillaries⁹⁴. The platelet count in healthy individuals ranges from 150, 000 to 450, 000 per μL .

A wide range of fluid shear stress can occur depending on the characteristic length of blood vessels, the gender, age, and various degrees of stenosis. In aorta, the mean shear stress is measured as 4.3 dyne/cm²⁶⁸. In common carotid artery, the mean wall shear stress is from 12 to 15

dyne/cm² in males and from 11 to 13 *dyne/cm²* in females ⁷². In hinge region of mechanical heart valve, the peak shear stress can be 6000 *dyne/cm²* ⁸⁰. In ventricular assist devices, platelets are exposed to shear stresses up to 8000 *dyne/cm²* ⁸².

Platelets can be activated by chemical agonists, such as Von Willebrand factor, thrombin, and fibrinogen. These platelet stimuli bind to specific platelet surface receptors, which emit signals that transduce through the membrane into the platelet and modulate the levels of intracellular messengers, such as Ca²⁺, and diacylglycerol, that then trigger the physiological response by changes in phosphorylation, enzymatic activities, and structural properties of proteins ⁷⁹. Positive-feedback loops exist in platelet. For instance, endoperoxides (EPs)/thromboxane A2 (TxA2) and ADP are secreted from activated platelets and bind to specific receptors and enhance platelet activation. Resting platelets have a discoid shape with diameter of approximately 4 μm. When platelets are in fluid suspension, the initial response of stimulation is platelet shape change, which includes two separate and independent events, the spheration of platelet and the pseudopodia formation due to separable assembly of contractile and pseudopodal cytoskeletons ⁹⁶.

In contrast to biochemical pathways of platelet activation, cells also have mechanosensors that respond to mechanical stress by changing their conformation. These molecules are able to convey information of extracellular environment to the cell interior via conversion of physical stimuli to chemical signals ³⁰. The mechanical signals received by surface mechanosensors such as integrin would transfer to the cytoskeleton either by means of biochemical pathway, or via the connected structural components such as proteins linking integrin to cytoskeleton. Brown et al. ⁶ found that exposed to low shear stress of 50 *dyne/cm²*, platelets release small amounts of ATP, ADP and serotonin. Shear stresses of 100 *dyne/cm²* can lead to cell lysis. Shear stresses of 250 *dyne/cm²* or more can result in platelet fragmentation. Platelet activation has been shown to be

more accurately described by the cumulative stress along platelet transport trajectory, as a function of shear stress and exposure time. The exposure time to certain shear stress ranges from milliseconds to minutes^{4,32,82}. In vitro studies investigate the cumulative shear stress on platelet activation by applying physiological and pathological shear stress waveforms to platelets and measure thrombin generation and expression of platelet surface thrombogenic markers^{16,108,112}. Constant or dynamic shear stress waveforms are applied to platelets through perfusion chambers such as cone and plate shearing device to mimic the in vivo flow conditions.

1.2 Numerical modeling of blood flow based on multiscale approach

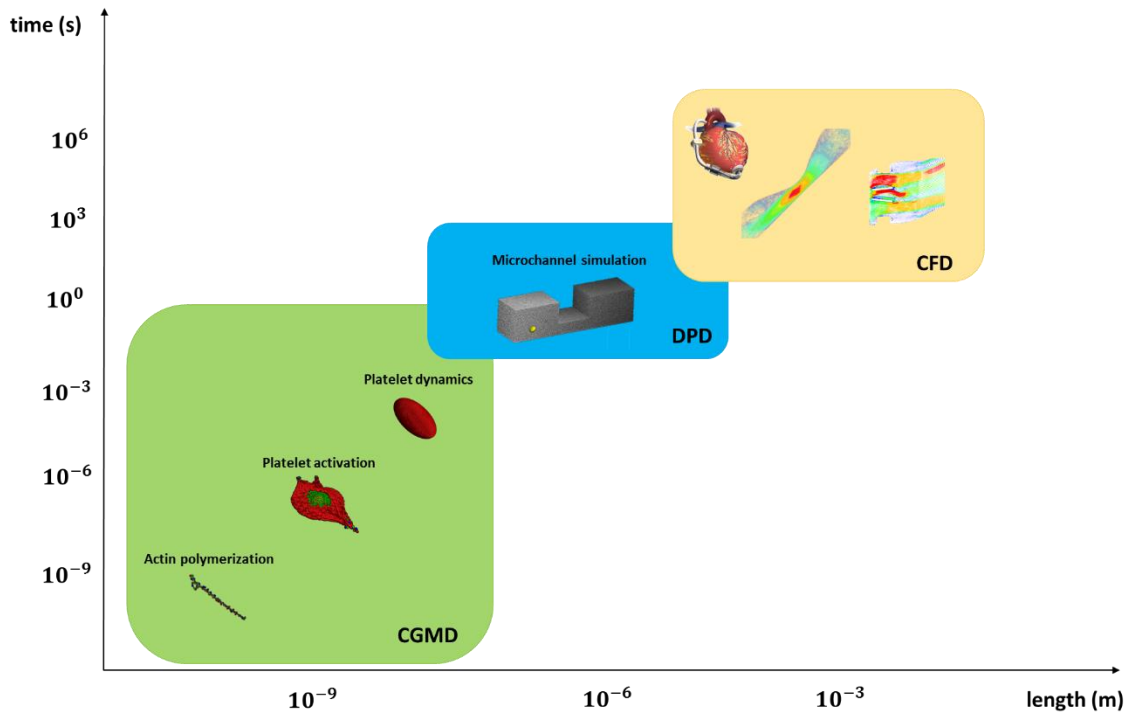


Figure I-1. Shear-induced platelet activation at multiple spatial-temporal scales. CFD covers mm in length and seconds in time. DPD covers 1 μm to 100 μm in length and μs to ms in time. CGMD covers nm to μm in length and ns to μs in time.

Traditionally, simulations of blood flow in the vasculature treat blood as a continuum and solve Navier-Stokes equations governing viscous blood flows. Shear stress distribution within the

prosthetic devices can be modeled using computational fluid dynamics (CFD), e.g., by modeling spherical particles representing platelets that are injected into the inflow of the device and computing the fluid shear stress accumulation along their corresponding trajectories in order to estimate their thrombogenic potential ¹⁰². Due to the limited scales range that can be simulated using continuum approaches (down to μm level at the most), CFD is not able to address the subsequent biomechanical interactions and biochemical reactions of blood's individual constituents, which occur at the nm scales, leaving a gap from 100 μm down to 10 nm between the macroscopic fluid dynamics and the biochemical scales. It is clear that an approach based purely on a continuum assumption such as CFD is unable to capture this multiscale nature of flow induced platelet activation and may fail to establish the direct correlation between mechanical stimuli and platelet activation on the cellular and molecular scales.

The blood is a heterogeneous material composed of a variety of substances including blood plasma, white blood cells, red blood cells, platelets, and proteins. The physical characteristics of blood flow are significantly affected by the material properties of individual cellular components ¹⁰³. The progress of thrombosis is initiated by platelet activation, which can be induced by pathological flow patterns emerged in cardiovascular diseases and prosthetic devices. Multiple activated platelets then interact and aggregate via GPIIb-IIIa-fibrinogen/vWF bridging, followed by the phase change of the coagulated material ^{55,95}. These processes involve complex phenomena on multiple length scales: the hemodynamics including fluid shear stress, vortices, and recirculation zones are described on 10 μm to 100 μm scale; platelet transport dynamics and platelet-platelet interactions are addressed on the 1 to 10 μm scale; the pseudopodia formation, and receptor-ligand binding are on the nm scale ^{19,95}. A successful computational approach should take into account

the multiscale nature of the shear-induced thrombosis and be able to couple the blood flow phenomena across disparate length and time scales.

Discrete particle approaches such as dissipative particle dynamics (DPD) and molecular dynamics (MD) are well suited to model multiphase and multicomponent blood flow, where both fluid phase such as blood plasma and solid phase such as platelets are represented as ensembles of particles and their interactions can be easily addressed with various physical potential functions and force fields. DPD is a coarse-grained particle-based approach that represents blood flow by directly modeling blood plasma and individual cellular and molecular components as ensembles of discrete particles. It can bridge the gap ranging from 10 *nm* to 100 μm between the continuum-based blood flow representation and the microscopic molecular events of platelet activation and thrombus formation^{10,103}. It has been successfully employed to simulate the complex rheological properties of blood flow, including blood-plasma separation^{44,48}, Fahraeus-Lindqvist Effect, cell free layer, margination of white blood cells and platelets¹³, platelets transport and interactions through stenosis⁸¹, and platelet-mediated thrombosis¹⁹.

MD simulations are important tools to investigate the nanoscale dynamics of biological macromolecules such as proteins, nucleic acids and lipid bilayer membranes, by providing the ultimate detail concerning individual particle motions as a function of time³³. These simulations use atoms as the minimum unit and allow observation of molecular behaviors with femtosecond (10^{-15} s) time resolution and angstrom (10^{-10} m) spatial resolution^{33,104}. An atomistic MD model can accurately capture the system dynamics. However, due to the computational limitation, it only allows the system to be studied with small system size and short observation time. In addition, we aim to understand the mesoscopic behaviors of platelets and the platelet-mediated thrombosis, in

which the atomistic details of the model can be neglected. Therefore, a mesoscopic coarse grained model would be more suitable than a model with full atomistic detail.

Coarse-grained MD (CGMD) enables us to focus on the particular scales of interactions by averaging the less essential degrees of freedom, resulting in a reduction of computational cost while still capturing the essential phenomena⁷¹. CGMD has been successfully employed to simulate polymers, proteins, bilayer membrane, cytoskeleton, and blood cells^{43,109,117}.

Taking advantages of fast and larger scales simulations of hydrodynamic phenomena with DPD and finer resolved molecular description with CGMD, an integrated multiscale DPD-CGMD approach is designed which couples dynamic biophysical transport phenomena of flow induced stresses acting on the platelet membrane and cytoskeleton with structural and functional changes in the platelets leading to their activation at disparate length and time scales. This innovative computational approach can provide insights into the causal relationship between the pathological shear stresses generated within such devices and the flow induced thrombus formation.

1.3 Dissertation outline

The current work is structured as follows:

In Chapter II, the top-scale DPD-based platelet suspension model is developed, in which both blood plasma and platelet are modeled with particles interacting with each other by DPD force fields. The no-slip boundary condition is developed to enable blood plasma flow through 3D geometries with various shapes. The platelet suspensions flowing through the 3D stenotic microchannel is simulated. The inflow-outflow boundary condition is developed to enable the fluid flow driven by pressure gradient. The performance of DPD blood plasma simulation is conducted and strong scaling efficiency is measured for five different geometry cases: 50 %, 75 %, 150%, C-shape and S-shape.

In Chapter III, the compressible effect of DPD blood plasma flowing through severe stenotic microchannel is improved by introducing Morse potential into DPD force fields. The DPD-Morse fluid compares favorably with CFD results in describing fluid flow properties including fluid mass density, velocity and shear stress. The influence of compressible effect on platelet shear stress accumulation is investigated by comparing rigid platelet transport in both DPD-Morse and DPD fluids.

In Chapter IV, the mesoscopic DPD blood plasma is interfaced with a CGMD platelet to achieve multiscale blood plasma-platelet interaction. The platelet membrane stress is depicted and used as a new metric to predict platelet activation, other than the local fluid stress. The surface stress accumulation of a rigid and deformable platelets are compared which shows that the rigid platelet model overestimates the platelet activation potential by over predicting its surface stress.

In Chapter V, the shear-induced platelet activation is investigated by modeling mechanotransduction process and ensuing pseudopodia formation, using multiscale DPD-CGMD model. The simulation results are compared with experiments in terms of platelet pseudopodia lengths and number.

II. Modeling platelet suspensions flowing through stenotic microchannel

2.1 Introduction

Previous efforts of our group focused on the modeling of fully developed viscous fluid flow through 3D stenotic microchannel based on CGMD approach, where blood plasma was modeled as free particles and vessel wall as frozen particles^{18,103}. The particle interaction for fluid-fluid and fluid-wall were characterized by Lennard-Jones potential with different parameter sets. The CGMD simulation results were compared with CFD and excellent agreement was achieved in describing parabolic velocity profiles and regions of fluid recirculation distal to the constriction. The same method was also applied to 3D mechanical heart valve (MHV) geometry to depict the platelet dispersion patterns during regurgitation around the tip of the leaflets¹⁰³.

In the current work, a platelet suspension model through 3D stenotic microchannel was developed. Instead of using Lennard-Jones potential as the interacting force fields, the current model employed DPD formulation that permits the description of viscous blood plasma behavior and allows the explicit modeling of platelet⁸¹. The blood plasma was modeled as free DPD particles. The platelet was constructed as an ellipsoid capsule with one layer membrane represented by connected DPD particles on a network of springs. First, the fluid properties such as density, viscosity, velocity and shear stress were analyzed with counter-Poiseuille flow to validate the operation range of the DPD formulation in approximating incompressible fluid flow. To enable the simulation of DPD fluid through a variety of 3D complex geometries mimicking blood vessels, a novel algorithm was developed to impose no-slip boundary condition on DPD fluid particles without explicitly modeling vessel walls with frozen particles, which is known to yield unstable results such as density fluctuations^{5,63}. The no-slip BC algorithm is an extension of Willemsen et al.⁹⁷ and can obtain no-slip at fluid-solid boundaries of any 3D complex wall geometries

constructed with triangular meshes. This is achieved by applying the algorithm in a local sense to each of these triangular elements with a controlling effect only on fluid particles coming into the triangular area.

The platelet model preserves elasticity and bending stiffness supplied by harmonic bonds and dihedral angle potentials. It allows studies of single cell behavior including migration, deformation, and dynamics in the viscous blood plasma, and platelet-platelet, platelet-wall interactions in simulations of platelet suspensions. The current model is considered as a top model of a fully coupled multiscale approach to investigate fluid-shear induced platelet activation and thrombosis: (i) a bulk fluid flow model of platelet suspensions that provides mechanistic inputs of fluid flow to individual platelets; (ii) a molecular scale platelet model based on CGMD that enables the simulation of complex processes of platelet shape change and pseudopodia formation; (iii) two-way couplings of both scales, i.e., fluid-shear will induce pseudopodia formation, and the shape change of platelet will in return alter the local fluid dynamics.

2.2 Methods

2.2.1 Modeling viscous fluids with DPD

The blood plasma was modeled with DPD methodology, in which the motion of each DPD particle is governed by

$$d\mathbf{v}_i = \frac{1}{m_i} \sum_{j \neq i}^N (\mathbf{F}_i^C dt + \mathbf{F}_i^D dt + \mathbf{F}_i^R \sqrt{dt}) \quad (\text{II-1})$$

where \mathbf{F}_i^C , \mathbf{F}_i^D , \mathbf{F}_i^R are the conservative, dissipative and random forces acting on the particle i . The pairwise interacting forces between particle i and j are given by

$$\begin{aligned}
\mathbf{F}_i^C &= \begin{cases} a \left(1.0 - \frac{r_{ij}}{r_c}\right) \mathbf{e}_{ij}, & r_{ij} < r_c \\ 0 & r_{ij} \geq r_c \end{cases} \\
\mathbf{F}_{ij}^D &= -\gamma w^D(r_{ij})(\mathbf{v}_{ij} \cdot \mathbf{e}_{ij})\mathbf{e}_{ij} \\
\mathbf{F}_{ij}^R &= \sigma w^R(r_{ij})\xi_{ij}\mathbf{e}_{ij}
\end{aligned} \tag{II-2}$$

where $\mathbf{r}_{ij} = \mathbf{r}_i - \mathbf{r}_j$, $r_{ij} = |\mathbf{r}_{ij}|$, $\mathbf{e}_{ij} = \mathbf{r}_{ij}/r_{ij}$, $\mathbf{v}_{ij} = \mathbf{v}_i - \mathbf{v}_j$, r_c is the cutoff radius. a , γ , σ are the strength of conservative, dissipative and random forces, respectively. ξ_{ij} is a random number with zero mean and unit variance. Dissipative force \mathbf{F}_i^D is to reduce relative motion of a particle pair and describes the viscous resistance of fluid. Random force \mathbf{F}_i^R is to introduce thermal fluctuations of DPD fluid. The dissipative and random forces form a thermostat that satisfies the fluctuation-dissipation theorem such that the DPD system is able to maintain equilibrium temperature T . This relationship is given by $\sigma^2 = 2\gamma k_B T$, where k_B is the Boltzmann constant. The weight functions $w^D(r)$ and $w^R(r)$ are given by

$$w^D(r_{ij}) = [w^R(r_{ij})]^2 = \left(1.0 - \frac{r_{ij}}{r_c}\right)^{2k} \tag{II-3}$$

where parameter k affects the viscosity of the DPD fluid.

The DPD parameters are determined as $k = 0.25$, $a = 25.0$, $\sigma = 3.0$, $\gamma = 4.5$, and number density $n = 3.0$. The time evolution of particle position and velocity is determined by Newton's second law that is integrated by the modified Velocity-Verlet algorithm.

2.2.2 Study of fluid flow properties using counter-Poiseuille flow

The dynamic viscosity μ is measured by counter-Poiseuille flow method, in which the flow system is divided into two symmetric regions, and a pair of body forces is applied to the DPD particle of each region in opposite directions^{5,81}. μ is determined by fitting the parabolic velocity profiles developed in periodic Poiseuille flow to the analytical solution of the Navier-Stokes

equation (Figure II-8). A system of size $30 \times 30 \times 30$ with $n = 3.0$ is divided into two regions where body force $g = 2.0$ is applied in opposite directions. Periodic boundary conditions are employed in three directions of the simulation box. The integration timestep is $dt = 0.005$. Fully developed velocity profile is achieved after simulation of 10, 000 time steps. For postprocessing, the 3D simulation box is divided into 60 vertical bins along x direction with side length of 0.5, where the velocity profile is obtained by averaging particle velocity in each layer for 5, 000 time steps.

The analytical solution for fluid region on the left side was determined by solving Navier-Stokes equation:

$$\rho \left(\frac{\partial v}{\partial t} + \frac{u\partial v}{\partial x} + \frac{v\partial v}{\partial y} + \frac{w\partial v}{\partial z} \right) = -\frac{\partial p}{\partial y} + \mu \left(\frac{\partial^2 v}{\partial x^2} + \frac{\partial^2 v}{\partial y^2} + \frac{\partial^2 v}{\partial z^2} \right) + \rho g_y \quad (\text{II-4})$$

where velocity $u = 0$, $v \neq 0$, $w = 0$, pressure gradient $\frac{\partial p}{\partial y} = 0$, body force $g_y \neq 0$. The boundary condition is $v(x = 0) = 0$, $v(x = L) = 0$, where L is the characteristic length.

Solution of equation (II-4) presents

$$v = -\frac{\rho g_y}{2\mu}(x^2 - Lx) \quad (\text{II-5})$$

Analytical solution corresponding to the right side can be acquired by reversing (II-5) with respect to x axis and then shifting to the right by L.

The fluid flow modeled with DPD bears compressibility effect and cannot sustain large compression because of soft interaction potential employed. The compressibility effects depend on the repulsive interactions^{15,59}. To determine the velocity range of DPD fluid in approximating incompressible fluid flow, body forces ranging from $g = 0.001$ up to $g = 0.2$ are imposed on fluid particles to achieve different maximum velocity under counter-Poiseuille flow. The velocity, number density and shear stress are analyzed after fluid flow is fully developed (Figure II-9).

2.2.3 Development of no-slip boundary condition in 3D complex geometries

The major issue of simulating DPD fluid flow in a three-dimensional confined geometry is to impose the no-slip boundary condition on the walls enclosing the DPD fluid. To simulate the viscous fluid phenomena of blood flow, such boundary condition needs to act to prevent the slip of the DPD particles on the boundary and minimize density fluctuations near the boundary. Particles within one cutoff distance to the boundary are subject to extra forces from fictitious particles that are generated by reflecting real fluid particles to the other side of the wall plane which possess inverted velocities of their real counterparts. Adding extra DPD interaction forces leads to an equilibrated shear layers across the wall and the velocity is zero on the wall. Besides, near wall particles are subject to a normal repulsive force that mimics the effect of the fluid fictitiously occupying the empty space beyond the wall. The repulsive force term controls the number density fluctuations near the wall ^{15,62,97}.

Along with the no-slip boundary condition, a novel reflection method is designed to confine all of the fluid particles within the concave wall geometry. As illustrated in Figure II-1, a single specular reflection is originally employed on an individual triangle for reversing the normal velocity of a fluid particle while keeping its tangential velocity unchanged and it is imposed only once on every triangle in order at every time step. However, it does not work for complex three-dimensional situations. For example in a concave shaped geometry, the single reflection fails when a fluid particle hits the same triangle more than once at the same time step. Therefore, in addition to the single reflection, double and triple reflections are designed. Figure II-1 (c) shows the double reflection: once a fluid particle is within an edge region formed by two neighbored triangles: triangles A and B, it has to be reflected twice to be bounced back to the fluid domain. Similarly,

Figure II-1 (d) shows the triple reflection: once a particle is within a corner region formed by three neighbored triangles: triangles A, B and C, it has to be reflected three times.

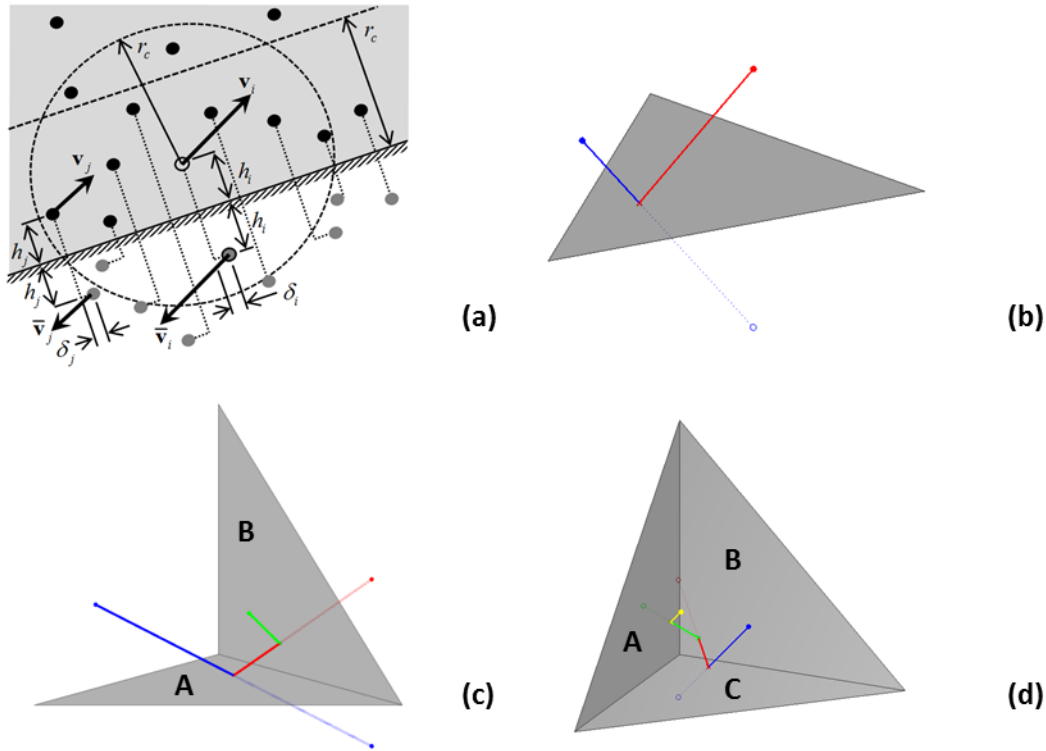


Figure II-1. Schematic of implementation of no-slip boundary condition. (a) Particles within one cutoff distance to the wall are subject to extra DPD forces arising from the interactions between real and fictitious particles. The repulsive force is included to mimic the existence of fluid particles outside of computational domain. The addition of dissipative and random forces aims to create an equilibrated shear layer across the wall such that no-slip boundary condition is achieved at the wall. (b to d) Particles moving across the wall are reflected back with specular reflection.

A complex geometry is considered with a connected mesh of triangular elements, each representing a planar solid wall onto which no-slip condition is applied, along with a multiple reflection scheme to confine all of the fluid particles within the enclosed wall geometry. Complex geometries such as curved shapes found in stenosis and aneurysm are constructed using ANSYS DesignModeler and Meshing (Release 15.0). A finer mesh is imposed on regions with higher curvatures and coarse mesh on straight cylindrical region (Figure II-2).

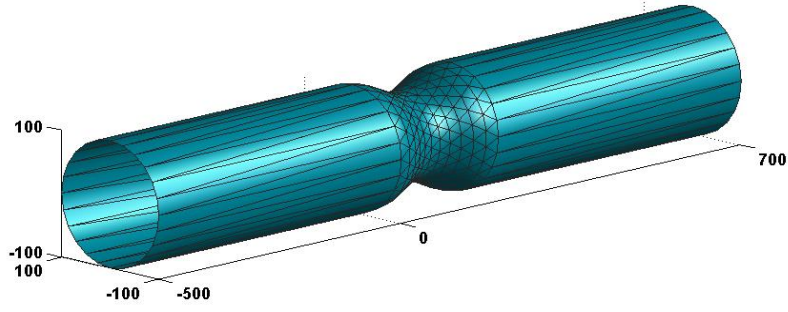


Figure II-2. Stenotic microchannel constructed with triangular wall elements. A fine mesh is imposed on stenotic region with large curvature, and coarse mesh on straight cylindrical region.

2.2.4 Modeling platelet suspensions through 3D stenotic microchannel

The platelet is modeled as deformable ellipsoid with 444 particles with dimension $4 \times 4 \times 2$ in μm . The pairwise interaction between platelet particles is DPD. Besides, harmonic bonds are defined in between platelet particles to represent an elastic membrane, and dihedral potentials are defined between adjacent triangles to provide in-plane bending stiffness of platelet (Figure II-3).

Harmonic bond potential is defined as:

$$V^B = k^b(r - r_0)^2 \quad (\text{II-6})$$

where k^b is the harmonic bond strength, r is the instant bond length, and r_0 is the equilibrium length.

Dihedral potential is defined as:

$$V^D = k^d(1 + \cos\phi) \quad (\text{II-7})$$

where k^d is the dihedral potential strength, ϕ is the angle between two adjacent triangles.

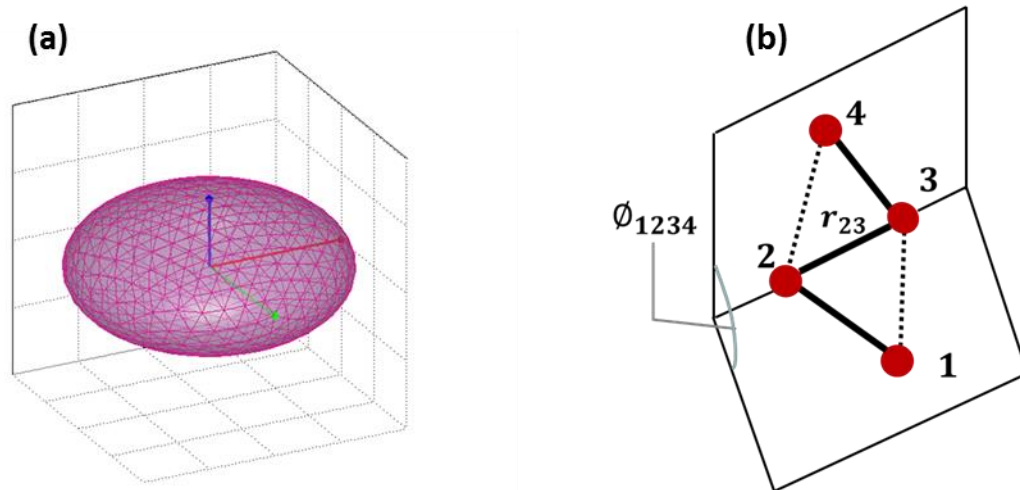


Figure II-3. Coarse grained platelet model with 444 particles, with pairwise DPD interaction and bond potential between the connected particles, as well as dihedral potentials between neighboring triangular elements. (a) Platelet model in ellipsoidal shape; (b) Schematic of bond and dihedral potentials with bond length r_{23} and dihedral angle ϕ_{1234} .

A platelet suspension model through 3D stenotic microchannel is developed. No-slip boundary condition is applied on the triangular walls, and periodic boundary condition along flow direction. A body force is applied on each fluid particle to drive the fluid flow. 117 platelets are randomly located and oriented in the fluid domain at the beginning of simulation.

2.2.5 Development of inflow-outflow boundary condition

An inflow/outflow boundary condition is developed to simulate non-periodic boundary flow. Several conditions need to be considered: (1) particles are inserted into the fluid domain at inlet with desired flow rate; (2) particles are removed from the fluid domain at outlet; (3) extra boundary forces are applied to maintain the mass conservation of DPD fluid within fluid domain. Considering all three conditions, imaginary periodic flow domains are incorporated at both upstream and downstream of interested fluid domain (Figure II-4). Imaginary fluid domains employ periodic boundary condition in flow direction. Particles leaving the imaginary domain

from one side are reinserted back to the same domain from the other side and number density in imaginary domain keeps constant. An extra boundary force scheme is applied to ensure the correct interaction of particles near periodic boundary (Figure II-5). Positions \mathbf{r} and velocities \mathbf{v} of near-boundary particles in region A and B are copied and sent to region A' and B' on the opposite side of imaginary domain and are considered as ghost particles. At upstream domain, an external body force is applied to fictitious particles to drive the flow and leads to a fully developed three dimensional parabolic velocity profile. To implement the particle insertion scheme at inlet of fluid domain, whenever an upstream fluid particle i comes into the fluid domain, before it is reinserted back to the upstream domain through periodic boundary, a new fluid particle is generated in the fluid domain with r_i and v_i (Figure II-4). A similar scheme is also applied at outlet. The mass flow rate and parabolic velocity profile of upstream domain is imposed to the fluid domain. At both inlet and outlet, fluid particles are removed from the simulation domain if they pass across the boundary. In addition to particle insertion/removal schemes at inlet/outlets, fluid particles in fluid domain within one cutoff distance to inlet/outlets also experience extra boundary forces from upstream/downstream fluid particles following DPD formulation. The purpose of the extra boundary force is to eliminate the force imbalance experienced by particles near inlet/outlets.

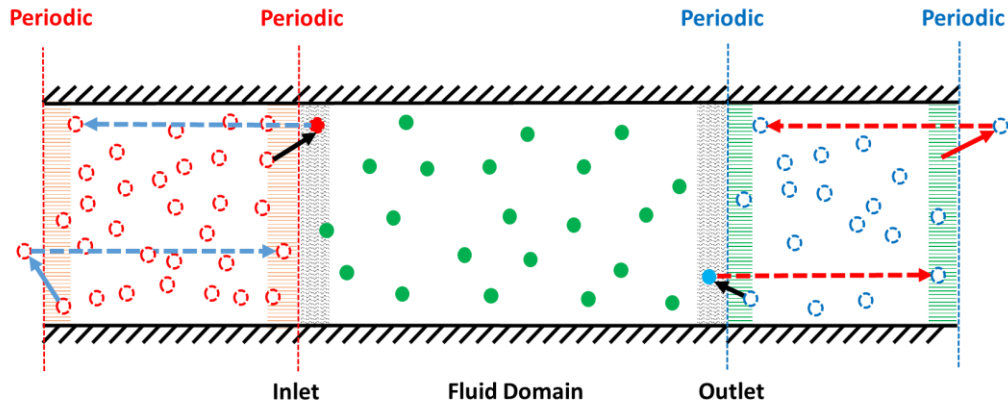


Figure II-4. 2D schematic of three-dimensional inflow/outflow BC model. The upstream, middle, and downstream fluid particles are illustrated in RGB color. Periodic boundary condition is applied to both upstream and downstream domains. Inflow/outflow boundary condition is applied to the middle fluid domain.

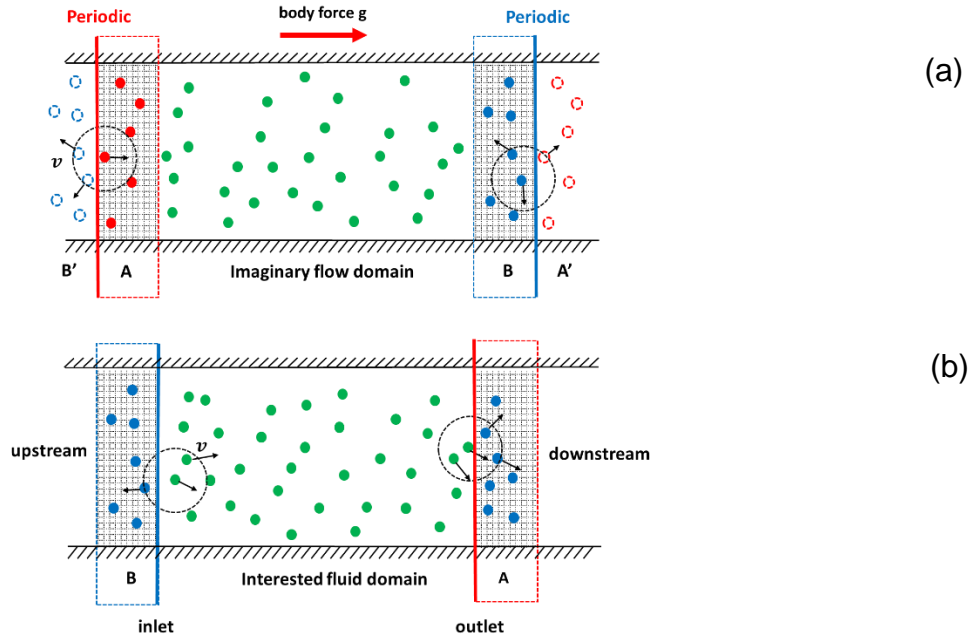


Figure II-5. Schematic of boundary force enforcement in imaginary flow domain and middle fluid domain. (a) Imaginary flow domain: region A and B include particles within one cutoff distance from the periodic boundary. Ghost particles are copied from A to A' and from B to B' to interact with real fluid particles on the opposite side. (b) Middle fluid domain: particles within one cutoff distance to the inlet/outlet interact with upstream/downstream fluid particles.

2.2.6 Parallel performance measurement on supercomputers

Five stenotic geometries are constructed with triangular elements wall by Gambit (Fluent Inc., New York; Figure II-7). Fine grained triangles are used at region with large curvatures and coarse grained triangles are used elsewhere to save computing time. No-slip boundary condition is applied on each triangular element, periodic boundary condition is applied at inlet and outlet. Body force $g = 0.02$ is added to each fluid particle to drive the flow. LAMMPS is employed for conducting the simulations. It is an established molecular dynamics code developed by Sandia National Laboratory⁶⁴. The simulations are conducted on the Sunway Bluelight System, which is petascale supercomputer with 137, 200 cores in total, including 8704 ShenWei SW 1600 processors with peak performance of 1.07016 PFLOPS and LINPACK efficiency as 74.37%⁸⁹.

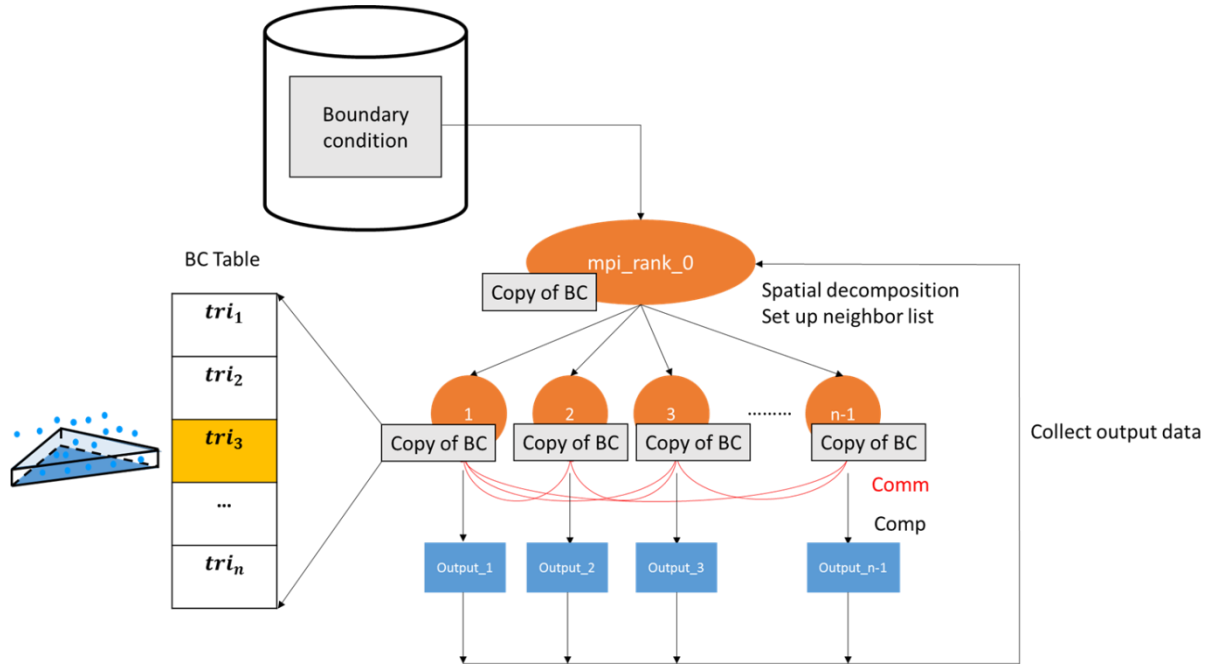


Figure II-6. Implementation of no-slip boundary condition. The boundary condition profile is loaded to the root processor with rank 0, and is broadcasted to the rest of processors. Each processor loops its local particles and determines if it resides inside any specific triangles.

The no-slip boundary condition is expressed as fix style written in an input file for simulation. Each triangular elements correspond to one fix command. Once simulation starts, this input file is loaded on processor 0, and are broadcasted to the rest of processors. Each processor traverses through this list of fix commands and determines if its local particles are within the region of influence by these fixes. If they are, then extra forces are applied to these local fluid particles to enforce no-slip boundary condition (Figure II-6).

To validate the accuracy of DPD method to simulate viscous fluid dynamics, The velocity profiles are visualized. The total simulation time is 100,000 timesteps in which $dt = 0.005$. The fluid region is divided into boxes with size $2 \times 2 \times 2$. The velocity of fluid particles within each box is averaged over 2000 timesteps and the result is printed out every 10,000 timesteps. The output file is post-processed by Matlab and the velocity profiles are generated (Figure II-16).

The strong scalability E and speedup S are defined as

$$E = \frac{T_1}{N * T_N} \quad (\text{II-8})$$

$$S = \frac{T_1}{T_N} \quad (\text{II-9})$$

where T_1 is computing time using single processor, N is total number of processors, and T_N is computing time using N processors. Here, the minimum number of processors is 500, and a linear scaling is imposed to derive the computing time T_1 .

Table 2. Number of particles and triangular elements.

	50% stenosis	75% stenosis	150% stenosis	C-shape	S-shape
1m case	1,000,922	1,021,287	1,077,113	1,040,164	1,040,939
10m case	11,117,701	11,347,866	11,986,190	11,572,056	11,566,388
Number of triangles	770	850	884	1294	1254

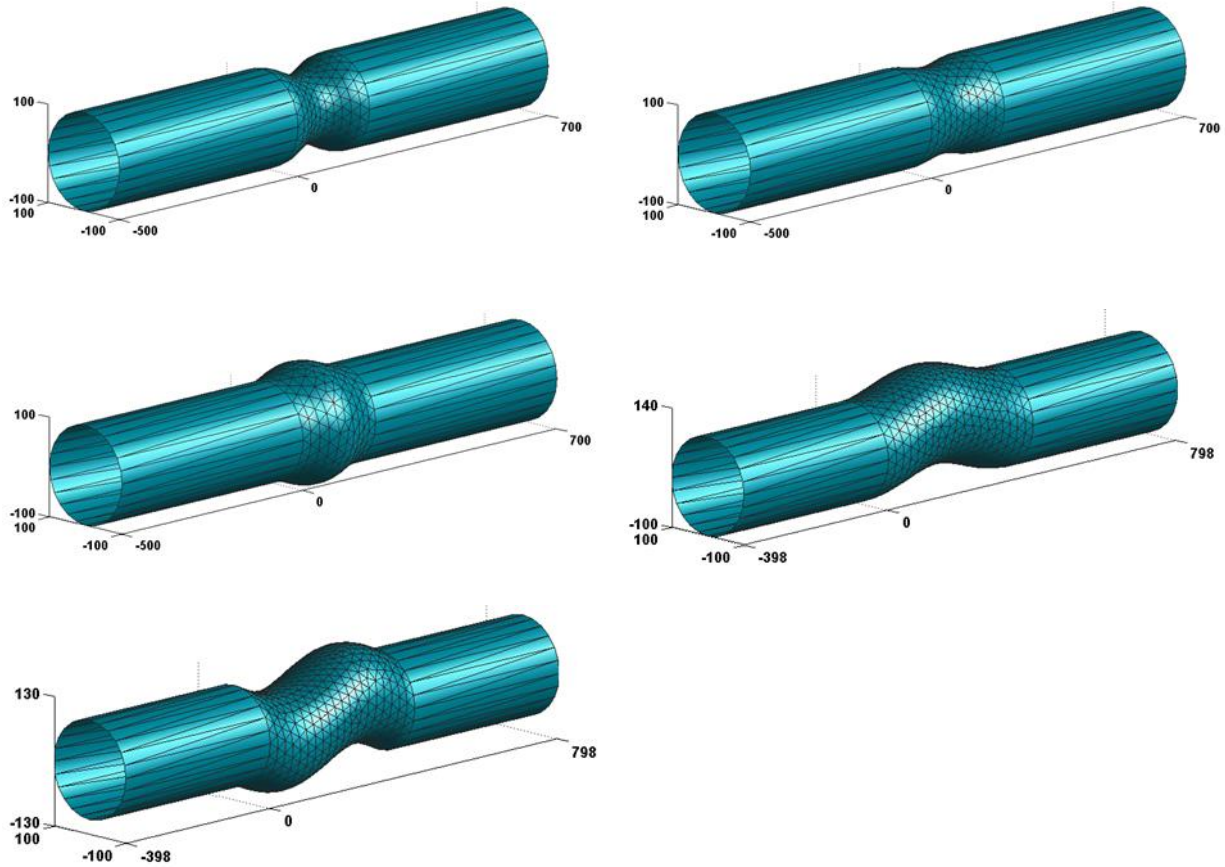


Figure II-7. Wall geometries for five simulation cases, 50%, 75%, 150%, C, and S shapes.

2.3 Results

2.3.1 Viscous fluid flow properties under counter-Poiseuille flow

Figure II-8 shows fully developed velocity profile from simulation (red dots) that is in good agreement with analytical solution (blue line). No-slip boundary condition is naturally preserved in such flow condition. When the parameter set $k = 0.25$, $a = 25.0$, $\sigma = 3.0$, $\gamma = 4.5$ is applied, the dynamic viscosity μ is determined as 1.5.

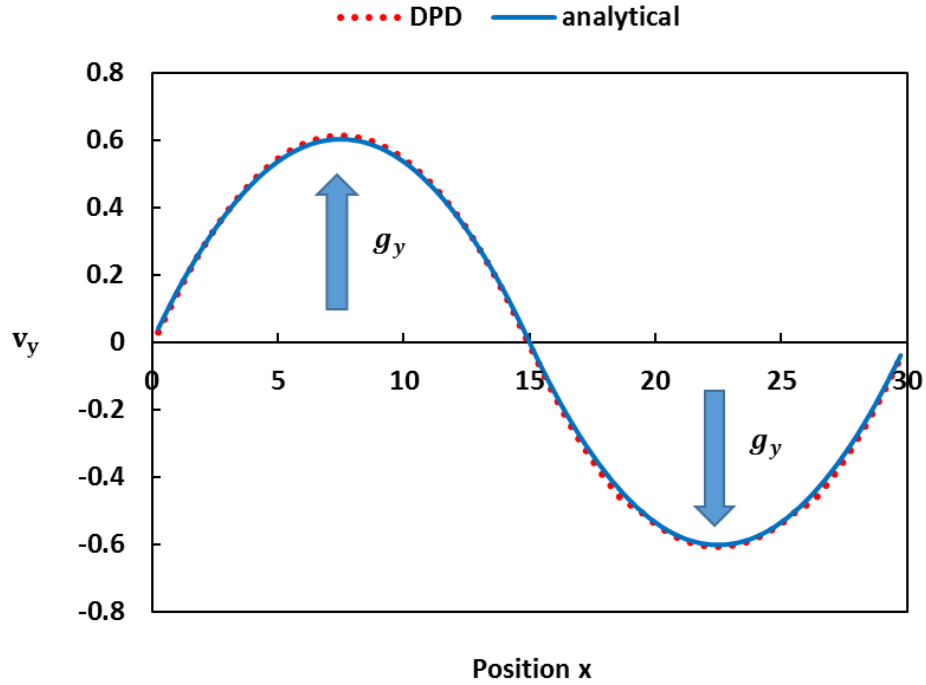


Figure II-8. Determination of μ through numerical fitting method.

Figure II-9 shows the fluid velocity, shear stress, and number density under different body forces ranging from 0.002 to 0.1, with Reynolds number from 17 to 750. Although fluid velocity is in good agreement with analytical solution, the shear stress starts to deviate from analytical solution as Reynolds number is increased, and mild number density gradient starts to appear. Furthermore, the speed of sound is determined in Soares et al. ⁸¹ by formula $c^2 = \partial p / \partial \rho$ at constant temperature. It is observed that the DPD fluid breaks down in approximating incompressible fluid whenever $v_y^{max} \gg c$.

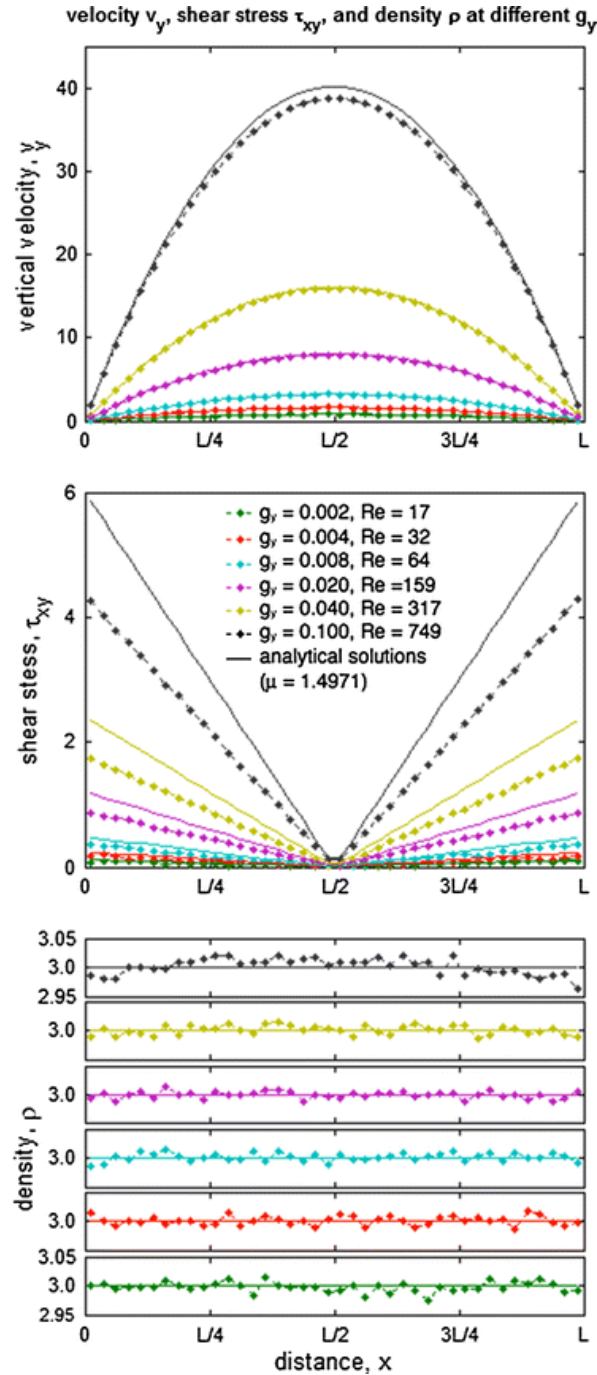


Figure II-9. Velocity, shear stress and density profiles developed with periodic Poiseuille flow under different body forces (dots – numerical simulations, lines – exact solutions). The DPD fluids breaks down in approximating incompressible fluid flow as the Reynolds number reaches 750 - though the velocity profile still matches the analytical solution, shear stress is badly estimated and mild density gradient develops.

2.3.2 Fluid development with no-slip boundary condition

Plane Poiseuille and Couette flow were first simulated to test the feasibility of no-slip boundary condition. Figure II-10 demonstrates the flow development process, in which the parabolic velocity profile was gradually achieved in Poiseuille flow, and a linear velocity profile in Couette flow.

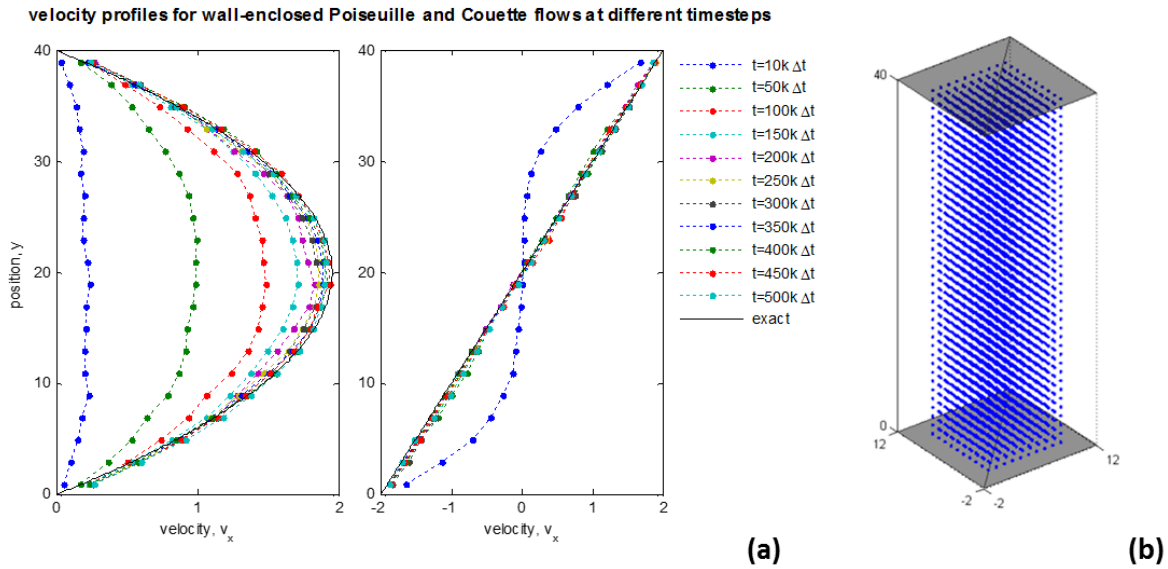


Figure II-10. Poiseuille and Couette flow development in channels enclosed by solid walls. (a) Velocity development of two types of fluid flows. (b) Schematic of simulation setup with upper and lower walls.

In three dimensional stenotic microchannel, DPD fluid flow achieves fully developed parabolic velocity profile, zero-velocity on the wall, and fluid acceleration through the stenotic region (Figure II-11). The boxes below present the flow development along $z = 0$ plane at upstream, stenotic, and downstream regions.

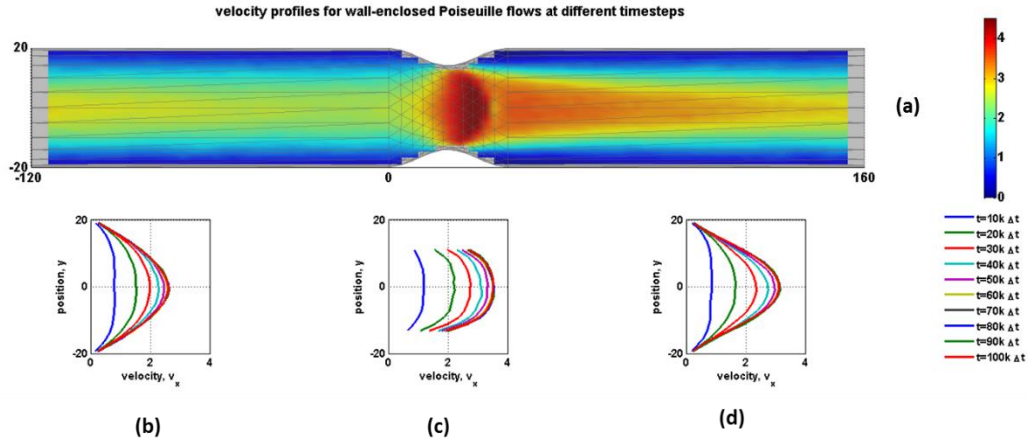


Figure II-11. Flow development in stenotic microchannel. Fully developed flow is achieved at 100, 000 time steps. (a) Cross-section view ($z = 0$) of velocity profile. Averaged velocity profile at upstream (b), stenotic (c), and downstream (d) region in $z = 0$ plane.

2.3.3 Platelet suspensions in stenotic microchannel

The platelet suspension transports with blood plasma through the microchannel (Figure II-12) with diameter $d = 20$, and 64% stenosis. The Reynolds number is 20, and the wall shear rate is 0.05. The individual platelets exhibit flipping motion⁵³, and collide with other platelets and with the wall. Platelets are initially randomly located in the fluid domain. As time proceeds, the platelets distribution becomes non-uniform and clusters of platelets are observed, as well as plasma-rich region with no platelets. This phenomenon is very similar to prior studies on red blood cells⁹¹. In the straight tube, platelets tend to stay in the core region and leave a cell-free layer (CFL) near wall. On the other hands, platelets that already reside in the CFL are observed to be trapped there, and have more contacts with the wall. More platelet-wall interaction takes place in the stenotic region, where platelets are squeezed together by the confined wall geometry, and accelerate through the stenotic throat. The average platelet velocity in the straight portion of the microchannel is 0.5, and the maximum velocity in the stenotic throat is 1.2.

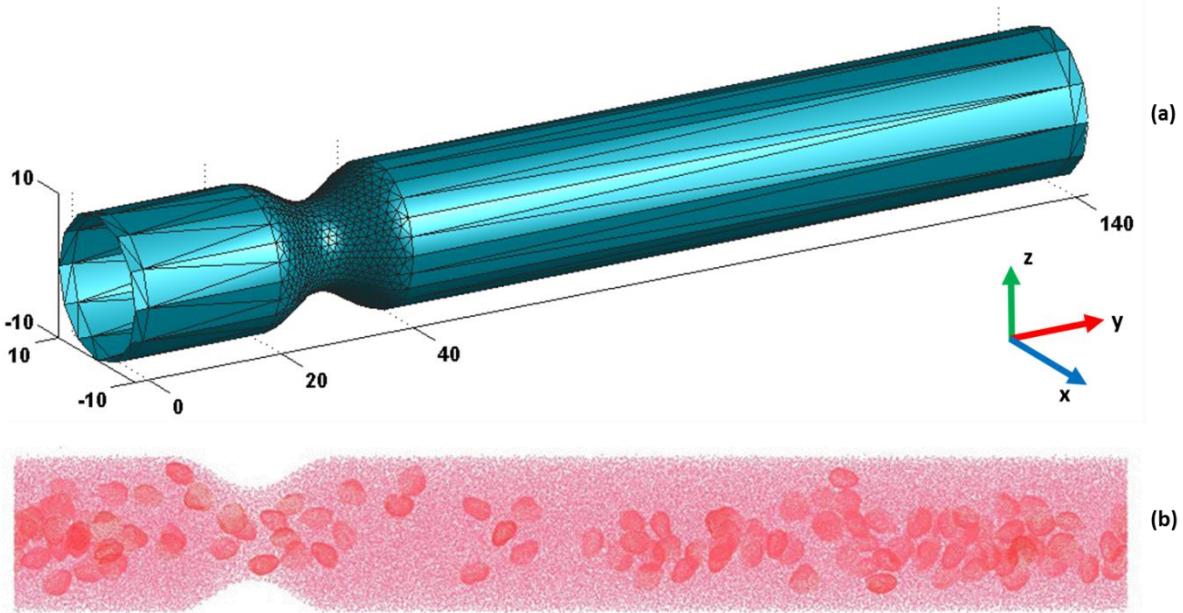


Figure II-12. Platelet suspension through stenotic microchannel. No-slip boundary condition is imposed on the walls, and periodic boundary condition on inlet and outlet. (a) Construction of stenotic microchannel; (b) Snapshot of platelet suspension in stenotic microchannel.

2.3.4 Validation of DPD viscous fluid flow dynamics under inflow/outflow BC

DPD fluid simulations are conducted in three dimensional cylindrical microchannel and the viscous fluid behaviors are compared between periodic boundary condition (PBC) and inflow/outflow boundary condition (I/O BC). A cylindrical microchannel is constructed and enclosed by fictitious walls with diameter 20 and length 35, and virtually divided it into three sub-domains: an upstream socket with length 5, a region of interest (ROI) domain with length 25, and downstream socket with length 5. A body force $g=0.5$ is used to drive the upstream fluid, leading to a maximum fluid velocity of 0.18. By applying the I/O BC at inlet, the mass and momentum of upstream fluid particles are transmitted to the ROI domain. At outlet, the fluid particles flowing out of the ROI region are removed. Additional DPD force was applied on particles in ROI region near boundaries by particles within upstream and downstream sockets. To validate the I/O BC

system, a control simulation with PBC is conducted where the fluid was driven by body force. No-slip BC was applied in both flow systems. The velocity and number density profiles in plane $z = 0$ are shown in Figure II-13. Fully developed velocity profile is achieved in I/O BC identical to the result of PBC. Higher number density was observed in I/O BC as a result of compressible effect of DPD fluid: as new DPD particles are inserted at inlet, the fluid particles get accumulated near inlet. The velocity profile near inlet is slightly deteriorated because of the increased number density.

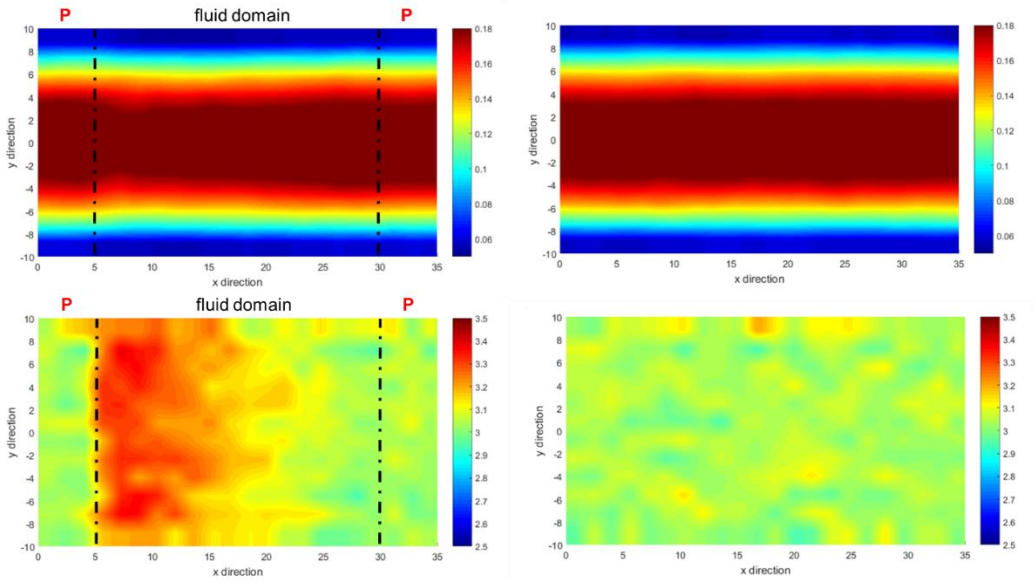


Figure II-13. Fluid velocity and density plot in x-y cross section of fluid domain. Left column: inflow/outflow BC is applied; fluid domain is between the dotted lines at $x = 5$ and $x = 30$; P represents the upstream and downstream periodic domain. Right column: periodic BC is applied on entire fluid domain.

To reflect three dimensional characteristic of fluid domain, the cross section of simulation domain is compared between I/O BC and in three planes along flow direction, $x = 10$, $x = 17.5$ and $x = 25$. In all six plots (Figure II-14), parabolic velocity profile is observed and comparable to each other. This implies that the I/O BC is able to successfully achieve the viscous DPD fluid flow in three dimensional scenario.

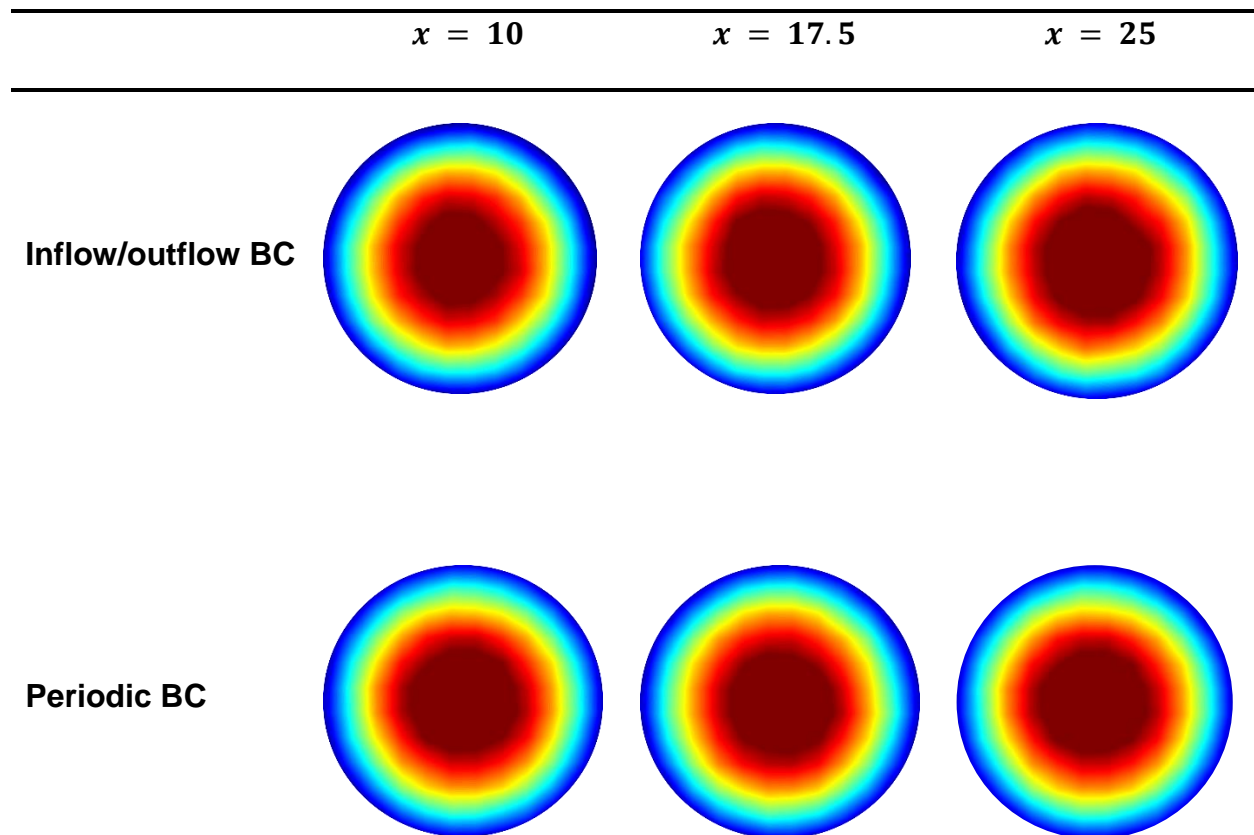


Figure II-14. Fluid velocity plot in x - z plane at three distinct locations along flow direction, $x = 10$, $x = 17.5$, and $x = 25$. Upper row represents fluid velocity in domain with applied inflow/outflow BC. Lower row represents results from periodic BC simulation.

The mechanical stress distribution in fluid domain is then studied. The fluid domain is divided into cylindrical bins along flow direction, and the per-atom fluid stress is averaged within each bin and pressure and shear stress distribution along flow direction are plotted (Figure II-15). A linear pressure gradient is achieved in I/O BC system. In contrast, pressure gradient does not exist in PBC system since the fluid flow is driven by body force. The shear stress is comparable in between I/O BC and PBC as a result of the fully developed parabolic velocity profile.

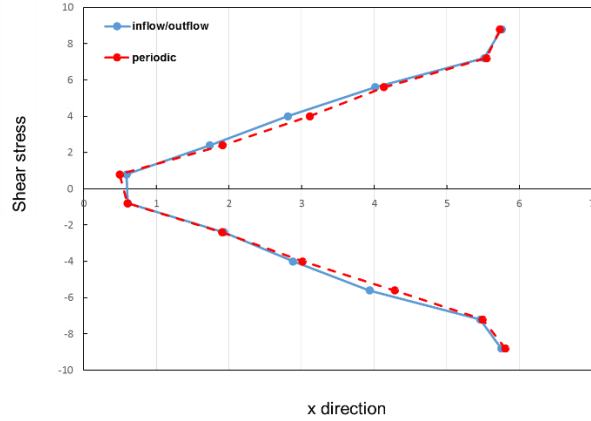
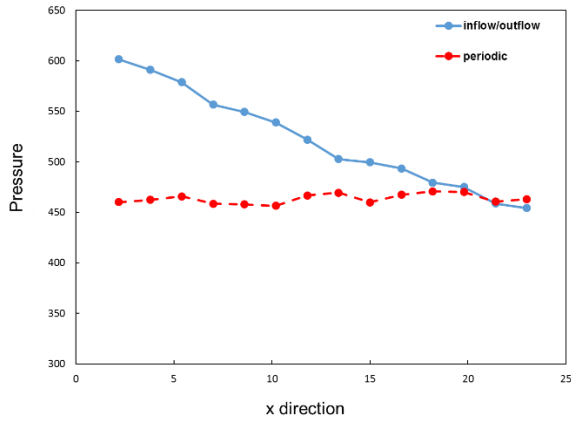
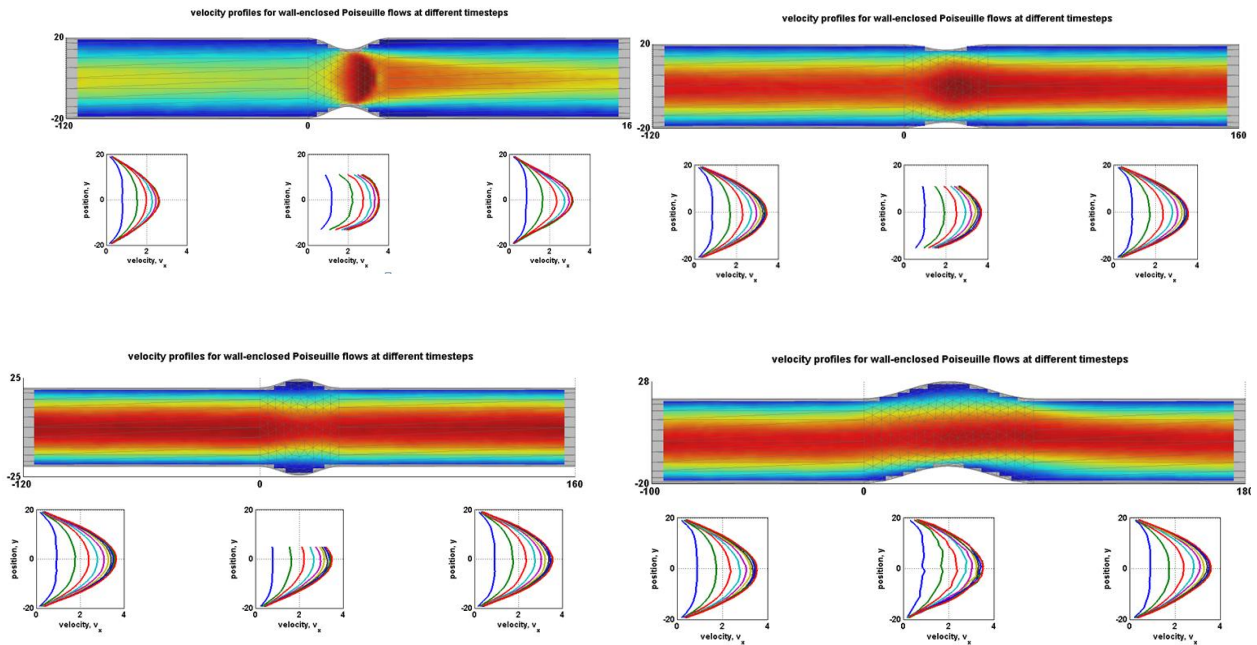


Figure II-15. Fluid pressure gradient and shear stress along flow direction for inflow/outflow and periodic fluid domain. A linear pressure gradient results from addition of inflow/outflow BC, whereas a flat pressure gradient comes from periodic BC. The shear stress distribution is the same for both cases.

2.3.5 Performance analysis of DPD fluid flow through five geometries



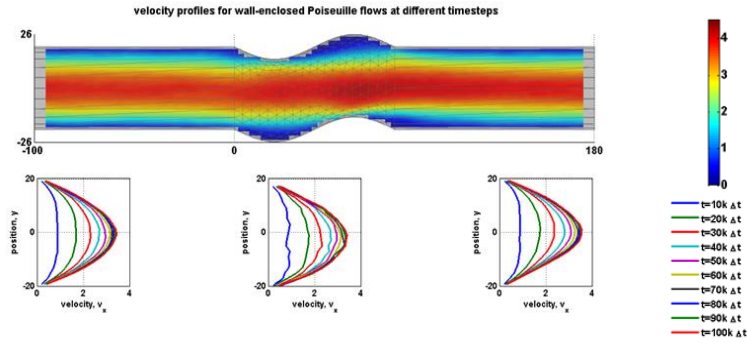


Figure II-16. Fully developed velocity profile for five geometries.

No-slip boundary condition is well preserved for all five cases (Figure II-16). The speedup and strong scalability are shown in Figure II-17. The five geometries demonstrate good speedup and strong scalability for both 1 million and 10 million systems. In the 1 million particle system, the strong scalability is reduced to around 80% as number of processors increases to 5,000. In the 10 million particle system, the strong scalability initially drops to around 85% with 2,000 and 3,000 processors, and gets closer to 100% with 5,000 processors.

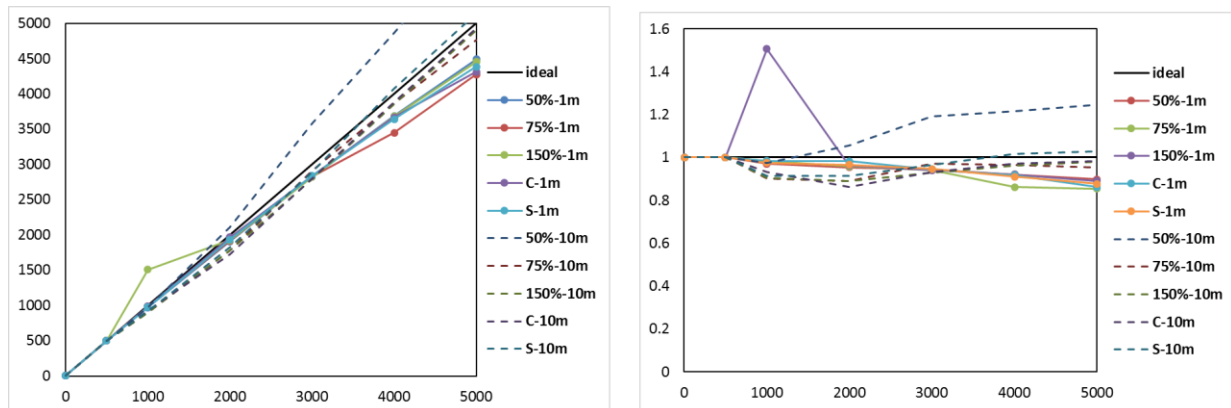


Figure II-17. Speedup and strong scalability for five geometries with system size 1 million and 10 million.

2.4 Discussion and conclusions

In the current work, the viscous fluid flow phenomena are recreated with the DPD model at mesoscopic scale. The fluid viscosity is determined by using counter-Poiseuille flow method, where the velocity profile generated from simulation are fitted to the analytical solution of plane-Poiseuille flow with Newtonian behavior. The parabolic velocity profile can be achieved with this method without imposition of physical walls and the adverse effects of explicit wall boundary condition can be avoided^{2,5}. However, when simulating blood flow through confined blood vessels, it is necessary to model physical walls enclosing the fluid domain, and associated no-slip boundary condition needs to be resolved.

The modeling of no-slip boundary condition requires correct boundary forces being applied onto fluid particles such that fluid particle near boundary would have zero velocity, and fluid number density near boundary is as uniform as bulk flow. Such boundary forces can be provided by frozen wall particles⁶³, or by extra fictitious particle-layer outside of fluid domain that enables the extension of velocity profile beyond the wall boundary⁹⁷. It is noted that construction of wall particles is not straightforward in a 3D complex geometry such as human vasculatures. Therefore, fictitious particle approach is adopted which only employs local fluid particle information, and implement it on each triangular elements of a complex wall. Although the introduction of extra boundary forces results in fluid number density fluctuations near the wall, it has negligible impacts on fluid particle in the bulk region. Besides, a reflection scheme is also required in order to prevent fluid particles from penetrating the wall, because of the soft interaction potential employed.

DPD bears compressible effect in modeling high Reynolds number flow¹⁵. In the current work, a speed of sound is determined for DPD fluid, beyond which the DPD fluid fails to match the analytical shear stress profile, and mild density gradient appears. Expanding DPD fluid flow

to higher Reynolds number requires a larger computational domain. Alternatively, the velocity limit can be increased by reducing the particle mass or increasing the system temperature ⁵⁹.

The platelet model demonstrates the characteristics of physiological platelets – deformation in the blood plasma, flipping motion under shear flow, interaction with each other and with walls, and acceleration through stenotic region. The limitation of the current work is the absence of other blood components such as red blood cells, which interact with platelets and have effects on platelet margination to the cell-free layer (CFL). CFL is a critical region where clot is formed as consequence of near-wall platelet motion and platelet-wall interaction ⁹¹. Another limitation is the lack of validation of mechanical and rheological properties of our platelet model by experiments, which can be mitigated by providing data from pipette aspiration ²⁵, dielectrophoresis (DEP) ⁴², optical tweezers ¹², and AFM ³⁸.

The cardiovascular system is an internal flow loop with curves and branches which create complex hemodynamic conditions ⁹⁹. Vascular pathologies in large arteries present aneurysms or stenosis that further change the hemodynamics within the blood vessel. DPD has been used to study the viscous fluids characteristics in three dimensional constricted geometries such as bulge, stenosis, and bifurcation with periodic boundary condition along flow direction ^{44,81}. However, the lack of suitable inflow/outflow BC hampers the advancement of DPD in simulating blood flow system with multiple outlets. PBC is mostly applied in DPD simulations where flow development attributes to imposition of body forces upon fluid particles. Any attempt to truncate the fluid domain would introduce artifacts to the fluid system, which leads to erroneous simulation results. The current work develops an inflow/outflow boundary condition that involves the insertion and removal of particles into and from the fluid system and also provides a boundary force scheme that applies correct boundary forces to fluid particles near inlet/outlet. The fully developed velocity

profiles can be achieved with I/O BC. The pressure gradient appears along flow direction, and fluid shear stress matches the solution based on PBC simulation. However, due to the compressibility effect of DPD fluid, fluid particles are accumulated at inlet which gives an increased number density near inlet. It was observed that if fluid flows at higher Reynolds number, the density gradient became more significant. Therefore, in order to maintain the DPD fluid within incompressible regime under inflow/outflow BC, the DPD forces fields need to be improved to include force terms that provide sufficient fluid pressure.

III. Improving the compressible effect of DPD-based blood flow simulations through severe stenotic microchannel

3.1 Introduction

DPD has demonstrated the hallmarks of viscous fluid flow properties that were verified by continuum-based simulation approach such as computational fluid dynamics (CFD) ^{15,40,81}. It is noted that most of the DPD simulations were conducted in straight and mild stenotic cylindrical or rectangular shaped geometries with limited Reynolds number. In human vasculatures, platelet aggregation and thrombosis can be triggered by arterial stenosis, and the maximum rate of platelet accumulation is increased with increasing stenosis severity ¹⁰⁰. Occlusions of greater than 75% in coronary artery can induce occlusive thrombi and generate symptoms of angina ^{11,21}. However, the DPD approach breaks down in approximating the incompressible viscous fluids through severe stenosis where fluid particles accumulate upstream of stenosis, and a density gradient appears along flow direction ^{18,105}. This is due to the compressibility effect emerged as a result of the soft interaction potential employed in the conventional DPD formula ^{59,92}.

Morse potential has been applied as a coarse-grained force field to model water ⁹ and blood ¹¹⁵ and was able to closely replicate the fluid properties. It was also applied in simulations such as polymer translocation through microchannel ²⁴, aggregation of red blood cells ^{14,46,111}, and molecular binding between platelet glycoprotein GPIb α and von Willebrand Factor (VWF) ⁷⁸. In the first case, the repulsive role of Morse potential was emphasized to avoid DPD particle interpenetration problem in polymer chains. In latter cases, the attractive part was employed to simulate cell-cell and molecule-molecule attractions. In the case of stenotic flows, a hard short-range repulsive force makes Morse potential a good candidate to improve the compressibility effects of the conventional DPD fluids. When fluid flow is being largely compressed in stenotic

region, Morse potential can provide a hard core for the DPD fluid particles to sustain the compression. Therefore, we introduced a hybrid DPD-Morse fluid model to better preserve the fluid incompressibility, in which the Morse potential is added to the conventional DPD force field. The particle interaction range is divided into two parts, an inner hard-core region where both Morse and DPD force fields are applied, and an outer soft layer where only DPD force field is exerted. We conducted a series of comparative studies to investigate the compressibility effects of DPD-Morse and DPD fluids. We first employed the counter-Poiseuille flow to study the viscous fluid flow development with periodic boundary condition. We then employed a 67% stenotic microchannel to investigate the influence of the compressibility effects in fluid flow properties under large compression. We compared the simulation results with CFD solutions for verification. After the fluid domain was examined, we embedded a rigid platelet model within the fluid domain to explore the effects of the two fluid models on platelet transport. Last, we computed the fluid stress accumulation along platelet flowing trajectory, which is an important indicator for predicting the potential damage to the platelets.

3.2 Methods

3.2.1 DPD-Morse fluid model

A new viscous blood plasma model is proposed which combines the Morse potential and conventional DPD force field. The Morse potential is being used in order to reduce the fluid compressibility.

A modified DPD formula is presented as

$$d\mathbf{v}_i = \frac{1}{m_i} \sum_{j \neq i}^N (\mathbf{F}_i^M dt + \mathbf{F}_i^C + \mathbf{F}_i^D dt + \mathbf{F}_i^R \sqrt{dt}) \quad (\text{III-1})$$

In equation (III-1), \mathbf{F}_i^M is the conservative force derived from Morse potential acting on particle i . \mathbf{F}_i^C , \mathbf{F}_i^D , \mathbf{F}_i^R are the conservative, dissipative and random forces of DPD force field acting on the particle i . \mathbf{v}_i and m_i are velocity and mass of particle i .

\mathbf{F}_i^M is expressed as

$$\mathbf{F}_i^M = 2D_0\alpha \left[e^{2\alpha(r_0-r_{ij})} - e^{\alpha(r_0-r_{ij})} \right] \mathbf{e}_{ij} \quad (\text{III-2})$$

where the first term is a repulsive term related to fluid pressure, and the second term is an attractive term related to fluid viscosity. D_0 is the well depth, α is a scaling factor, and r_0 is the zero-force length. $\mathbf{r}_{ij} = \mathbf{r}_i - \mathbf{r}_j$, $r_{ij} = |\mathbf{r}_{ij}|$, $\mathbf{e}_{ij} = \mathbf{r}_{ij}/r_{ij}$. The repulsive term is dominant when $r < r_0$ and the attractive term becomes more important when $r > r_0$ ⁵⁶.

DPD force field is expressed as

$$\mathbf{F}_i^C = a \left(1.0 - \frac{r_{ij}}{r_c} \right) \mathbf{e}_{ij} \quad (\text{III-3})$$

$$\mathbf{F}_{ij}^D = -\gamma w^D(r_{ij}) (\mathbf{v}_{ij} \cdot \mathbf{e}_{ij}) \mathbf{e}_{ij} \quad (\text{III-4})$$

$$\mathbf{F}_{ij}^R = \sigma w^R(r_{ij}) \xi_{ij} \mathbf{e}_{ij} \quad (\text{III-5})$$

$$w^D(r_{ij}) = [w^R(r_{ij})]^2 = \left(1.0 - \frac{r_{ij}}{r_c} \right)^{2k} \quad (\text{III-6})$$

where F_i^C contributes to fluid pressure, F_{ij}^D contributes to fluid viscosity, and F_{ij}^R mitigates the missing degree of freedom after coarse-graining. a , γ , σ are the strength of conservative, dissipative and random forces. ξ_{ij} is a random number with zero mean and unit variance. $\mathbf{v}_{ij} = \mathbf{v}_i - \mathbf{v}_j$ ²³.

Two cutoff distances r_c^M and r_c are defined, r_c^M is the cutoff for Morse potential, r_c is the global cutoff, and $r_c^M < r_c$. The Morse potential plays a significant role as the inter-particle

distance is reduced to less than r_c^M when fluid is being compressed. DPD force field is valid within r_c . Zero-force length r_0 is set the same as r_c^M .

3.2.2 Parameterization of DPD-Morse potential using counter-Poiseuille flow

Characteristic fluid flow phenomena in straight microchannels have been achieved by DPD fluid model with parameter set $a = 25.0$, $\gamma = 67.5$, $k = 0.25$, $r_c = 1.7$, $k_B T = 1.0$, number density $n = 3.0$. To minimize the compressible effect of DPD fluid flowing through severe stenotic microchannel, given the same DPD parameter set, different parameter sets of Morse potential are explored. Three parameters are present in Morse potential: scaling factor α , well depth D_0 , and zero-force length r_0 . α controls the potential width. When α is increased, both repulsive term and attractive term become steeper which lead to a narrower potential well. The parameter space of α can be from 0.5 to 2. Here, $\alpha = 0.5$ and $\alpha = 1.0$ were selected to achieve a gentle change of Morse potential in the repulsive range. D_0 is the secondary factor that affects the steepness of repulsive term at a fixed r_0 . When α is determined, the parameter space of D_0 is set as [10, 100, 200, 400, 600]. For DPD fluid with number density $n = 3.0$, the average inter-particle distance is determined as 0.69, the cubic root of system number density. The parameter space of r_0 is therefore selected as [0.6, 0.8, 1.0, 1.4, 1.7].

In our simulations, counter-Poiseuille flow was employed to perform the parameterization of Morse potential, with the objective of preserving fluid dynamic viscosity and increasing system pressure. The fluid dynamic viscosity of DPD fluid is attributed to the dissipative term of DPD force fields, and that of DPD-Morse fluid is resulted from both the dissipative term of DPD force fields and the attractive term of Morse potential. The pressure of DPD fluid is provided by the conservative term of DPD force field, and that of DPD-Morse fluid is given by the conservative term of both DPD force fields and Morse potential. The simulation domain was $30 \times 30 \times 30$,

which was divided into two symmetric sections with a pair of body forces $g = 2.0$ applied to the fluid particle of each section in opposite directions^{5,81}. B was applied in three orthogonal directions. The integration timestep was $dt = 5e - 4$. Fully developed parabolic velocity profile was achieved after simulation of 10,000 timesteps. For post-processing, the 3D simulation box was divided into 60 vertical bins along x direction with side length of 0.5, where the physical quantities of each fluid bin were obtained by averaging all particles information in each bin for 5,000 timesteps. The dynamic viscosity μ was acquired by fitting the velocity profile from simulation to the analytical solution. The parameter set was considered ineffective if the fluid velocity profile deviated from the conventional DPD fluid. When the fluid velocity profile was the same, the parameter set was selected depending on the system pressure (Figure III-1). α was first set as 1.0. r_0 was selected as 0.6 and 0.8. The fluid velocity and pressure were compared in between different sets of parameters. When $r_0 = 0.6$, the change of D_0 does not affect the fluid properties compared to the DPD solution; when $r_0 = 0.8$, by changing D_0 , the fluid velocity profile of the DPD-Morse fluid deviated from the DPD solution. To maintain the same fluid velocity profile, α was reduced to 0.5. When $r_0 = 0.8$, only $D_0 = 100$ allows the DPD-Morse fluid to maintain the same fluid velocity profile. With $\alpha = 0.5$ and $D_0 = 100$, r_0 was further adjusted to increase the system pressure. With $r_0 = 1.4$, the DPD-Morse fluid achieved higher system pressure as compared to the DPD fluid while preserving the fluid velocity. When r_0 was further increased to 1.7, the DPD-Morse fluid deviated from the DPD fluid velocity profile.

The final parameters were selected as $\alpha = 0.5$, $D_0 = 100$, $r_0 = 1.4$. With this parameter set for DPD-Morse fluid, the fluid flow properties, i.e., velocity, number density, shear stress, pressure, and radial distribution functions were demonstrated and compared in between DPD and DPD-Morse fluids (Figure III-2). Furthermore, a compression simulation was conducted where 5%

compression was applied along x direction to the original fluid system. The isothermal compressibility κ_T was computed based on $\kappa_T \approx \left(\frac{\ln(\rho_2/\rho_1)}{P_2 - P_1} \right)_T$, where ρ_1 and P_1 were original system quantities, and ρ_2 and P_2 were computed from compressed system¹¹⁶. The speed of sound was determined by $c = \sqrt{\frac{\partial P}{\partial n}}$.

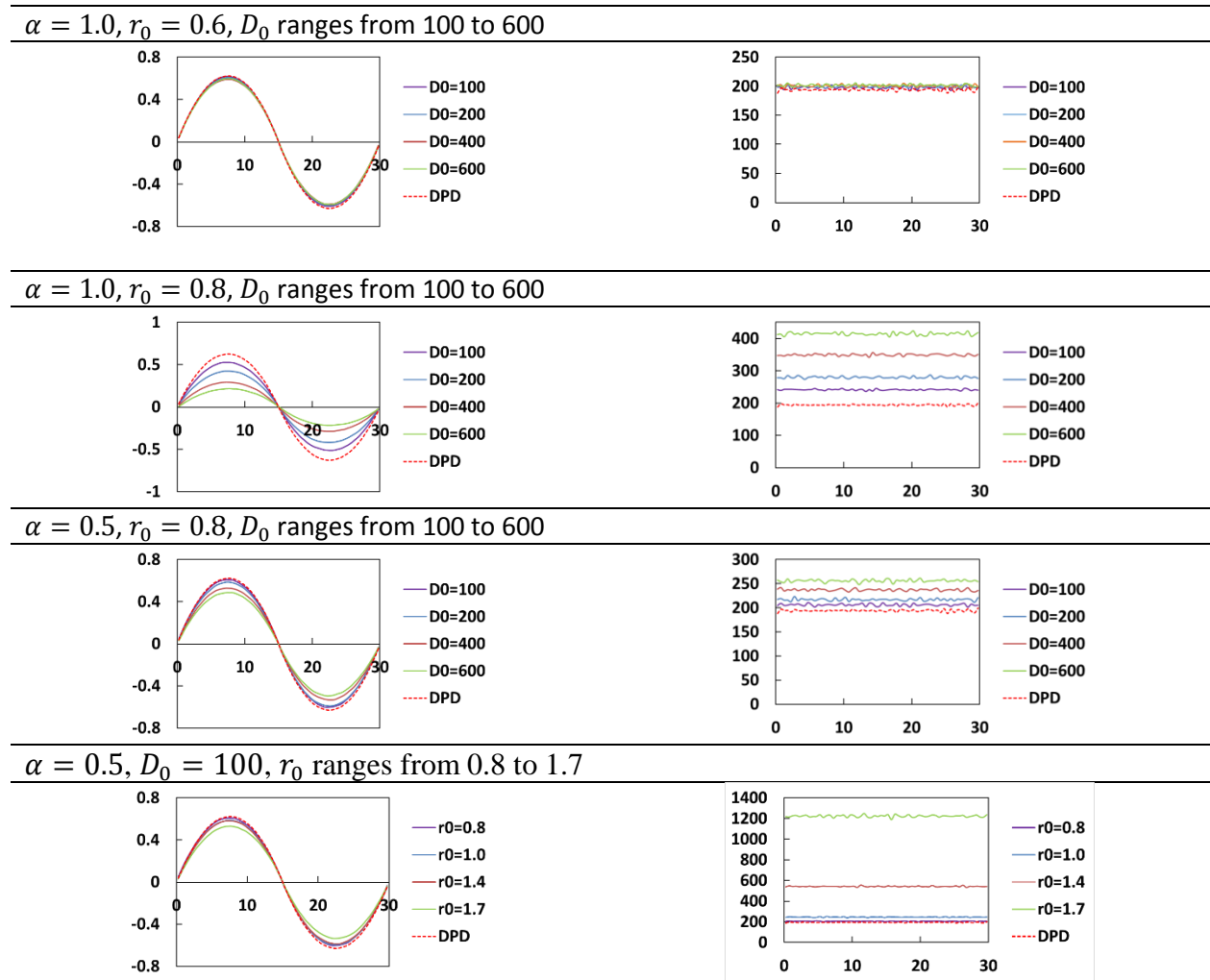


Figure III-1. Velocity (left) and pressure (right) distribution of DPD-Morse fluid under counter-Poiseuille flow.

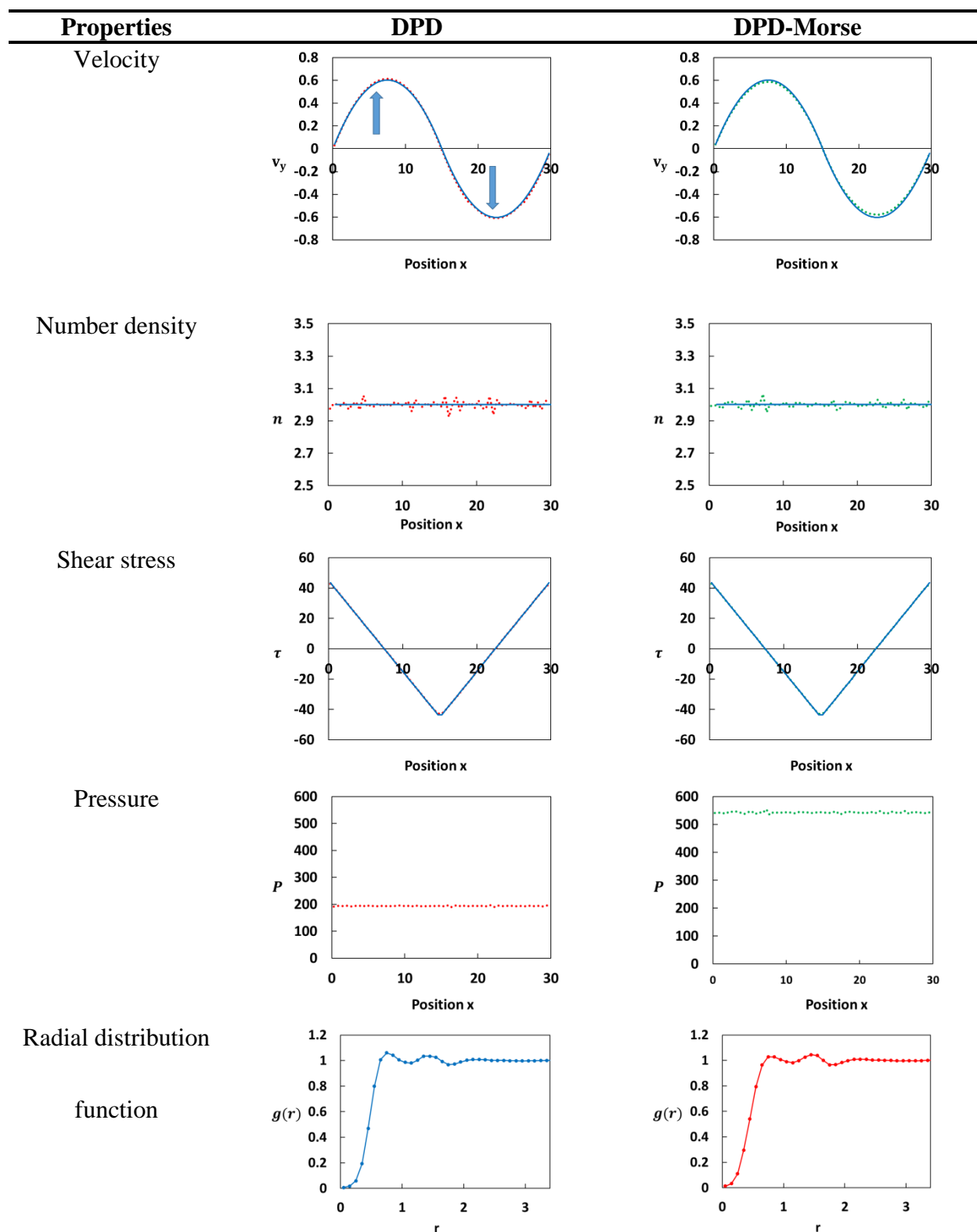


Figure III-2. Counter-Poiseuille flow of DPD and DPD-Morse fluids. The system dimensions are $30 \times 30 \times 30$, number density $n=3.0$. A body force $g_y = \pm 2.0$ is applied along the y direction. The system is divided into 60 vertical bins along the x direction with side length of 0.5, and fluid

particle velocity, number density, shear stress, and pressure are averaged in each bin for 5000 timesteps after the flow is fully developed (all numbers appear in dimensionless units).

3.2.3 Stenotic microchannel simulations with no-slip boundary condition

A 67% stenotic microchannel was constructed in order to study the compressibility effects of DPD fluids flowing in a stenotic channel through a severe constriction (Figure III-3). The stenosis degree was defined as the ratio between the occluded cross-section area and the full cross-section area. The length L , height H , and width W of the microchannel was $120 \mu m$, $30 \mu m$, $30 \mu m$, respectively. The microchannel consists of three sections, an upstream section with $L = 44 \mu m$, $H = 30 \mu m$, and $W = 30 \mu m$; a downstream section with same dimensions as the upstream section; and a stenotic section with $L = 32 \mu m$, $H = 10 \mu m$, and $W = 30 \mu m$. The fluid flow was driven along the x direction by a body force $g_x = 2.0$. A no-slip boundary condition was applied on the top walls composed of 10 triangular elements, and on the bottom wall of 2 triangular elements. Same no-slip boundary condition was applied in the DPD-Morse fluid simulation^{81,117} (Figure III-4). The platelet was modeled as a rigid ellipsoid with 444 particles with dimension $4 \times 4 \times 2$ in μm ⁸¹. Physical quantities in dimensionless units were further converted into physical units for the interpretation of fluid flow properties, platelet transport dynamics, and the fluid stress accumulation (SA) along the platelet trajectory¹¹⁷. To visualize fluid number density, velocity and shear stress, the simulation data was spatially averaged over a two-dimensional grid of $dx = 0.5$ and $dy = 0.5$, and temporally over 50,000 timesteps.

To compute SA, the platelet centroid $\mathbf{r}(t)$ was identified at a constant time interval, where the starting time point t_0 was recorded when the platelet was released into the fluid, and the finished time point t_f was recorded when the platelet passed through the outlet of microchannel. SA was computed as the time integral of a scalar fluid stress along the platelet transport trajectory,

$$SA = \int_{t_0}^{t_f} \tau(\mathbf{r}(t)) dt = \int_{t_0}^{t_f} \tau(x(t), y(t), z(t)) dt \quad (\text{III-7})$$

where t_0 and t_f are the initial and final time points of platelet transport, $\tau(\mathbf{r}(t))$ is the scalar fluid stress at platelet centroid $\mathbf{r}(t)$, $t \in [t_0, t_f]$. The scalar fluid stress $\tau(\mathbf{r}(t))$ is converted from the fluid stress tensor using the formula III-8:

$$\tau = \frac{1}{\sqrt{3}} \sqrt{\tau_{xx}^2 + \tau_{yy}^2 + \tau_{zz}^2 - \tau_{xx}\tau_{yy} - \tau_{xx}\tau_{zz} - \tau_{yy}\tau_{zz} + 3(\tau_{xy}^2 + \tau_{yz}^2 + \tau_{xz}^2)} \quad (\text{III-8})$$

Following previous work, the fluid stress tensor $\tau(\mathbf{r}(t))$ was computed using spatial-temporal averaged virial stress^{65,88,117}. Along the spatial scale, the whole microchannel was discretized into bins in xy -plane. Each bin has dimension $1 \times 1 \times 30$. The fluid bin was selected which enclosed the platelet centroid $\mathbf{r}(t)$. Each particle within the bin has a per-particle fluid stress tensor,

$$\tau_{ab} = -\frac{1}{2} \sum_{n=1}^{N_p} (r_{1a}F_{1b} + r_{2a}F_{2b}) \quad (\text{III-9})$$

where r_1, r_2 and F_1, F_2 are the positions and pairwise forces of two interacting fluid particles i and j . a and b take on values x, y and z . N_p is the number of neighbors of particle i . τ_{ab} is the virial stress with physical unit of stress \times volume. Along temporal scale, the fluid stress τ_{ab}^i for each particle i is averaged over $2.06ms$. Then the spatial-averaged fluid stress tensor τ_{ab} for each bin is computed as by averaging the per-particle stress τ_{ab}^i for all particles i within this bin.

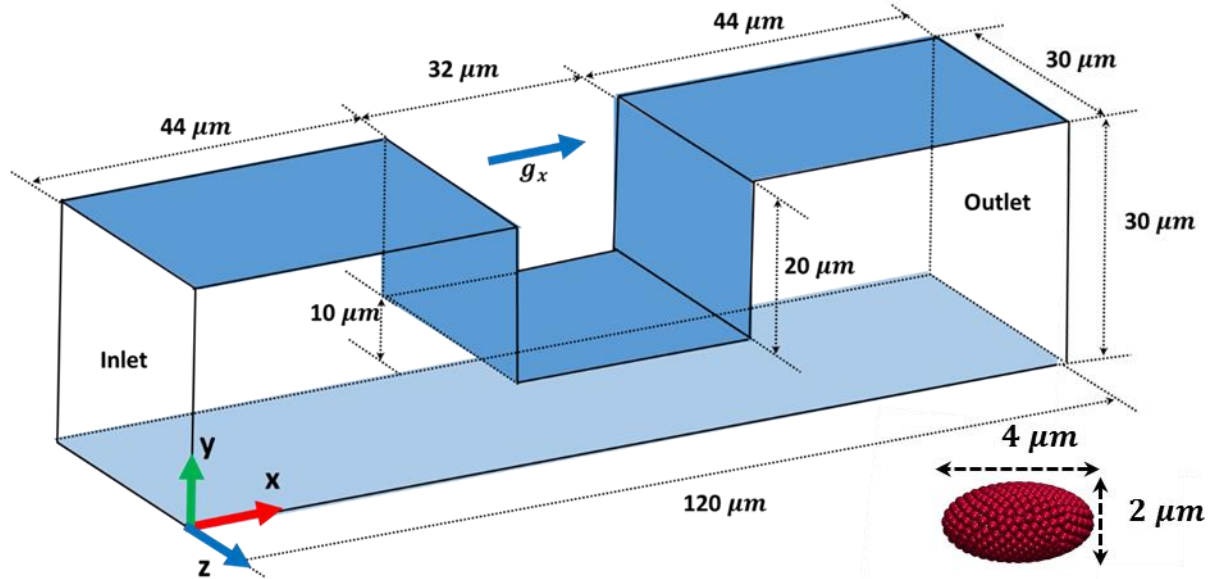


Figure III-3. Stenotic microchannel of 120 μm length, 30 μm height, and 0 μm width. The upstream is 44 μm in length, 30 μm in height, and 30 μm in width; the downstream section has the same dimensions as the upstream section; the stenotic section is 32 μm in length, 10 μm in height, and 30 μm in width. The fluid flow is along x direction driven by a body force g_x . No-slip boundary condition is applied on the top walls composed of 10 triangular elements, and the bottom walls with 2 triangular elements. The platelet is modeled as a rigid ellipsoid particle with dimensions of 4 \times 4 \times 2 μm .

3.2.4 Two-dimensional continuum fluid simulation

As a reference case, a computational fluid dynamics (CFD) model was solved and its results were compared to the DPD and DPD-Morse models. For this model we assumed that it can be solved on a two-dimensional plane because the channel is infinitely wide and there is no influence of the side walls. The fluid was assumed to be incompressible Newtonian (ρ of 1060 kg/m^3 , μ of 0.00119 $\text{Pa}\cdot\text{s}$). The inlet and outlet velocity profiles were based on the inlet velocity profile of the DPD-Morse model and were defined with a parabolic function. Navier–Stokes continuum equations were solved using finite volume method. The domain was discretized using homogenous-quadratic mesh with cell size of 0.1 μm (100 cells in the narrowest region, 296,000 cells in total). The model was solved in ANSYS Fluent 17.0 with coupled pressure-

velocity scheme and second order discretization. The CFD data was plotted on the same post-processing grid as particle simulations.

3.2.5 Unit conversion from dimensionless to physical units

The model units are converted from dimensionless to physical units¹¹⁷. The reference length $\sigma_r = \frac{D_p}{D_p^*}$, where $D_p = 4 \mu m$ and $D_p^* = 4$. The reference mass $m_r = \frac{\rho \sigma_r^3}{\rho^*}$, where the fluid density of blood plasma $\rho = 1060 kgm^{-3}$, and the particle density in the model is $\rho^* = 3$. The reference velocity $v_r = \frac{v}{v^*}$, where $v = 3.6 mm/s$ corresponds to $v^* = 0.3$. The reference time $t_r = \frac{\sigma_r}{v_r}$.

3.3 Results

We first compared the DPD-Morse fluid to the DPD fluid using counter-Poiseuille flow. A series of fluid physical quantities were investigated, including velocity, number density, shear stress and pressure. We also performed the compression simulation to study the isothermal compressibility and speed of sound of the two types of fluids. This was followed by the fluid simulations through the 67% stenotic microchannel, where the compressibility effects were evaluated for the two fluids by examining the fluid number densities in the system. We also compared the velocity and shear stress profiles in the two flow fields. The results were further verified by comparing the results of particle-based simulations with CFD. Furthermore, we embedded a single platelet model into the fluid domain, to compare the platelet transport behavior, including platelet traversing velocities and traversing period. Finally, we computed the fluid stress accumulation along the platelet transport trajectory within one period, and examined the difference between the DPD-Morse and DPD fluids in predicting the shear-induced stress accumulation.

3.3.1 Fluid flow properties in counter-Poiseuille flow

DPD-Morse fluid is shown to have the same fluid flow properties as DPD fluid under counter-Poiseuille flow condition (Figure III-2): parabolic velocity profiles are achieved and are in good agreement with the analytical solution; stable density fluctuations are observed around system average number density; the fluid shear stresses are mapped closely with the analytical solution. Note that the system pressure of DPD-Morse fluid is higher than that of the DPD fluid as a result of stronger repulsive force in between fluid particles in DPD-Morse fluid. The radial distribution function (RDF) of the DPD-Morse fluid closely resembles that of the DPD fluid.

The compression simulation presents a much smaller isothermal compressibility of the DPD-Morse than that of the DPD fluid: $\kappa_T^{DPD-Morse} = 0.015/Pa$, $\kappa_T^{DPD} = 0.046/Pa$ so $\kappa_T^{DPD-Morse} \approx 0.33\kappa_T^{DPD}$ which demonstrates that DPD-Morse fluid is more resistant to compression under the same condition.

The speed of sound for the DPD-Morse fluid is higher than that of the DPD fluid, where $c^{DPD-Morse} = 0.23 m/s$, and $c^{DPD} = 0.14 m/s$. This corresponds to Mach number $Ma^{DPD-Morse} = 0.03$ and $Ma^{DPD} = 0.05$ in the case of the counter-Poiseuille flow correspondingly. Both fluids have a dynamic viscosity $\mu = 1.197 mPa \cdot s$. Reynolds number is 0.0482. DPD-Morse fluid reduces the compressibility effect of conventional DPD fluid, while preserving the viscous fluid characteristics.

3.3.2 Fluid flow properties in the 67% stenotic microchannel flow

Fluid simulations through the 67% stenotic microchannel were conducted with the two fluid models. The no-slip boundary condition for the DPD-Morse fluid was achieved by creating fictitious fluid particles which interact with real fluid particles near boundaries through DPD forces⁸¹. No-slip condition was achieved for the fluid particles in the near wall vicinity, but the fluid

density was increased close to 1500 kg/m^3 (Figure III-4). This fluid density artifacts were observed by prior studies and can be modulated by modifying the repulsive force term imposed at the boundary^{15,63,97}. The current work does not intend to address this problem since the number density in the bulk flow domain was not affected by the near wall density fluctuations.

The system number density was compared between the DPD-Morse and the DPD fluids (Figure III-5). In the DPD-Morse fluid, a relatively uniform density distribution was observed. In the DPD fluid, a significant difference in fluid density was observed between the upstream and downstream sections of microchannel. The fluid particles accumulated dramatically at the upstream. The non-uniform density distribution of the DPD fluid leads to less accurate prediction of fluid quantities including velocity and shear stress. Figure III-6 shows the velocity field of the stenotic microchannel, simulated by CFD, DPD-Morse, and DPD models. The CFD velocity field was used as a benchmark result. The DPD-Morse fluid resembles the CFD solution. It has a relative uniform velocity distribution in the stenotic section, while the DPD fluid has a large discrepancy in velocity field between upstream and downstream sections. The highest velocity magnitude was found at the exit of stenotic section in the DPD fluid. This is caused by the dramatic decrease of the fluid number density in the downstream section, which provides smaller resistance to the fluid particles exiting the stenosis. The change of fluid density in the microchannel leads to variations in the fluid viscosity within the flow field (Figure III-7). Along the platelet flowing trajectory, the fluid viscosity of the DPD-Morse fluid is more uniform with only gradual changes compared with the more abrupt changes in the DPD fluid, and is closer to the blood plasma viscosity of $1.197 \text{ mPa} \cdot \text{s}$. The fluid shear stress distribution was shown in Figure III-8. Symmetric fluid shear stress was observed in the DPD-Morse fluid domain, and is close to the CFD solution. The fluid shear stress was deteriorated in the DPD fluid domain near the exit of the stenotic section.

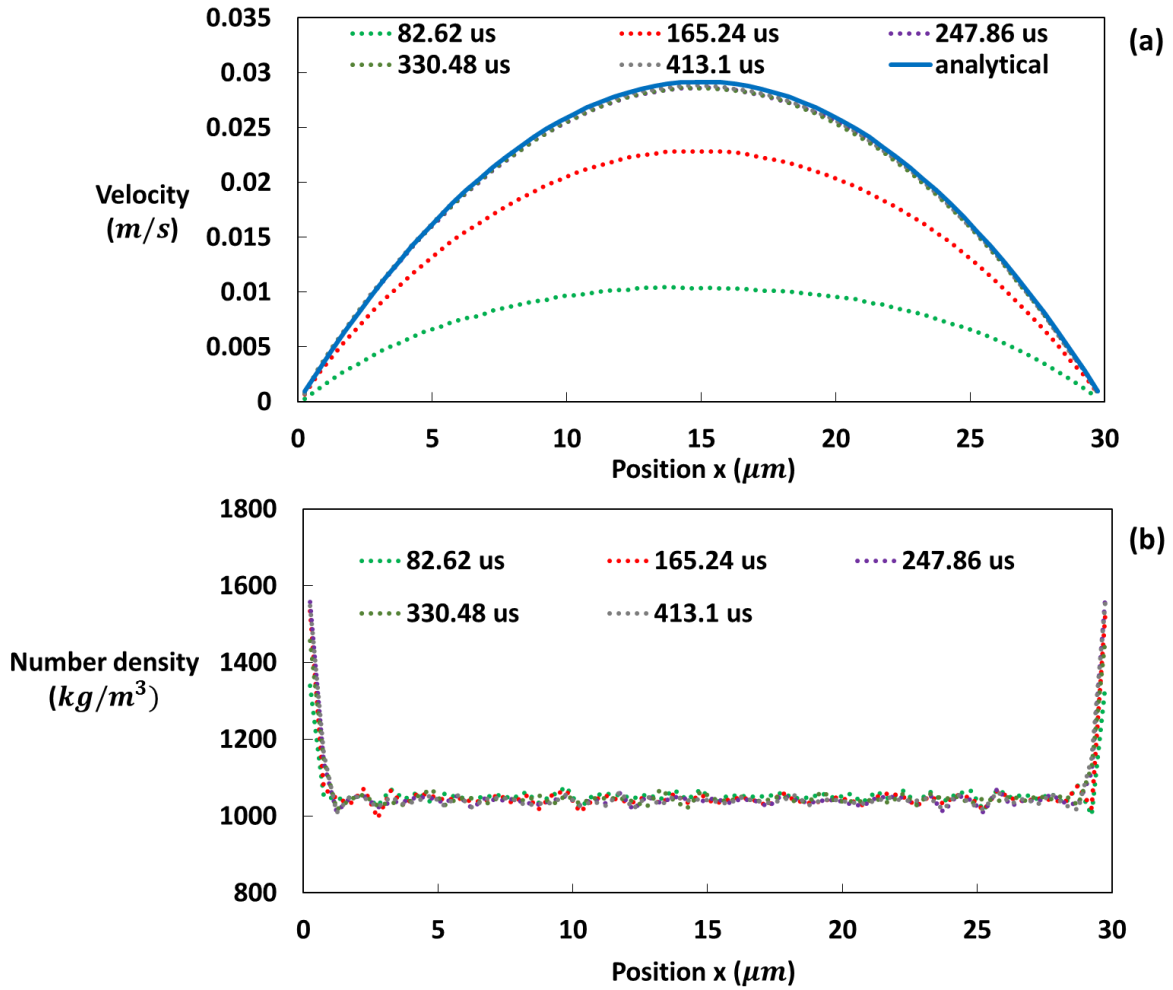


Figure III-4. No-slip boundary condition for the DPD-Morse fluid. Fluid velocities and number densities are shown at five time points: 82.62, 165.24, 247.86, 330.48 and 413.1 μs . The velocity profiles are compared to the analytical solution (blue solid line). The blood plasma density is 1060 kg/m^3 .

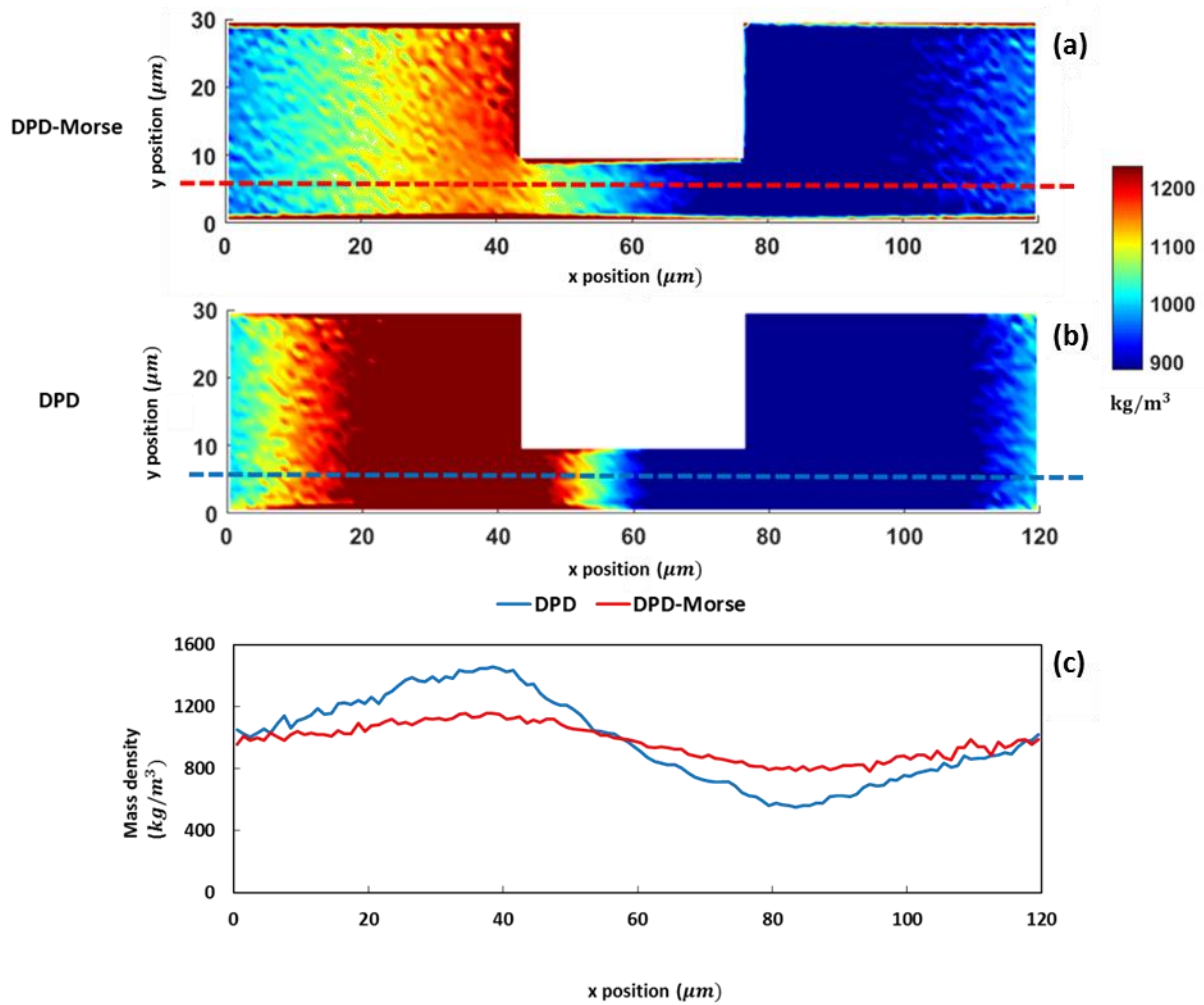


Figure III-5. Fluid density comparison of the DPD and the DPD-Morse fluids in 67% stenotic microchannel. (a) and (b) show an xy cross-section of the fluid density of the DPD-Morse and the DPD fluids, correspondingly. (c) shows the observations of fluid density gradient along flow direction at $y=5.5$, where the blue line represents the DPD fluid, and the red line represents the DPD-Morse fluid.

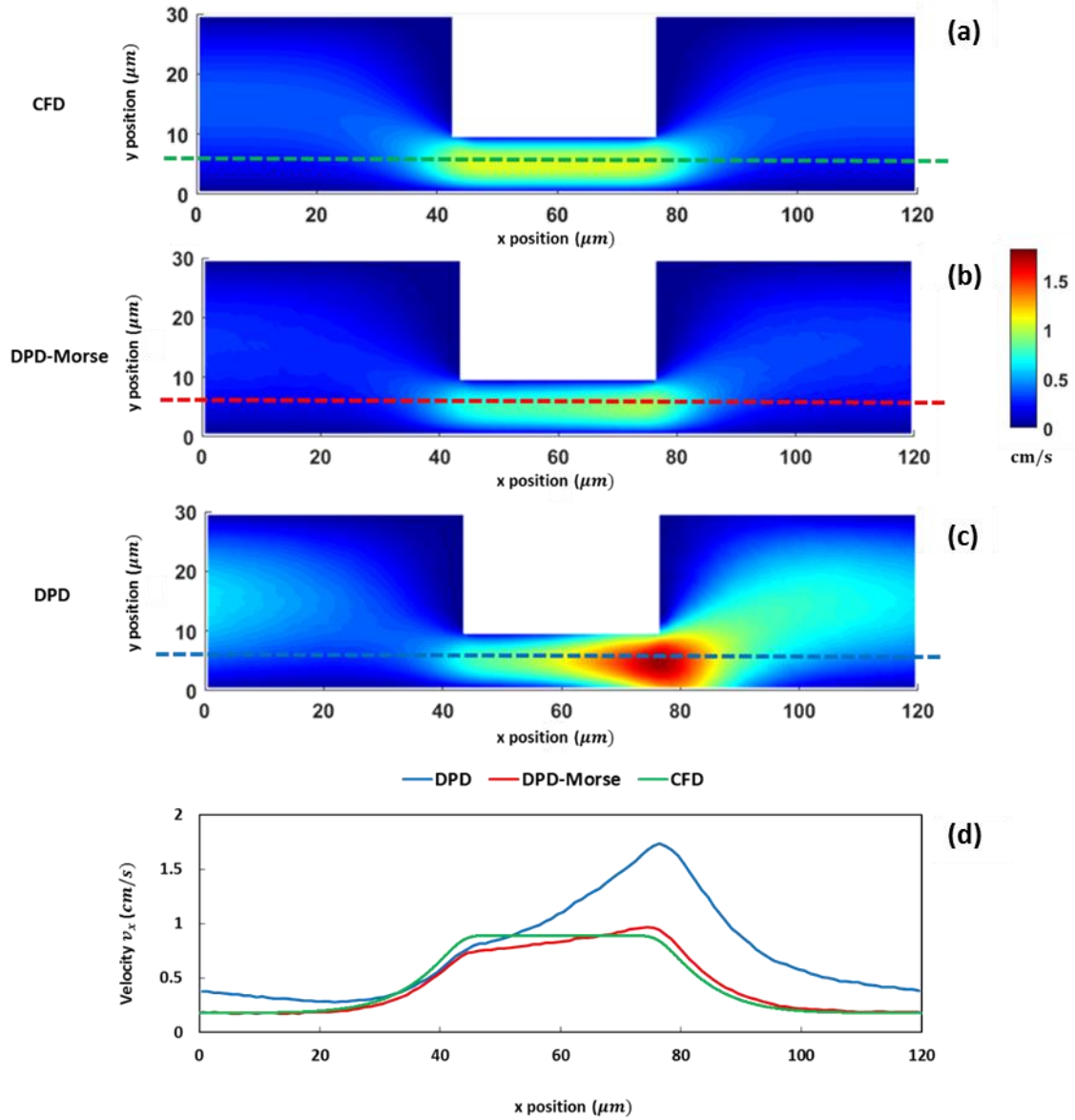


Figure III-6. Velocity comparison of CFD, DPD-Morse, and DPD fluids in the 67% stenotic microchannel. (a-c) represent xy cross-section view of velocity v_x of the three fluid models. (d) shows the velocity change long flow direction at $y=5.5$ (green (CFD), red (DPD-Morse), and blue (DPD)).

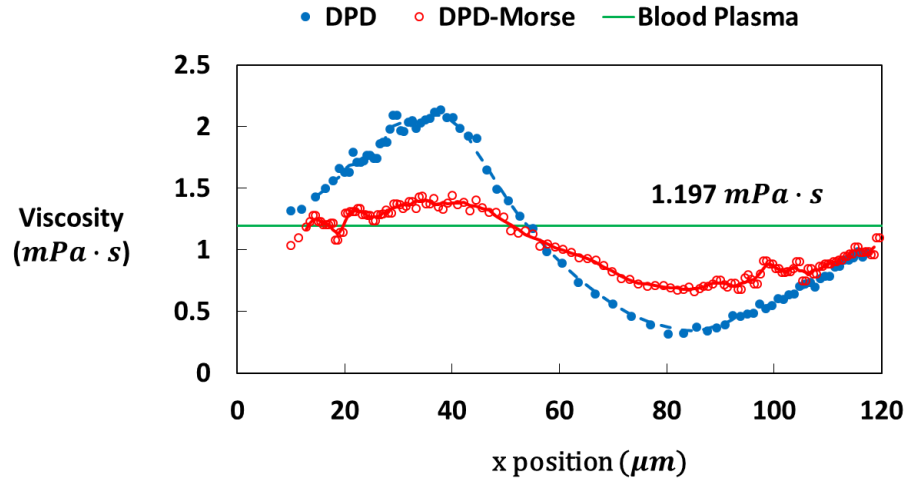


Figure III-7. Fluid viscosity change along a platelet flow trajectory in reference to blood plasma viscosity of 1.197 mPa·s (the blue and red lines represent the DPD and DPD-Morse fluids, respectively.). The mean squared error for the DPD-Morse fluid is 0.08, and for the DPD fluid is 0.39.

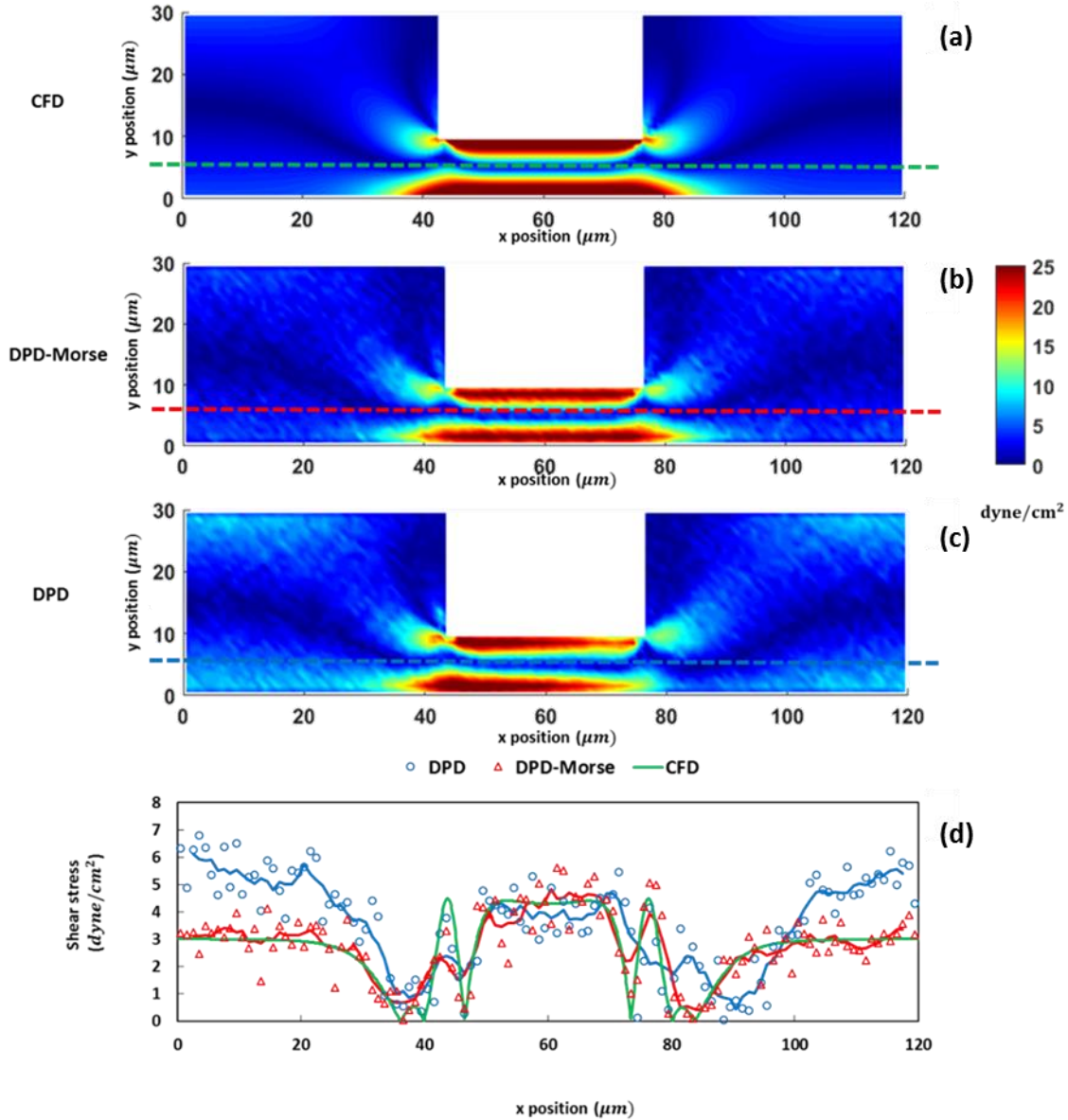


Figure III-8. Shear stress comparison of the CFD, DPD-Morse and DPD fluids in the 67% stenotic microchannel. (a-c) represent xy cross-section of the shear stress of the three fluid models. (c) shows the shear stress change along the flow direction at $y=5.5$. (green (CFD), red (DPD-Morse), and blue (DPD)).

3.3.3 Platelet transport dynamics in 67% stenotic microchannel flow

The platelet transport properties in the DPD and the DPD-Morse fluids were compared by tracking the trajectory of a single platelet flowing through the stenotic microchannel (Figure III-9

and III-10). The velocity component v_x is shown in Figure III-9 (a). The platelet trajectory through the microchannel is shown in Figure III-9 (b). In the upstream domain, the platelet flowing in the DPD fluid has a slightly higher v_x . When the platelet approached the stenotic section, it started to accelerate with a stronger acceleration in the DPD fluid. The platelet continued to accelerate through the stenotic section, where the DPD fluid reached a maximum v_x at the exit of the stenotic section which twice that achieved with the DPD-Morse fluid, after which the platelet began to slow down. The y component of platelet velocity v_y in both types of fluids is close to zero at upstream, stenotic, and downstream sections (Figure III-9 (c)). It becomes evident when platelet approached and exited the stenotic section.

The difference in the platelet transport period through the stenotic microchannel is demonstrated in Figure III-10. The red platelet was immersed in the DPD-Morse fluid, and the yellow one in the DPD fluid. The two platelets are initially positioned at same location at 0 ms (two platelets are overlapped in the first subplot of the figure). The platelet in the DPD fluid moved faster than in the DPD-Morse fluid, and the discrepancy appears gradually as the platelet traveled along the microchannel. At 18 ms , it already passed the outlet and starts a new period for the DPD fluid, whereas the platelet in the DPD-Morse fluid only exited from the stenotic section at that time instant. The platelet transport results are consistent with the significant density and velocity difference between the DPD-Morse and the DPD fluids shown in Figure III-5 and III-6.

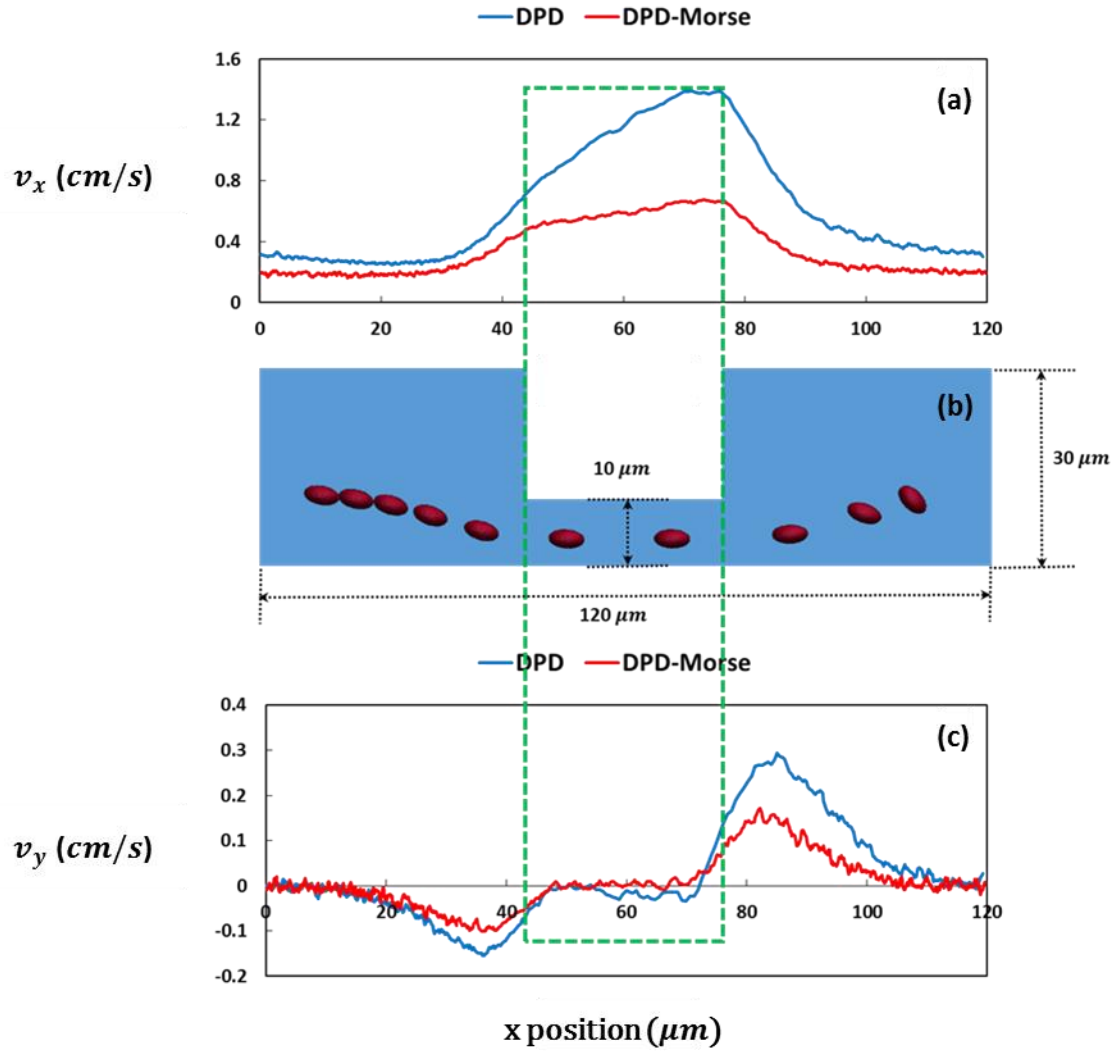


Figure III-9. (a) shows the x-component of platelet flowing velocity v_x . (b) shows the platelet transport trajectory and (c) y-component of platelet flowing velocity v_y .

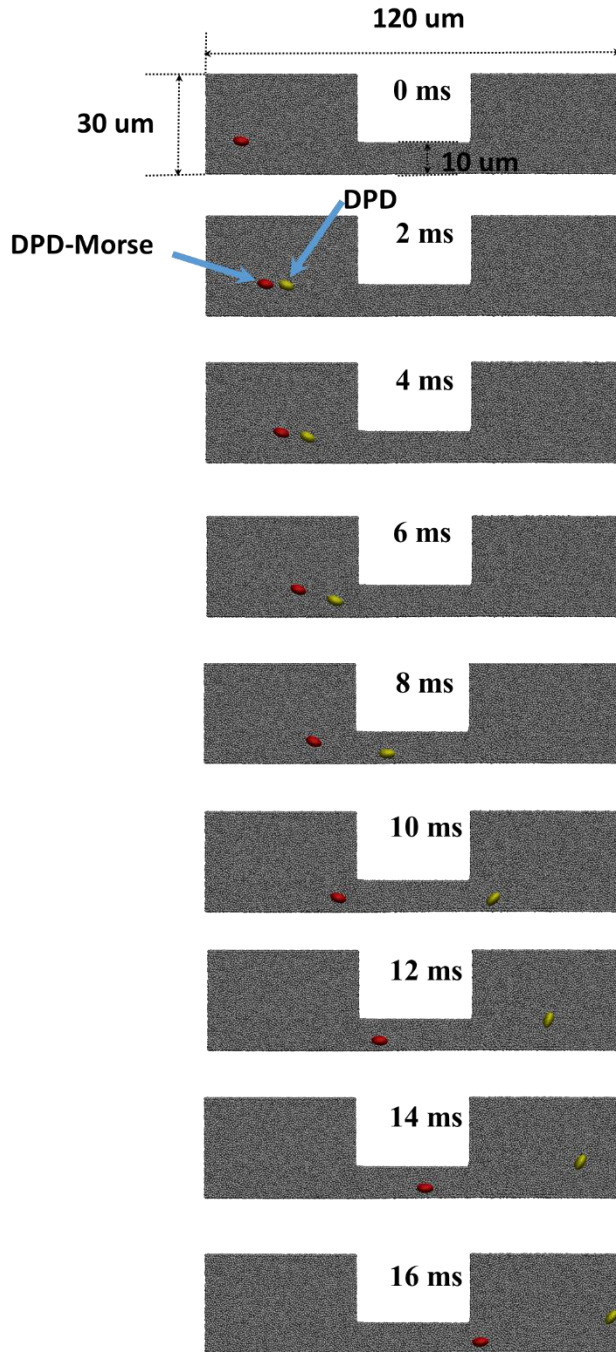


Figure III-10. Snapshots of platelet passing through the stenotic microchannel at different time points. The red platelet is immersed in the DPD-Morse fluid, and the yellow one in the DPD fluid. At 0 ms (i.e., the first subplot), the red and yellow platelets are overlapped.

3.3.4 Fluid stress accumulation along platelet flowing trajectory

Figure III-11 (a) shows the spatial change of scalar fluid stress along platelet flowing trajectory. Platelet immersed in both fluids started with same fluid stress level. As a platelet approached the stenotic section, the platelet in the DPD fluid experienced a higher fluid stress level close to 25 dyne/cm^2 but for the DPD-Morse fluid the fluid stress was on the level of 15 dyne/cm^2 . In the stenotic region, the DPD fluid shows a larger stress gradient than the DPD-Morse fluid. This resulted in a lower fluid stress level for the DPD fluid at exit of stenosis. In the downstream section, the fluid stress levels became similar for two fluids.

The platelet in the DPD fluid took 16.5 ms from the release to the pass of outlet boundary, and about 30 ms in the DPD-Morse fluid. The stress accumulation was then computed and presented in Figure III-11 (b). Before platelets entering the stenotic section, the stress accumulation was close in between two types of fluids. As platelets approached the entrance of stenosis, both fluids demonstrated a sudden increase of stress accumulation level. Once the platelet entered the stenotic section, the stress accumulation began to slow down. It was also observed that the stress accumulation in the DPD-Morse fluid exceeded the DPD fluid. In the downstream section, the stress accumulation rate became similar between two types of fluids.

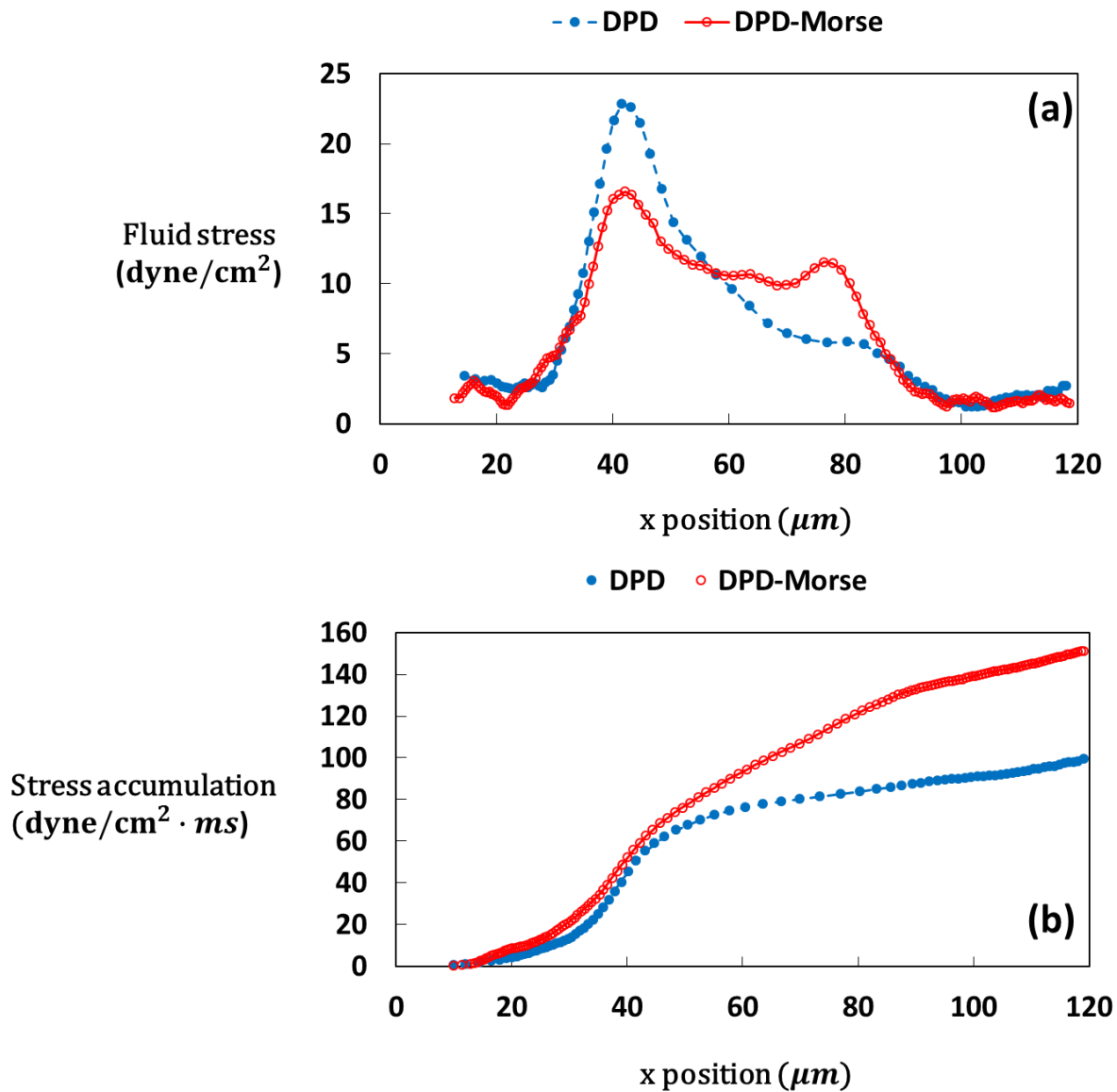


Figure III-11. (a) Scalar fluid stress along the platelet flow trajectory in the DPD and DPD-Morse fluids. (b) Fluid stress accumulation (SA) along the platelet flow trajectory.

3.4 Discussion and conclusions

DPD has been applied successfully in modeling red blood cells and platelets immersed in viscous blood plasma through 3D complex geometries such as human vasculatures and prosthetic cardiovascular devices^{13,81,103,117}. It demonstrates the hallmarks of viscous fluid flow characteristics with the imposition of no-slip boundary conditions at the wall^{63,81}. However, the compressibility effect limits the application of DPD to straight or mild stenotic microchannels with small fluid compression. The compressibility effect becomes significant as the degree of stenosis increases, and can lead to a fluid density gradient in the flow direction^{17,105}. This prevents DPD method from correct description of viscous fluid flow in severe stenosis and accurate prediction of platelet dynamics and activation potential in such scenario^{58,90}.

The compressibility effect of DPD fluid appears as a result of the soft interaction potential employed in between fluid particles^{15,59}. The soft potential cannot avoid the particle interpenetration and can easily lead to local fluid particle accumulation when stenosis exists. In the current work, the compressibility effect of DPD fluid model is addressed by introducing Morse potential into DPD force fields. This significantly reduces the compressibility effect while preserves other viscous fluid properties. The DPD-Morse fluid exhibits same fluid properties as the DPD fluid under counter-Poiseuille flow. It also presents smaller isothermal compressibility, larger speed of sound, and smaller Mach number, which indicate that the compressibility effect is less profound in the DPD-Morse fluid than the conventional DPD fluid.

The reduction of compressibility effect in DPD-Morse fluid is confirmed in simulations of a 67% stenotic microchannel flow where large fluid compression is produced. Driven by the same pressure gradient, discrepancy of flow field is observed between the two fluid models. The DPD-

Morse fluid exhibits more uniform fluid density distribution than the DPD fluid, attributed to the improved conservative force term that favorably preserves the fluid incompressibility.

Blood plasma is considered as incompressible Newtonian fluid with constant viscosity. However, when using particle dynamics approaches to model blood flow under severe stenosis, special care needs to be taken for the fluid viscosity. In DPD approach, the fluid viscosity is controlled by the friction factor of DPD force fields⁹³. A multi-viscosity system can be modeled with DPD by assigning a different friction factor for each fluid. Given the same friction factor, the fluid viscosity can be influenced by the fluid density⁷³. For the DPD fluid without compression, the density is fluctuated around a constant value. As density gradient appeared in the DPD fluid under severe stenosis, the difference between fluid viscosities at upstream and downstream becomes evident. This problem is mitigated by using the DPD-Morse fluid, where the change of fluid viscosities in the flow field is smaller and the fluid viscosities are closer to the blood plasma viscosity.

The comparison with CFD results indicate that compressibility effect existed in DPD model under severe stenosis dramatically affects the fluid dynamic properties including velocity and shear stress distribution. In contrast, the DPD-Morse fluid compared favorably with CFD results.

Fluid stress accumulation has been shown as an important indicator of shear-induced platelet activation, in which both fluid stress magnitude and exposure time play critical roles^{1,76,108}. Fluid stress gradient appeared in both types of fluid models, where the gradient is larger in the DPD fluid than in the DPD-Morse fluid. It is also found that the transport period is different where the platelet immersed in the DPD fluid transports at a faster rate than in the DPD-Morse fluid as a result of stronger compressible effect: the density gradient along flow direction accelerates the platelet

migration. Considering the difference of both fluid stress and exposure time, the DPD fluid model underestimates the fluid stress accumulation than the DPD-Morse fluid.

In the future work, the proposed DPD-Morse fluid model would be incorporated into a multiscale scheme where the rigid platelet model is replaced by our CGMD platelet model to investigate the mechanotransduction process of shear-induced platelet activation ¹¹⁷.

Platelet activation and aggregation are promoted when platelets pass through a stenosis or thrombus on the surface. DPD offers a promising computational description of platelet transport in a heterogeneous blood flow environment. However, the accuracy of DPD in describing stenotic fluid flow and associated platelet transport is deteriorated because of the significant compressible effect under large compression. Our DPD-Morse fluid model inherits the capability of DPD to simulate complex fluids at mesoscopic scale, and is superior to DPD model in describing viscous fluid phenomena through severe stenotic microchannel by better preserving the fluid incompressibility. Considering the complex geometries existed such as stenosis in the human vasculature and gap clearance of mechanical heart valves, our DPD-Morse model will offer a more accurate fluid stress accumulation along platelet flowing trajectory in such flow condition.

IV. Modeling blood plasma-platelet interaction using multiscale DPD-CGMD approach

4.1 Introduction

Platelet activation, aggregation and adhesion in blood plasma flow environment involve platelet-platelet, platelet-wall interactions that are strongly mediated by the hydrodynamic forces, the platelet shape and the existence of physical walls. Explicit platelet modeling is required to study these phenomena in wall-bounded shear flow. In prior studies, platelet is modeled as either rigid ellipsoid⁵³, or deformable capsule with connected particles that represent membrane^{81,85,101}. The simplified platelet model enables the study of single platelet dynamics in shear flow, which can be affected by its height from the vessel wall, its orientation along the vessel wall, and aspect ratio⁵³. A rigid platelet demonstrates periodic rotation following what is known as the Jeffery orbit flowing in the unbounded linear shear flow regime^{53,81}. As platelet approaches the wall, the lateral motion along the wall becomes dominant whereas the rotational motion is minimized⁵³. The platelet dynamics mediated by hydrodynamic factors and the physical walls have essential effects on platelet aggregation and adhesion^{51,52}. The multiple platelet interactions facilitate the modeling of platelet aggregation through the GPIIb α -vWF-GPIIb α bonds, where the GPIIb α was modeled on platelet surface, and vWF as a separate molecule with finite dimension^{51,52}. The platelet adhesion was modeled through the GPIIb α -vWF bond formation under shear flow^{54,85}.

The membrane-enclosed platelet models can predict platelet dynamic properties under shear flow, however, they are not able to simulate pseudopodia formation and shape change upon platelet activation. To enable the modeling of such phenomena, internal structures of platelet need to be included. Here, a multiscale CGMD platelet model is introduced that constitutes a bilayer elastic membrane, extensible actin filaments cytoskeleton, and viscous cytoplasm^{67,117}. The

construction of the model is based on molecular force fields, including non-bonded and bonded interactions. This model can not only be used to recreate platelet dynamics under shear flow as prior platelet models can do, but also to simulate shear-induced platelet activation with ensuing pseudopodia formation and shape change.

In the current work, the CGMD platelet model is coupled with the top-scale DPD-based blood plasma model through a hybrid potential composed of Lennard-Jones and DPD thermostat as a transition from molecular scale to fluid flow scale. The hybrid potentials have been applied extensively in simulations of solvent-polymer system, where the solvent is described by soft potentials, and the polymer beads interact with hard potentials⁸⁶. The DPD thermostat has also been used in MD simulations to conserve local momentum and correctly reproduce the hydrodynamic behavior^{3,60,83}. Here, the Lennard-Jones potential is employed to provide intermolecular interaction between fluid particles and membrane particles, and DPD thermostat maintains the local temperature, and provides no-slip boundary condition of fluid particles over platelet membrane.

The parameters of this hybrid potential are selected by fitting the platelet flipping dynamics under linear shear flow with the analytical solution of Jeffery's orbit. Furthermore, the fluid shear-induced membrane stress on platelet surface is depicted, in which the influence of membrane deformability is considered.

4.2 Methods

4.2.1 Fluid-platelet interaction model

The top scale DPD viscous blood plasma model is coupled with bottom scale CGMD platelet model through a hybrid potential. It is composed of Lennard-Jones potential that addresses the molecular interaction between fluid and membrane particles, and DPD thermostat that locally

maintains constant temperature and provides no-slip boundary condition of fluid particles over platelet membrane via the dissipative force term. The hybrid potential is expressed as:

$$d\mathbf{v}_i = \frac{1}{m_i} \sum_{j \neq i}^N (-\nabla U(r_{ij})dt + \mathbf{F}_i^D dt + \mathbf{F}_i^R \sqrt{dt}) \quad (\text{IV-1})$$

$$U(r_{ij}) = 4\epsilon_{LJ} \left[\left(\frac{\sigma_{LJ}}{r_{ij}} \right)^{12} - \left(\frac{\sigma_{LJ}}{r_{ij}} \right)^6 \right] \quad (\text{IV-2})$$

$$\mathbf{F}^D = -\gamma_{DPD} \omega^D(r_{ij}) (\mathbf{e}_{ij} \cdot \mathbf{v}_{ij}) \mathbf{e}_{ij} \quad (\text{IV-3})$$

$$\mathbf{F}^R = \sigma_{DPD} \omega^R(r_{ij}) \zeta_{ij} \sqrt{dt} \mathbf{e}_{ij} \quad (\text{IV-4})$$

where ϵ_{LJ} and σ_{LJ} are the depth of the potential well, and the zero-potential length of L-J potential.

γ_{DPD} and σ_{DPD} are the dissipative and random parameters of DPD thermostat.

4.2.2 Platelet flipping dynamics under shear flow

Under linear shear flow, the fluid particles exert external force and torque that governs platelet flipping motion. The rigid platelet is considered as a rigid body, and the total force and torque on the platelet are given by

$$\mathbf{F}_{ext}(t) = \sum_{i=1}^N \mathbf{F}_i(\mathbf{r}_i, t) \quad (\text{IV-5})$$

$$\mathbf{T}_{ext}(t) = \sum_{i=1}^N (\mathbf{r}_i - \mathbf{r}_{COM}) \times \mathbf{F}_i(\mathbf{r}_i, t) \quad (\text{IV-6})$$

where N is the total number of membrane particles in platelet, \mathbf{r}_i is position of particle i , $\mathbf{F}_i(\mathbf{r}_i, t)$ is the external force on particle i at time point t , \mathbf{r}_{COM} is the center of mass of platelet. It is noted that in the rigid body motion, forces between particles within the rigid body do not contribute to the external force and torque on the body. Therefore, $\mathbf{F}_i(\mathbf{r}_i, t)$ only comes from the fluid-structure interaction, and exerts from fluid particle to membrane particle.

To tune the parameters of the hybrid potential, the flipping motion of the platelet is investigated in which the platelet flipping dynamics is fitted to the analytical solution of Jeffery's orbit. The platelet flips under linear shear flow generated by two parallel plates moving along opposite directions. The no-slip boundary condition is applied on wall boundaries and fluid velocity is zero at the wall. Periodic boundary condition is imposed along x- and z-dimensions. The Reynolds number of fluid system is 2.59 (based on characteristic length of $16 \mu m$, mean velocity of 15 cm/s). The dimension of the parallel plate flow chamber is $L = 16 \mu m$, $H = 16 \mu m$, and maximum velocity $v_{max} = 30 \text{ cm/s}$ (Figure IV-1).

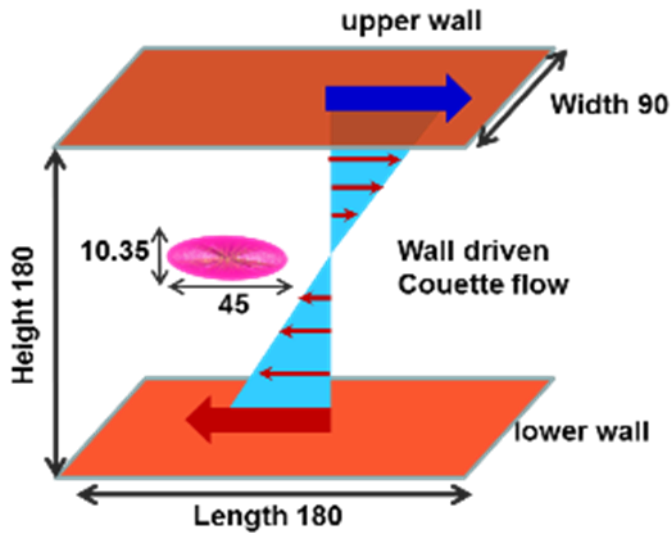


Figure IV-1. Simulation setup to study platelet flipping dynamics under linear shear flow. Parallel flow chamber is constructed with upper and lower walls moving in opposite directions. The platelet is positioned at the center.

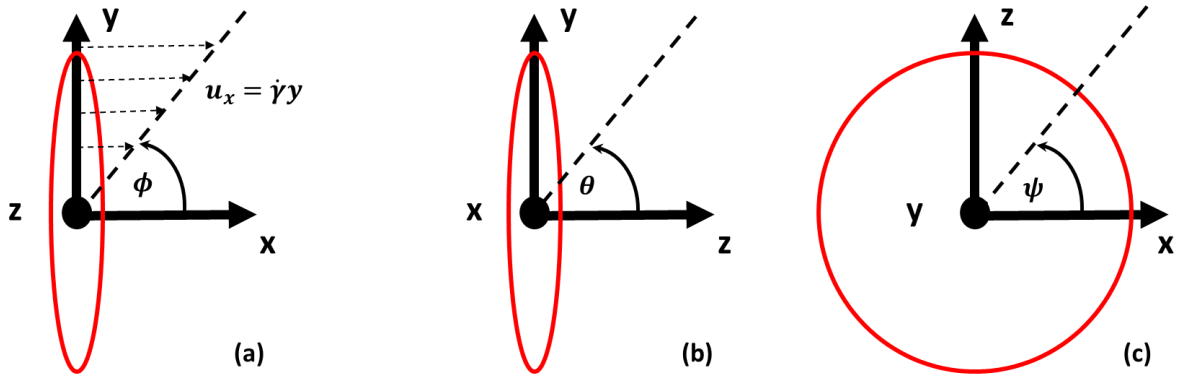


Figure IV-2. Platelet rotation: (a) along z axis, where ϕ is the deviated angle with respect to x axis; (b) along x axis, where θ is the deviated angle with respect to z axis; (c) along y axis, where ψ is the deviated angle with respect to x axis. Shear flow is applied in x-y plane along x direction.

In the current work, we focus on the rotation of platelet in shear plane x-y with rotation angle ϕ . Rotation within x-z plane with angle ψ is not considered. Rotation angle θ is fixed with two values, $\theta = 0$ and $\theta = \frac{\pi}{2}$ (Figure IV-3).

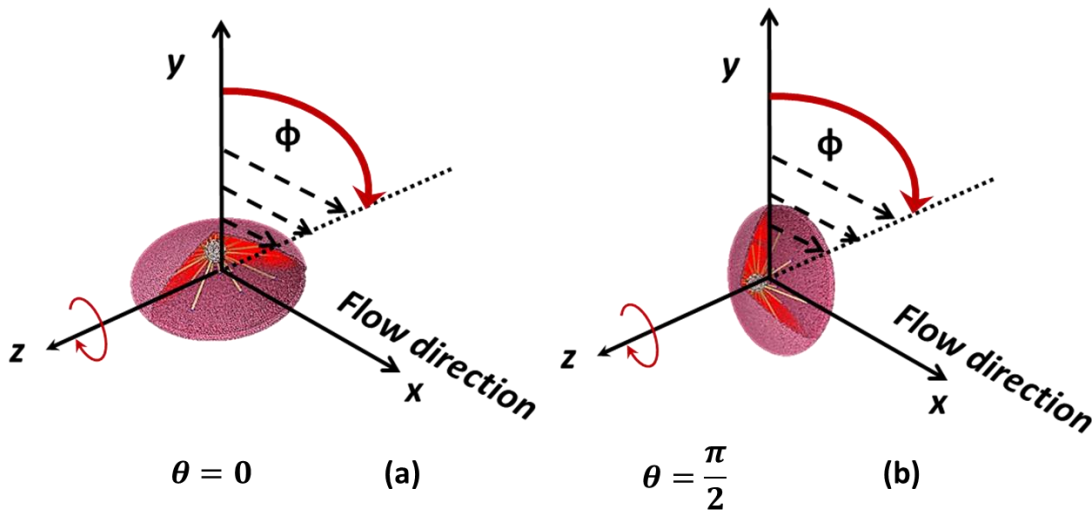


Figure IV-3. Platelet flipping in x-y plane with (a) $\theta = 0$ and (b) $\theta = \frac{\pi}{2}$. Rotation angle ϕ is monitored as a function of time.

The platelet flipping angle ϕ and period T are defined by ^{31,57,110}

$$\phi = \text{atan}\left(\frac{1}{r_e} \tan\left[-\frac{\dot{\gamma} t r_e}{r_e^2 + 1} + \tan^{-1}(r_e \tan \phi_0)\right]\right) \quad (\text{IV-7})$$

$$T = \frac{2\pi}{\dot{\gamma}} \left(r_e + \frac{1}{r_e}\right) \quad (\text{IV-8})$$

where ϕ is defined as the angle of the platelet with respect to the flow direction, ϕ_0 is the initial value of ϕ , $\dot{\gamma}$ is the shear rate, r_e is the aspect ratio of the platelet ($r_e > 1$).

The parameters of hybrid potential dictate the platelet flipping dynamics. Four parameters, including ϵ_{LJ} and σ_{LJ} of L-J potential, γ_{DPD} and σ_{DPD} of DPD thermostat, are involved and demonstrate different sensitivity to affect platelet flipping angle ϕ .

4.2.3 Platelet surface stress analysis

Two scenarios are considered: first, the whole platelet is kept rigid after immersion in fluid domain; second, the platelet membrane is considered deformable, and cytoplasm can move freely, whereas the cytoskeleton is kept rigid (Figure IV-4). The rigid platelet model maintains the ideal ellipsoidal shape of platelet. The deformable model deforms in accordance with the interactions between the deformable platelet and the surrounding fluid flow.

The mechanical stress in the multiscale system is expressed in terms of per-atom stress, which is represented as a stress tensor $S_{ab} = [\tau_{ab}]_{3 \times 3}$, where a and b take values x, y, and z to generate the six components of the symmetric tensor. in MD simulations, the per-atom stress is computed as:

$$S_{ab} = -[m v_a v_b + \frac{1}{2} \sum_{n=1}^{N_p} (r_{1a} F_{1b} + r_{2a} F_{2b}) + \frac{1}{2} \sum_{n=1}^{N_b} (r_{1a} F_{1b} + r_{2a} F_{2b})] \quad (\text{IV-9})$$

where v is velocity component for particle i and j and r_1 and r_2 and F_1 and F_2 are positions and forces of the two interacting particles. N_p is the number of neighboring particles that interact with particle i via pairwise potential, and N_b is the number of particles that particle i interact with via bonded potential. The first term of equation (IV-9) is the kinetic part, and the last two terms are the potential part. There is no angle, dihedral and improper force terms in the membrane. S_{ab} is in stress-volume unit. To have the unit of stress, S_{ab} needs to be divided by a per-atom volume, which is computed as $1/n$, where n is the number density of fluid or membrane.

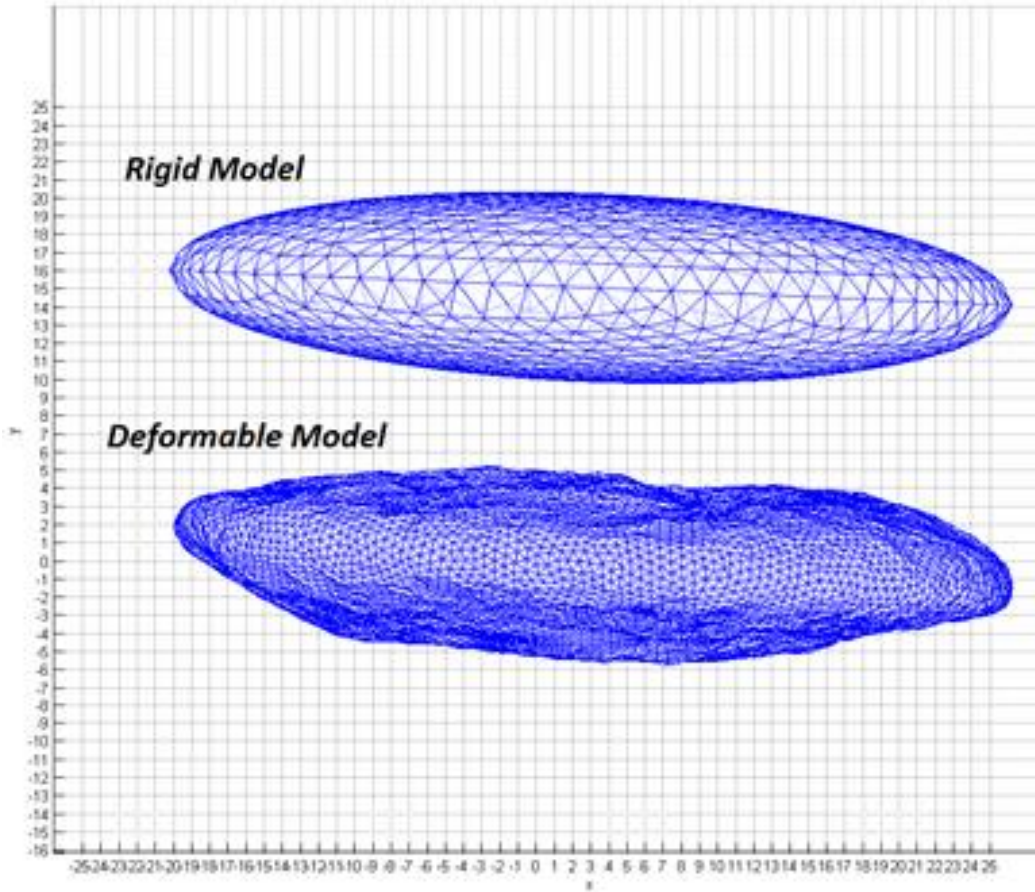


Figure IV-4. Mesh network of rigid and deformable platelet membrane.

4.2.4 Physical unit conversion

The model dimensionless units are converted into physical units. The superscript * denotes a quantity in the model dimensionless units. The subscript r represents a reference unit used in the scaling scheme.

First, the reference length scale σ_r is determined by the real platelet diameter $D_p = 4 \mu\text{m}$ and the model platelet diameter $D_p^* = 45$, according to the following definition:

$$\sigma_r = \frac{D_p}{D_p^*} \text{m} \quad (\text{IV-10})$$

where m stands for meter. Based on σ_r , the characteristic length of the flow domain $D_f^* = 180$ in the model is converted to $D_f = 16 \mu\text{m}$ in the physical unit.

Second, the reference mass scale m_r is defined as

$$m_r = \frac{\rho_f \sigma_r^3}{\rho_f^*} \text{kg} \quad (\text{IV-11})$$

where the mass density of blood plasma is $\rho_f = 1060 \text{ kg m}^{-3}$ at $37 \text{ }^\circ\text{C}$, and the particle density of the DPD fluid $\rho_f^* = 3$ in the model. kg stands for kilogram.

Third, the reference time scale t_r is defined as the time to move one reference length σ_r with one reference velocity v_r . The reference velocity v_r is determined by

$$v_r = \frac{v_f}{v_f^*} \quad (\text{IV-12})$$

where $v_f^* = 4$ is wall velocity in the model, and corresponds to velocity $v_f = 30 \text{ cm s}^{-1}$ in physical units. t_r is then computed by

$$t_r = \frac{\sigma}{v_r} \text{s} \quad (\text{IV-13})$$

where s stands for second. The mean velocity in the model Couette flow is $v_u^* = 2$ and thus the mean velocity in the SI unit v_u^* is computed by

$$v_u = v_u^* v_r \quad (\text{IV-14})$$

Based on the reference length, mass and time scales, the following dimensionless and physical units are introduced. The reference energy scale ε_r is

$$\varepsilon_r = m_r v_r^2 \quad (\text{IV-15})$$

The shear rate $\dot{\gamma}^*$, shear stress τ^* and viscosity μ^* of the fluid in the model formulation have:

$$\dot{\gamma}^* = \frac{2v_f^*}{D_f^*} \quad (\text{IV-16})$$

$$\tau^* = \dot{\gamma}^* \mu^* \quad (\text{IV-17})$$

The shear rate $\dot{\gamma}$, shear stress τ and dynamic viscosity μ of the fluid in the physical units are:

$$\dot{\gamma} = \frac{2v_f}{D_f} \quad (\text{IV-18})$$

$$\tau = \tau^* \frac{\varepsilon_r}{\sigma_r^3} \quad (\text{IV-19})$$

$$\mu = \frac{\tau}{\dot{\gamma}} \quad (\text{IV-20})$$

Reynolds number Re is computed by:

$$Re = \frac{\rho_f v_u D_f}{\mu_f} \quad (\text{IV-21})$$

where v_u is the mean velocity of the fluid, D_f is the diameter of the simulated flow region and μ_f is the dynamic viscosity of the flow.

Table 3. Reference units used in the DPD simulations; model parameters and translation of various input and output data from the dimensionless to real units

Quantity	Symbols	Model values	SI values
Length	σ_r	1	88.89 nm
Mass	m_r	1	2.48×10^{-19} kg
Time	t_r	1	1.19 μ s
Energy	ε_r	1	1.40×10^{-21} kg m ² s ⁻²
Velocity	v_r	1	7.5 cm s ⁻¹
Force	$f_r = m_r \cdot v_r / t_t = \varepsilon_r / \sigma_r$	1	1.57×10^{-2} pN
Diameter of microvessel	$D_f = \sigma_r D_f^*$	180	16 μ m
Diameter of the platelet	$D_p = \sigma_r D_p^*$	45	4 μ m
Thickness of the platelet		11.25	1 μ m
Aspect ratio of platelet	r_e	0.25	0.25
Mean velocity of the fluid	$v_u = v_u^* v_r$	2	15 cm s ⁻¹
Shear rate	$\dot{\gamma} = \dot{\gamma}^* \frac{v_r}{\sigma_r}$	0.044	37500 s ⁻¹
Shear stress	$\tau = \tau^* \frac{\varepsilon_r}{\sigma_r^3}$	18.56	369 dyne cm ⁻²
Viscosity *	$\mu = \mu^* \frac{\varepsilon_r}{v_r \sigma^2}$	417.54	0.98 mPa s
Reynolds number **	$Re = \frac{\rho_f^* v_u^* D_f^*}{\mu_f^*} = \frac{\rho_f v_u D_f}{\mu_f}$		2.59

Notes: * the normal value of plasma is 1.10-1.30 mPa s at 37 °C³⁴.

** Typical Reynolds number range of blood flow in the body varies from 1 in small arterioles to approximately 4000 in the largest artery, the aorta. ³⁶.

4.3 Results

4.3.1 Viscous blood plasma modeling

The DPD dissipative parameter γ and cutoff distance r_c are adjusted to achieve the blood plasma viscosity of 1.1 mPa·s. The counter-Pouille flow method is employed for the measurement of viscosity. First, r_c is fixed as 1.0, γ is adjusted in the range between 4.5 and 135. The viscosity is increased linearly with γ until $\gamma = 90$. When γ is increased to 112.5, an unlinear increase is observed, and when γ is further increased to 135, DPD fluid becomes unstable where the parabolic

velocity profile is lost. γ is finally chosen as 90. Given $\gamma = 90$, r_c is adjusted ranging from 0.6 to 2. When $r_c = 1.8$, the blood plasma viscosity is 0.98 mPa·s which is very close to the target value of 1.1 mPa·s.

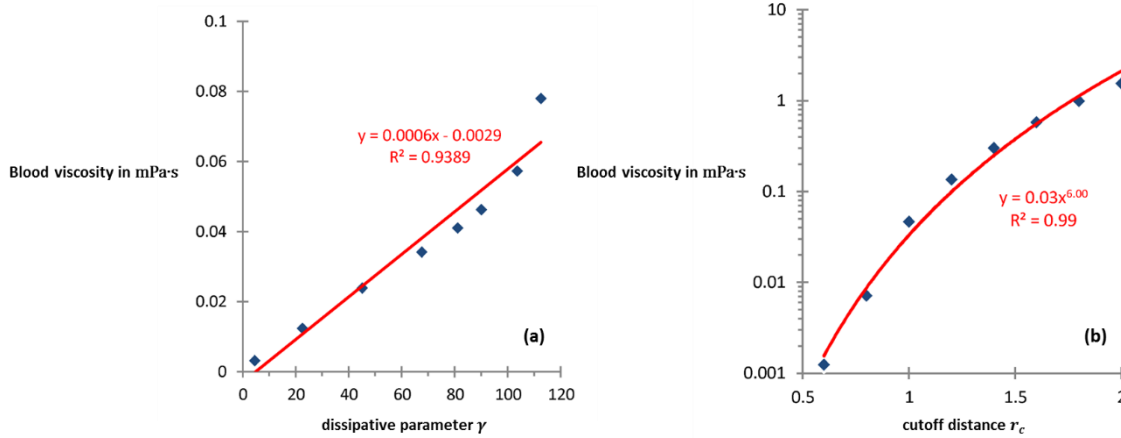


Figure IV-5. Blood plasma viscosity as a function of dissipative parameter γ and cutoff distance r_c , measured with counter-Poiseuille flow method. (a) viscosity versus γ when $r_c = 1.0$; (b) viscosity versus r_c when $\gamma = 90$.

4.3.2 Platelet flipping dynamics

The platelet flipping angle ϕ is determined by four parameters of the hybrid potential. Figure IV-6 shows the function $\phi(\dot{\gamma}t)$ in half flipping period, where the x axis represents the dimensionless time $\dot{\gamma}t$, and y axis represents the flipping angle ϕ . First, the impact of σ_{LJ} is studied while other three parameters are kept constant as $\varepsilon_{LJ} = 0.3$, $\gamma_{DPD} = 90$, $r_c = 1.8$. It is observed that when $\sigma_{LJ} > 1.0$, the platelet does not flip in linear shear flow. Reducing σ results in a smaller difference between the simulation result and the analytical solution. On the other hand, if σ_{LJ} is smaller than 0.4, the blood plasma particles penetrate into the platelet interior. $\sigma = 0.6$ is therefore selected as the final parameter. Next, the influence of ε_{LJ} is studied. It is observed that when ε_{LJ} is increased to 6, the simulation result gets closer to the analytical solution. Further increase of ε_{LJ}

gives the similar results. In addition, the dissipative parameter γ_{DPD} and cutoff distance r_c have no impact on the flipping angle ϕ . Comparing ϕ from flipping simulation using rigid platelet and the analytical solution of Jeffery's orbit indicates that the equilibrium distance σ_{LJ} and the well depth ε_{LJ} are key parameters to determine the platelet flipping dynamics, while the parameters of DPD thermostat have little impact on it. The final parameter set is defined as $\sigma_{LJ} = 0.6$, $\varepsilon_{LJ} = 6$, $\gamma_{DPD} = 90$, and $r_c = 1.6$.

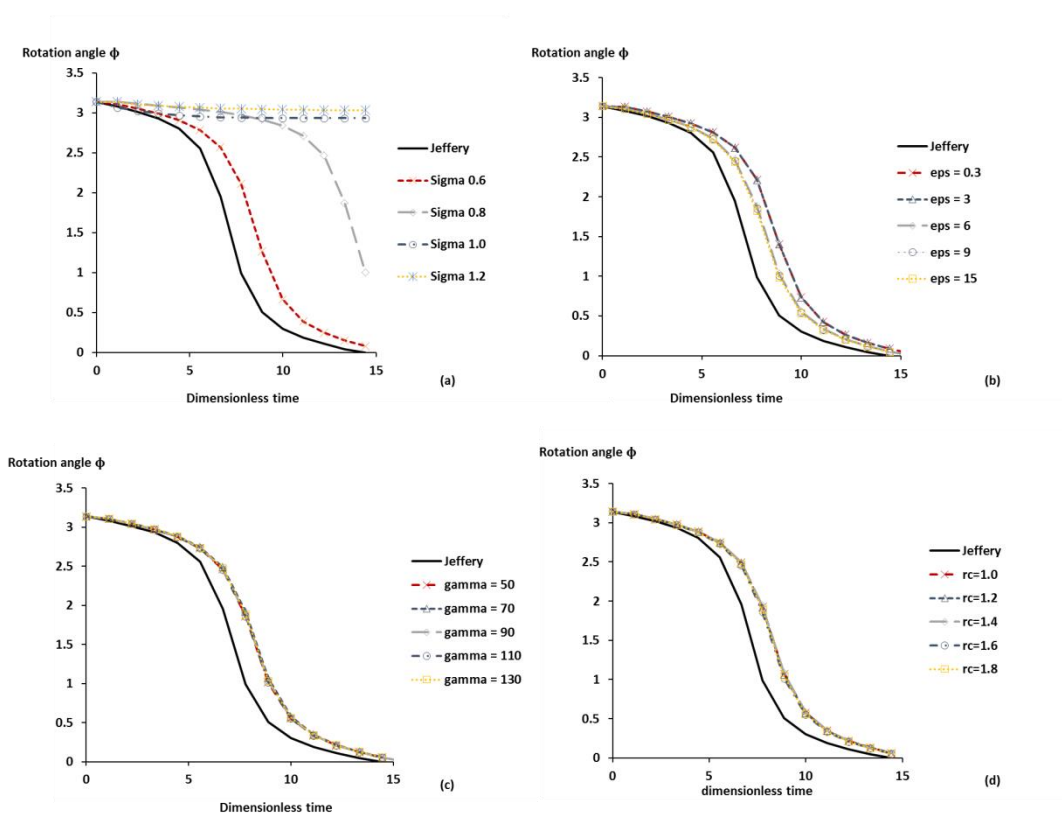


Figure IV-6. Flipping angle ϕ as a function of dimensionless time $\dot{\gamma}t$ in half flipping period. (a) effect of σ_{LJ} on ϕ . When $\sigma_{LJ} > 1.0$, platelet does not flip under shear flow; when $\sigma_{LJ} < 0.4$, fluid particles penetrate into platelet through membrane. σ_{LJ} is selected finally to be 0.6. (b) effect of ε_{LJ} on ϕ . An increase of ε_{LJ} leads to a closer match to analytical solution. The closest match is achieved when $\varepsilon_{LJ} = 6$. (c) effect of γ_{DPD} on ϕ . (d) effect of r_c on ϕ . γ_{DPD} and r_c do not have impact of platelet flipping.

4.3.3 Effects of platelet deformability on platelet flipping dynamics

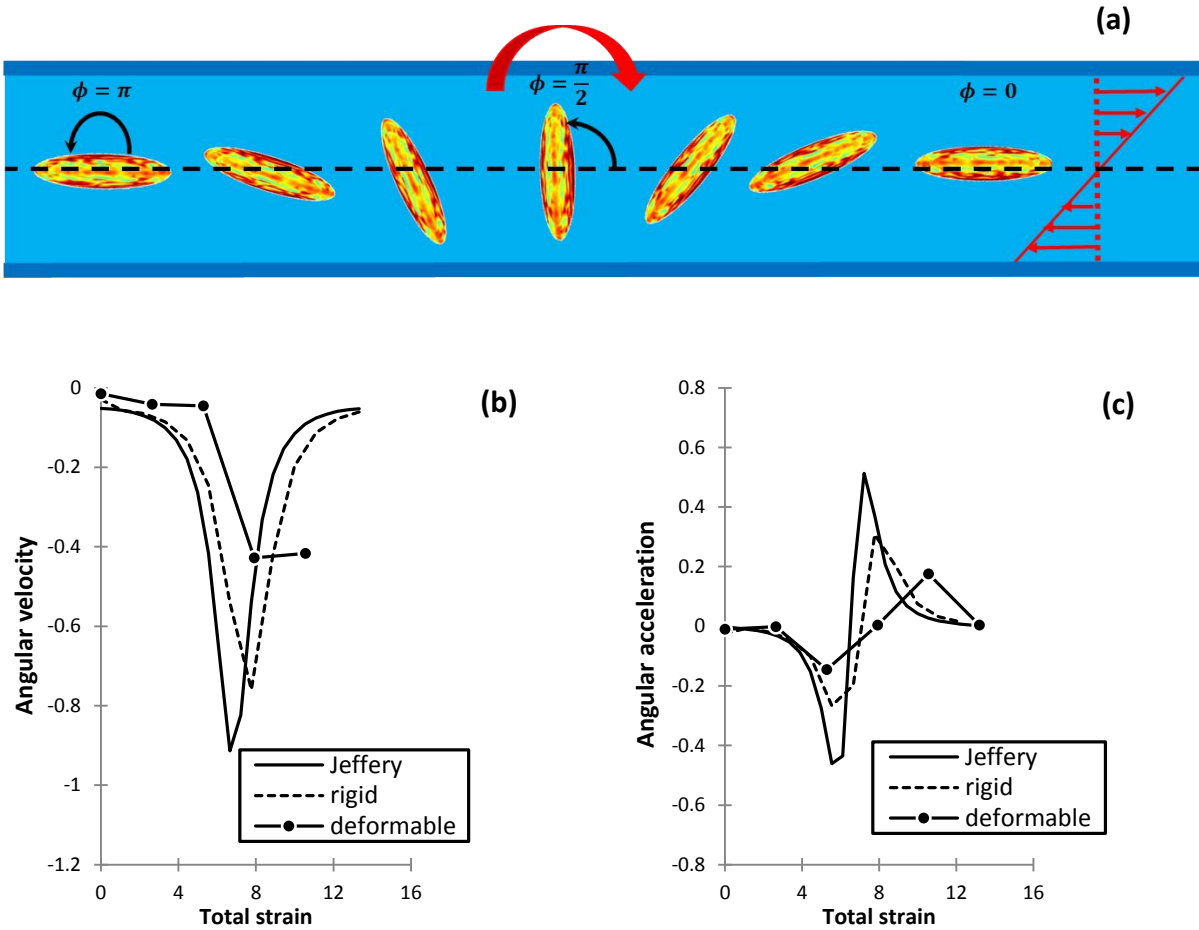


Figure IV-7. (a) Platelet flipping in linear shear flow. (b) Angular velocity $\dot{\phi}(\dot{\gamma}t)$ vs. the strain $\dot{\gamma}t$ for Jeffery’s orbits and numerical solutions using the rigid and deformable platelet models. (c) Angular acceleration $\ddot{\phi}(\dot{\gamma}t)$ vs. the strain $\dot{\gamma}t$ for Jeffery’s orbits and numerical solutions using the rigid and deformable platelet models.

The angular velocity and acceleration of half flipping period are depicted in Figure IV-7. The platelet was initially orientated $\phi = \pi$ with respect to the x positive direction. Under shear flow with shear rate 37500 s^{-1} , the orientation ϕ is gradually reduced to 0. Figure IV-7 (a) is a schematic diagram of platelet flipping from $\phi = \pi$ to $\phi = 0$. The plots (b) and (c) are represented as the first and second derivatives of platelet flipping angle ϕ . It is shown that the profiles of rigid platelet is closer to the analytical solution. Increasing the deformability of platelet results in a slower flipping motion with smaller angular velocity and acceleration.

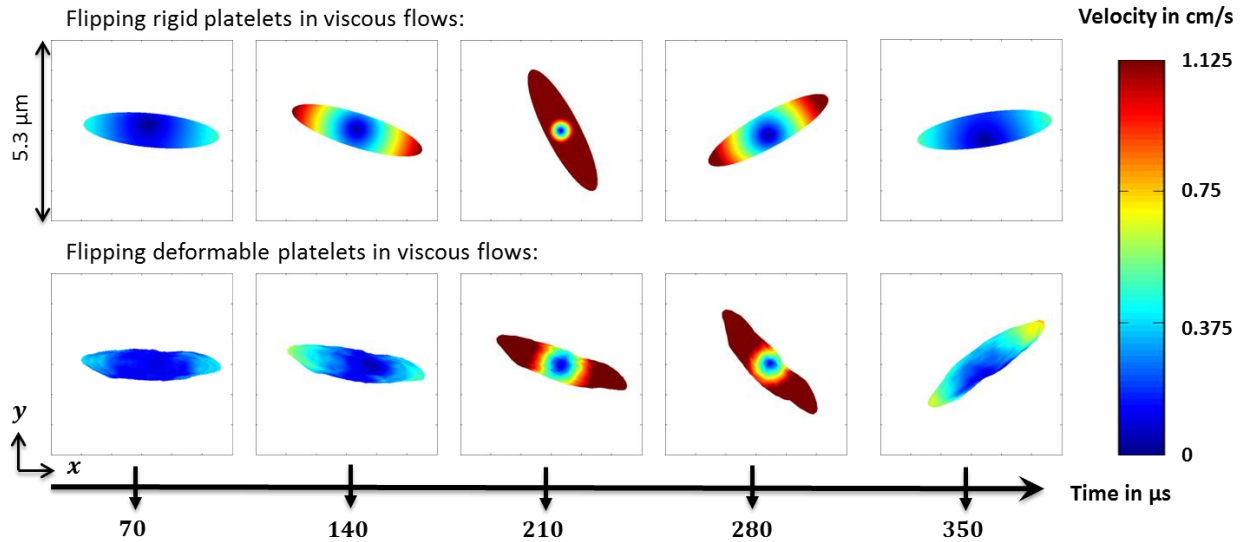
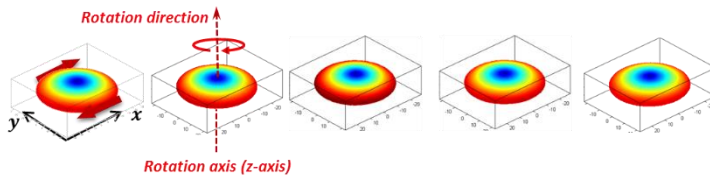


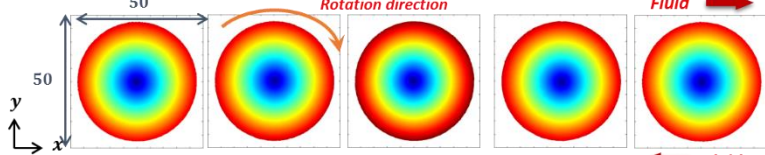
Figure IV-8. Platelet surface velocity profile during flipping. Top row: rigid platelet model. Bottom row: deformable platelet model. The velocity profiles at five discrete time points are illustrated, $70 \mu s$, $140 \mu s$, $210 \mu s$, $280 \mu s$ and $350 \mu s$. The maximum velocity on platelet surface for both cases is approximately 1.125 cm/s . Rigid platelet flips faster than deformable platelet. Bending of membrane is observed in deformable platelet model.

The platelet membrane velocity magnitude is depicted in Figure IV-8, in which the first row represents data from rigid platelet, and second row is from deformable platelet. The velocity magnitude is computed based on v_x , v_y , v_z of platelet membrane particles after spatial and temporal averaging. The rigid platelet flips faster than the deformable platelet, which is consistent with the results from Figure IV-7. For both rigid and deformable platelets, the highest velocity is found along the edge, and smallest velocity in the center.

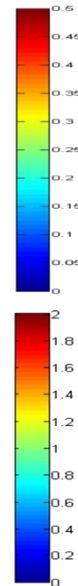
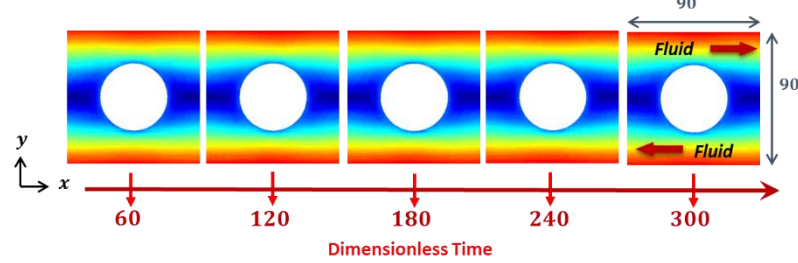
(i) Velocity magnitudes of the platelet surface particles (3D-viewpoint):



(ii) Velocity magnitudes of the platelet surface particles (xy-viewpoint):

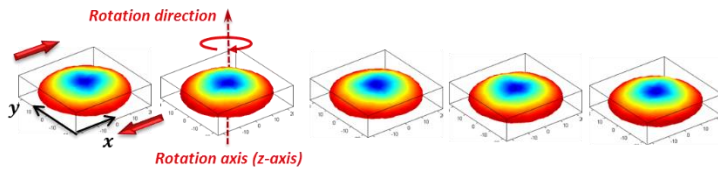


(iii) Velocity magnitudes of the surrounding fluidic particles:

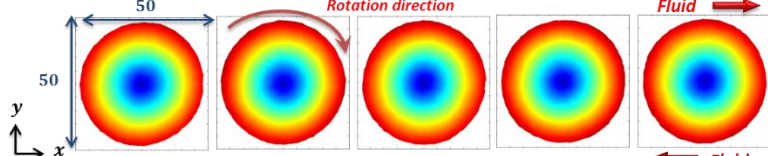


(a)

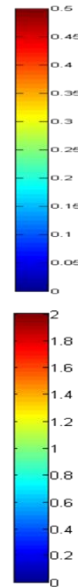
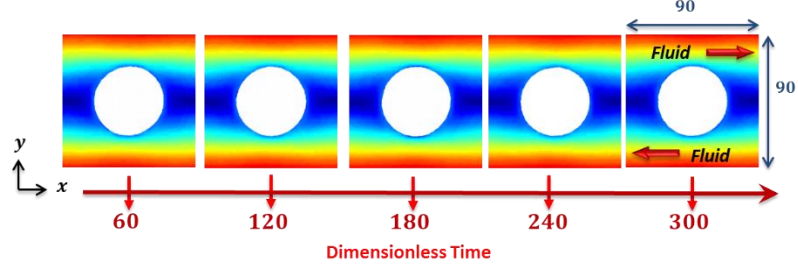
(i) Velocity magnitudes of the platelet surface particles (3D-viewpoint):



(ii) Velocity magnitudes of the platelet surface particles (xy-viewpoint):



(iii) Velocity magnitudes of the surrounding fluidic particles:



(b)

Figure IV-9. Platelet surface velocity distribution at $\theta = \frac{\pi}{2}$. (a) Rigid platelet. (b) Deformable platelet.

The platelet flipping was also performed when $\theta = \frac{\pi}{2}$. The surface velocity magnitude was plotted in Figure IV-9. Similar surface velocity patterns and magnitudes are observed in between rigid and deformable platelets at $\theta = \frac{\pi}{2}$.

4.3.4 Effects of platelet deformability on platelet membrane surface stress distribution ($\theta = 0$)

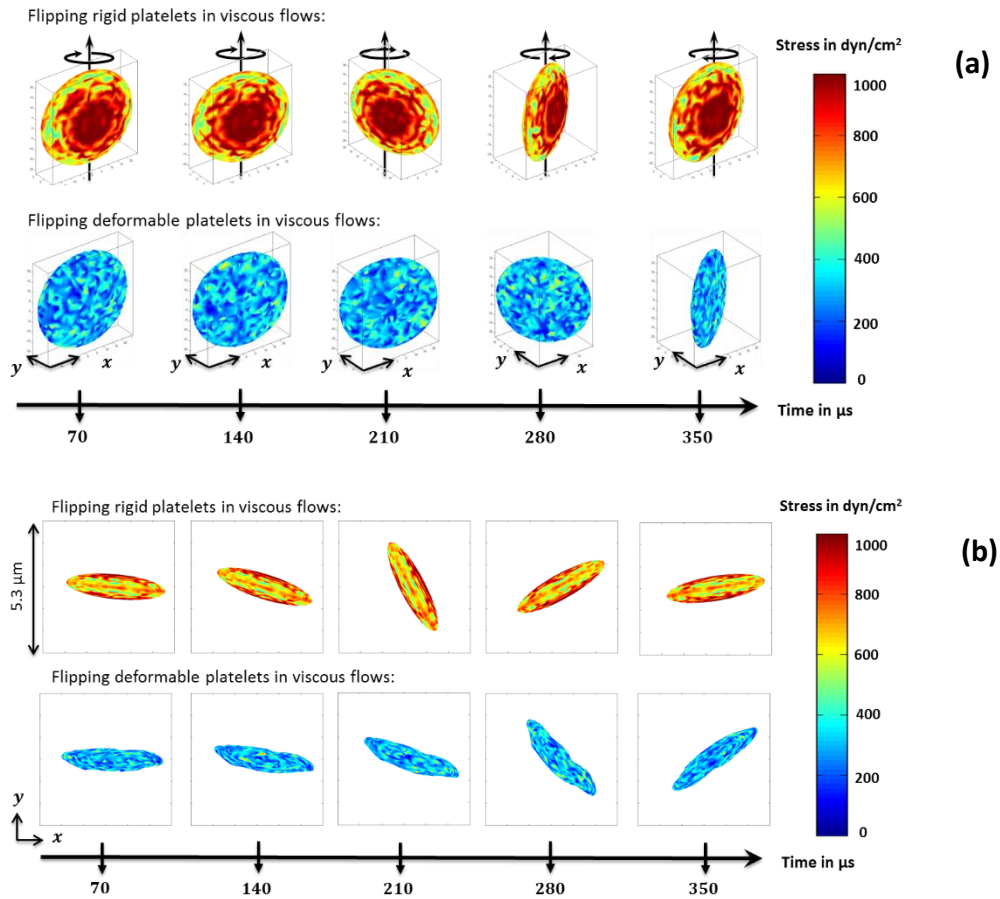


Figure IV-10. Platelet surface stress distribution. (a) 3D perspective. (b) 2D perspective. In both (a) and (b), top row: rigid platelet model, bottom row: deformable platelet model. Higher stress is observed in membrane of rigid platelet model, with maximum value approximately 1000 dyne/cm^2 .

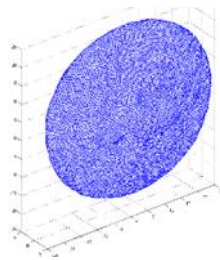
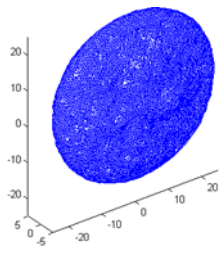
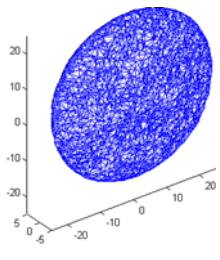
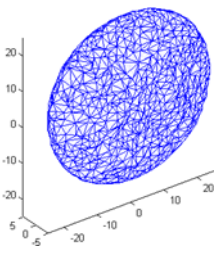
The fluid induced platelet membrane stress is studied. Figure IV-10 shows the 3D perspective and 2D perspective. For rigid platelet, the membrane stress in the center is higher than

the stress on the edge, while the membrane stress is relatively uniform in deformable platelet. The rigid platelet has a membrane stress around 2.6 times higher than the deformable platelet.

4.3.5 Spatial-temporal averaging

The instantaneous properties of platelet can be acquired at every time step. However, on this length and time scales, the desired information cannot be extracted. Therefore, a spatial and temporal averaging is conducted to depict the platelet properties at larger length and time scales. First, the platelet is coarse grained to 3 different length scales from original 19,675 particles by reducing the number of mesh elements on the surface. A cutoff distance is set up for each vertex such as the particles fall into this cutoff volume is being averaged. Meanwhile, the temporal averaging is achieved by averaging same particle information over a certain number of timesteps.

Table 4. Platelet spatial coarse-graining level.

	Original	Coarse Grained		
				
Total of points	19,675 particles	9,800 points	4,800 points	1,350 points
Ratio of points over original particles	100 %	49.8 %	24.4 %	6.86 %

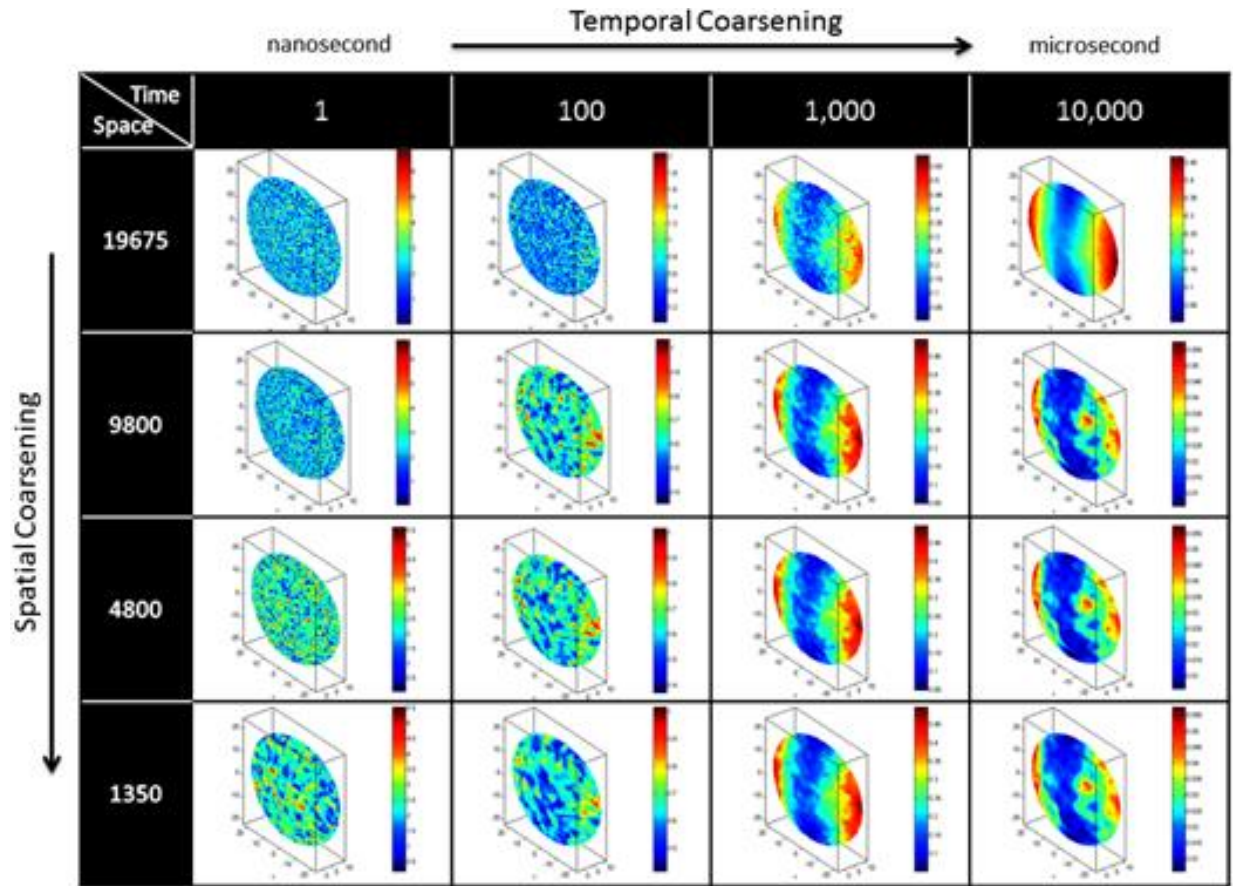


Figure IV-11. Coarse-graining effect along spatial and temporal scales. Rows represent spatial coarse-graining, where the first row is the velocity profile based the original membrane construction, and second to fourth row are averaged velocity profile on a coarse-grained platelet membrane. Columns represent temporal coarse-graining, where the first column is the description on 1 ns, and the last column presents velocity profile on 10 μ s.

It is shown that the two edges of platelet have highest velocity at ms time scale, which is not observable on a ns time scale. Along the length dimension at ms time scale, the general trend of membrane surface velocity distribution still exists although not as clear as the original platelet model.

4.4 Discussion and conclusions

In the current work, a multiscale platelet mechanotransduction model is built in which the mesoscopic DPD fluid model is coupled to the microscopic CGMD platelet model. It is able to recreate the accurate platelet flipping dynamics under shear flow, and at the same time, provide accurate mapping of fluid flow-induced platelet membrane surface stress distribution.

The coupling scheme adopts functional form of a hybrid potential including Lennard-Jones potential and DPD thermostat. The Lennard-Jones potential represents molecular scale interaction between the fluid flow and platelet membrane. The DPD thermostat locally preserves the temperature and conserves the momentum. In rigid platelet simulation, the whole platelet is considered as one rigid body, which movement is governed by the external force and torque applied from fluid domain. The hybrid potential plays an important role as it determines the fluid-structure interaction force and the ensuing platelet motion in shear flow.

The parameterization process successfully generates the rigid platelet flipping dynamics described theoretically by Jeffery's orbit. The parameterization of hybrid potential intends to match the simulation results to the analytical solution given by Jeffery's orbit. σ_{LJ} controls the repulsive force strength in between plasma and membrane particles. When $\sigma_{LJ} > 1.0$, a strong repulsive force leads to a gap between fluid and platelet membrane, and fluid cannot exert sufficient friction force on platelet to enforce the flipping motion; when $\sigma_{LJ} \leq 0.4$, the fluid particles are too close to the platelet domain and penetration takes place. $\sigma_{LJ} = 0.6$ is finally selected under which no penetration is observed in the simulation. It is noted that with the final selection of hybrid potential parameters, the platelet flipping angle function does not match exactly with Jeffery's orbit. This is because the presence of wall slows down the flipping motion. Mody et al.⁵³ suggest that only when platelet centroid is far from the wall, the simulation result can

match exactly with Jeffery's orbit, i.e., the ratio $H/a > 20$, where H is the height of the platelet centroid from the wall, and a is the major radius of platelet. In our simulation, $H/a = 4.0$, and therefore, the wall still has some effect on platelet flipping motion.

It is noted that in Mody et al.⁵³ and Sweet et al.⁸⁵ the shear rate of fluid flow is 1000 s^{-1} and 6.7 s^{-1} , while in our simulations the shear rate is 37500 s^{-1} . This results in a different flipping period T in which the platelet flips fastest in our simulations and slowest in Sweet et al.⁸⁵. When the dimensionless time $\dot{\gamma}t$ is considered, the period $\dot{\gamma}T = 2\pi \left(r_e + \frac{1}{r_e} \right)$, which is independent of the real flipping time. This facilitates the comparison of platelet flipping dynamics with Jeffery's orbit. Taking account the deformability of platelet membrane, the angular velocity and acceleration during platelet flipping are reduced. Though this deviates from the analytical solution of Jeffery's orbit, it is a closer description of platelet flipping dynamics to the experiments where the platelet is deformable.

The prediction of shear-induced platelet activation requires an accurate mapping of membrane stress induced by surrounding fluid flow, which can only be achieved in our multiscale model. The fluid particles exert normal and shear stresses on membrane particles. The rigid platelet demonstrated a surface stress distribution that is 2.6 times greater than the deformable platelet. As the rigid body does not yield and resists the fluid flow, a higher surface stress distribution is expected⁷². Considering the fact that platelets in blood flow are deformable bodies, the rigid platelet model actually overestimates the platelet surface stress distribution and their activation potential. The surface stress and velocity of membrane particles are further averaged along spatial and temporal dimensions, which smooth out the atomistic fluctuations and lead to a clearer trend at micrometer and microsecond scales.

A multiscale blood plasma-platelet interaction model is developed by coupling mesoscopic DPD fluid flow and CGMD platelet. The accurate platelet flipping dynamics under linear shear flow is achieved using a rigid model which is comparable to the analytical solution of Jeffery's orbit. By fitting the platelet angular change to the Jeffery's orbit, the unknown parameters of the interfacial potential function are determined. Furthermore, the platelet deformability is considered as a factor to influence platelet flipping dynamics. The surface stress distribution is depicted and compared in between rigid and deformable platelets, which shows that a rigid platelet would overestimate the surface stress distribution and lead to an erroneous prediction of platelet activation potential in terms of surface stress accumulation.

V. Multiscale model of shear-induced platelet activation

5.1 Introduction

Hemodynamic forces can be an agonist to platelet activation. Macroscopically, fluid shear induced platelet activation is majorly depicted by investigating the effects of fluid shear stress and exposure time on thrombin generation and expression of platelet surface thrombogenic markers^{75,77,106-108}. Such studies are conducted experimentally by applying physiological and pathological shear stress waveforms to platelets. Constant or dynamic shear stress waveforms are applied to platelets through perfusion chambers such as cone and plate shearing device to mimic the in vivo flow conditions. These studies are able to predict platelet activation potential based on thrombogenic marker expression after exposure to various fluid shear stresses for different time periods. Furthermore, morphological changes of platelet activation can be described by SEM images after platelet is exposed to shear. However, this kind of studies is not able to provide dynamic information of the process of platelet activation.

Platelet activation is characterized by two major processes, one is the secretion of small molecules and proteins, the other is the cytoskeleton-mediated shape change²⁰. The platelet shape change involves cytoskeleton rearrangement, in which actin filament bundles elongate and protrude from the platelet membrane to form pseudopodia¹¹⁴. The number and size of pseudopodia can be varied and they play a major role in regulating platelet aggregation efficiency²⁷. As platelets being activated in suspension, the actin matrix decreases in size and eventually reaches a stable condition²⁰. The actin filaments in pseudopodia form parallel tight bundles⁸⁴. The actin assembly in pseudopodia is suggested as a result of elongation, not branched nucleation as in lamellipodia^{41,84}. A treadmilling model was proposed to explain the actin polymerization and pseudopodia formation, in which the barbed end adds actin monomers and the pointed end removes monomers

^{39,84}. Both polymerization on the barbed end and depolymerization on the pointed end determine the protrusive force of actin filament bundles against membrane. Whenever the pseudopodia reach the effective length, its growth can be terminated by capping protein.

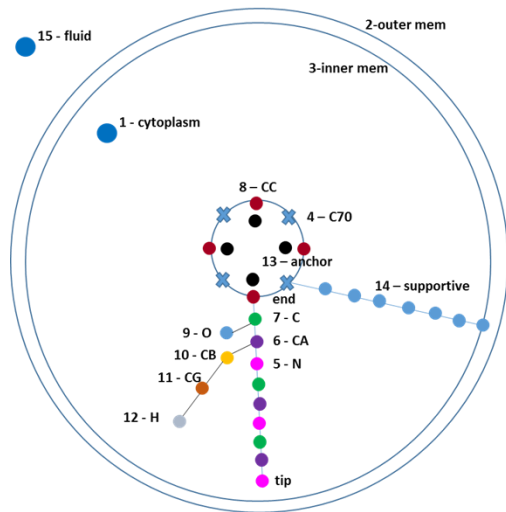
The computational approaches such as molecular dynamics offer us a promising tool to explore this phenomena in-silico. A multiscale platelet model in fluid shear has been developed in Chapter IV, which is able to accurately generate platelet transport dynamics such as flipping, as well as the surface stress mapping over platelet membrane. The most significant novelty of this model is that it explicitly model the internal structures of platelet, which is composed of cytoskeleton and cytoplasm. The cytoskeleton here is a simplified model that mimics the actin network of platelet. It is composed of 44 protrusible filaments ranging from 100 to 800 nm supported by a cytoskeleton core in the center ¹¹³. Each filament is considered as a helical polypeptide chain. When the platelet is in its static state, the filaments maintain their helical structure. As soon as platelet is activated under shear, the filament transits from a helical to a fully extended conformation to provide extra length for modeling pseudopodia formation. The number and dimension of protruded pseudopodia is then compared to the experimental results generated from the HSD and electron microscopy ⁶⁷.

5.2 Methods

5.2.1 Multiscale platelet mechanotransduction model

A molecular model of platelet is constructed with CGMD approach ^{67,113,117}. It constitutes a bilayer elastic membrane, extensible actin filaments cytoskeleton, and a viscous cytoplasm (Figure V-1). The membrane (thickness of 300 Å) is designed for representing both the phospholipid bilayer (100 Å) and the exterior coat (150 ~ 200 Å). It is characterized by a two layer membrane constructed separately by 2D triangular mesh and integrated by connecting adjacent

vertices in close proximity. Particles are located at the nodes of the network. The design of two-layer membrane makes it possible to add many receptors on the outer layer of the membrane, which could stretch the current platelet model capability to incorporate adhesion and aggregation dynamics. The actin filament network is modeled by the rigid filamentous core together with radiating filament bundles. To feature the geometric consistency, the carbon 70 (C70) structure is used to resemble the oval shaped core as observed in the electron micrograph ²⁶. The filament bundles are modeled by the α -helical structure, which is adopted for mimicking the spring-loaded molecular machineries because its spiral conformation could be stretched almost fully with a continuous increase in the stretching force ²⁹. The cytoplasm is modeled by a collection of homogeneous particles which interact with each other via Morse potential to recreate cytoplasm viscosity of 4.1 mPa ¹¹⁵.



atom type	function
1	cytoplasm
2	outer membrane
3	inner membrane
4	C70 (minus 44 atoms)
5	N
6	CA CT1
7	C
8	CC
9	O+OC
10	CB CT1
11	CG1 CT3 + CG2 CT3
12	H
13	anchor
14	supportive particle
15	fluid

Figure V-1. Atom types of platelet. The platelet is viewed from above its top surface. Type 1 is the cytoplasm, type 2 and 3 are membrane, type 4 to 14 are cytoskeleton, and type 15 are fluids. In cytoskeleton construction, only backbone particles play a role in pseudopodia formation.

5.2.2 Cytoskeleton stress accumulation

The platelet resides in a linear shear flow environment with 85.76 dyne/cm^2 with blood plasma viscosity of $1.072 \text{ mPa}\cdot\text{s}$. Platelet flips under linear shear flow for 1.1 ms in total, during which the stress accumulation of 44 coarse grained filaments is computed. The per-particle stress tensor is computed using the virial stress formula,

$$\begin{aligned}
S_{ab} = & -[mv_a v_b + \frac{1}{2} \sum_{n=1}^{N_p} (r_{1a} F_{1b} + r_{2a} F_{2b}) + \frac{1}{2} \sum_{n=1}^{N_b} (r_{1a} F_{1b} + r_{2a} F_{2b}) \\
& + \frac{1}{3} \sum_{n=1}^{N_a} (r_{1a} F_{1b} + r_{2a} F_{2b} + r_{3a} F_{3b}) \\
& + \frac{1}{4} \sum_{n=1}^{N_d} (r_{1a} F_{1b} + r_{2a} F_{2b} + r_{3a} F_{3b} + r_{4a} F_{4b}) \\
& + \frac{1}{4} \sum_{n=1}^{N_i} (r_{1a} F_{1b} + r_{2a} F_{2b} + r_{3a} F_{3b} + r_{4a} F_{4b})]
\end{aligned} \tag{V-1}$$

Note that S_{ab} has unit of stress * volume, it needs to be divided by a per-atom volume to get unit of stress. Such a per-atom volume is estimated by calculating the Voronoi tessellation of the atoms in the simulation box^{27,114}.

The stress tensor is then converted into a scalar value using formula,

$$\tau(t_i) = \frac{1}{\sqrt{3}} \sqrt{\tau_{xx}^2 + \tau_{yy}^2 + \tau_{zz}^2 - \tau_{xx}\tau_{yy} - \tau_{xx}\tau_{zz} - \tau_{yy}\tau_{zz} + 3(\tau_{xy}^2 + \tau_{yz}^2 + \tau_{xz}^2)} \tag{V-2}$$

5.2.3 Pseudopodia formation

A stress threshold T is defined, beyond which the corresponding filament extends and promotes pseudopodia formation. To achieve a physiological like activated platelet with multiple filopodia, k filaments with highest stress levels are defined to be protrusible ($k \geq 1$). The backbone potential energies are changed to extend the filaments in response to elevated stresses while the side chains remain their state and provide structural support to the filament's backbones. The time scale in pseudopodia formation is 1 ps, corresponding to $dt=5e-7$. Three steps are taken to extend protrusible filaments, 1) uncoil helical structure by changing dihedral potentials, 2) straighten the uncoiled structure by changing angle potentials, 3) promote the elongation of pseudopodia by changing bond potentials (Figure V-2).

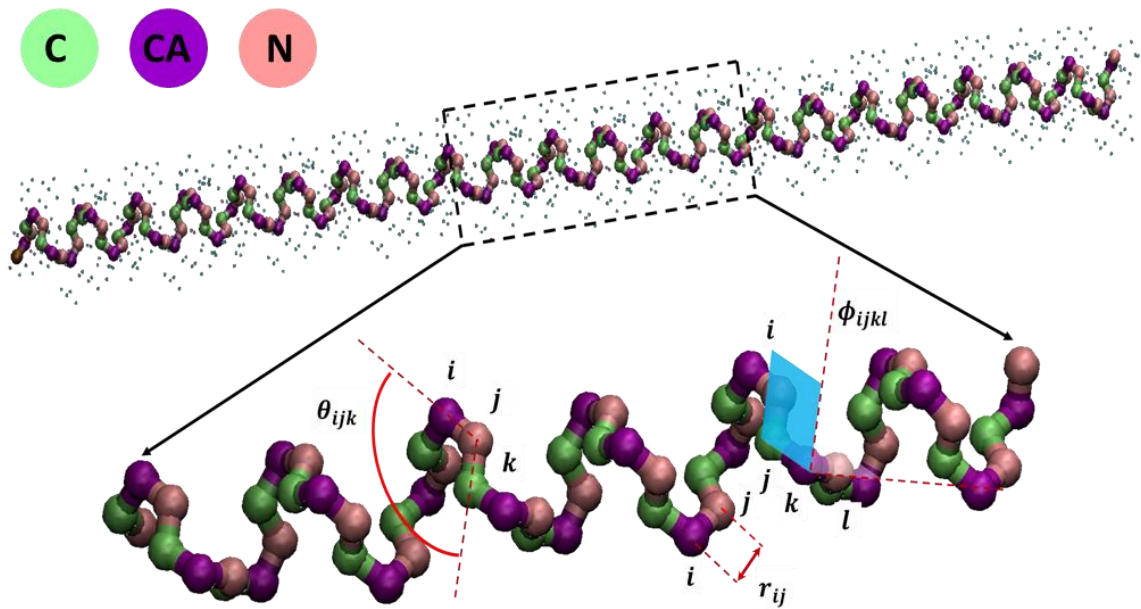


Figure V-2. One cytoskeleton filament of platelet. Helical structure is based on polypeptide chain. The tip starts with Nitrogen atom, and repeats in a pattern of N-CA-C. The dynamics of the filament is governed by bond, angle and dihedral potentials.

Step 1 – uncoil the helical structure

The charmm style dihedral potential is defined by

$$E = K[1 + \cos(n\phi - d)] \quad (\text{V-3})$$

where K is the force constant, n is the multiplicity of energy minima as the bond is rotated through 360° , and d is the angle where the potential passes through its minimum value. To uncoil the activated filament, parameters of three dihedral potentials C-N-CA-C, CA-C-N-CA, N-CA-C-N are adjusted.

Step 2 – straighten the filament

Harmonic style angle potentials is defined by

$$E = K(\theta - \theta_0)^2 \quad (\text{V-4})$$

where θ_0 is the equilibrium angle, and K is a scaling factor.

Once the coarse grained filament is uncoiled, three angle potentials of backbone are adjusted, CA-N-C, CA-C-N, N-CA-C. Besides, three more types of angle potentials are defined to straighten the filament: 1) short range harmonic angle defined between 1-2-3 neighboring particles of same type; 2) medium range harmonic angle defined between 1-3-5, 1-4-7 neighboring particles of same type; 3) and long range class 2 angle defined between 1-10-19 neighboring particles of same type.

Step 3 – elongate the filament

After the filament is straightened, the harmonic bond potentials of neighboring particles are adjusted by increasing K value to increase the length of filament to promote filament protrusion.

5.2.4 Validation by in-vitro experiment

Gel-filtered platelets were prepared and diluted to a final count of 20, 000/ul in HEPES-buffered modified Tyrodes solution with 3 mM Ca^{2+} added 10 min prior to experiments. The platelets were exposed to constant shear stresses of 10, 20, 30, 40 and 50 dyne/cm² for 4 min in the Hemodynamic Shearing Device (HSD). Samples were drawn at 0, 15, 30, 45, 60, 120, 180, 240 s, and immediately fixed with 2% glutaraldehyde in platelet buffer.

The samples were imaged in SEM microscope (LEO 1550) at 30, 000x magnification. Platelet shape, number of pseudopodia were measured using NIH ImageJ software.

5.3 Results

5.3.1 Shear-induced platelet activation

Being exposed to shear stress of 85.76 dyne/cm², the platelet takes several flipping periods during which the stress accumulation of 44 actin filaments are computed. Five filaments are selected for protrusion with highest values among all filaments. It is found that two of them connect to the top and bottom surfaces of platelet, and three other filaments connect to the edge of platelet. The five filaments transit from initially helical structure to the elongated filaments by uncoiling, straightening, and elongation. The length of the filaments are significantly increased, while the diameter is greatly reduced. The rest of non-protrusible filaments becomes an actin network (Figure V-3 and 4).

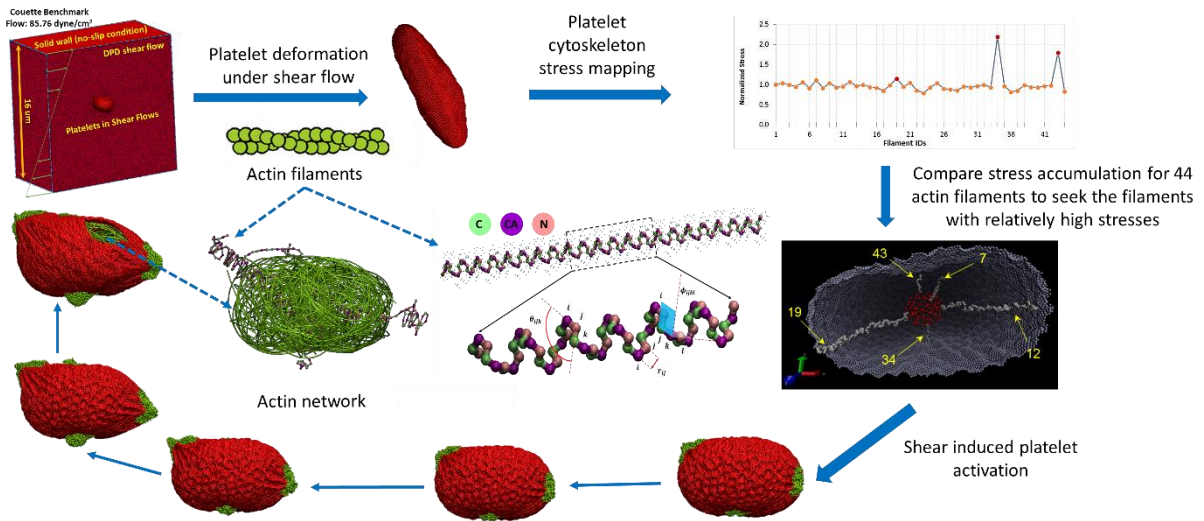


Figure V-3. Shear-induced platelet activation process. The platelet flips and deforms under linear shear flow with 85.76 dyne/cm^2 . The stress accumulation of 44 actin filaments is computed during 1.1 ms simulations, and five filaments with most highest values are selected for protrusion (filament No. 7, 12, 19, 34, and 43). The protrusible actin filaments transit from initial helical structure to elongated filaments to induce pseudopodia formation.

These two different morphologies of actin filaments represent bundled and cross-linked F-actin networks, respectively. This conformational change is consistent with the transition from alpha-helix to beta-sheet in protein under stretching force ^{69,70}.

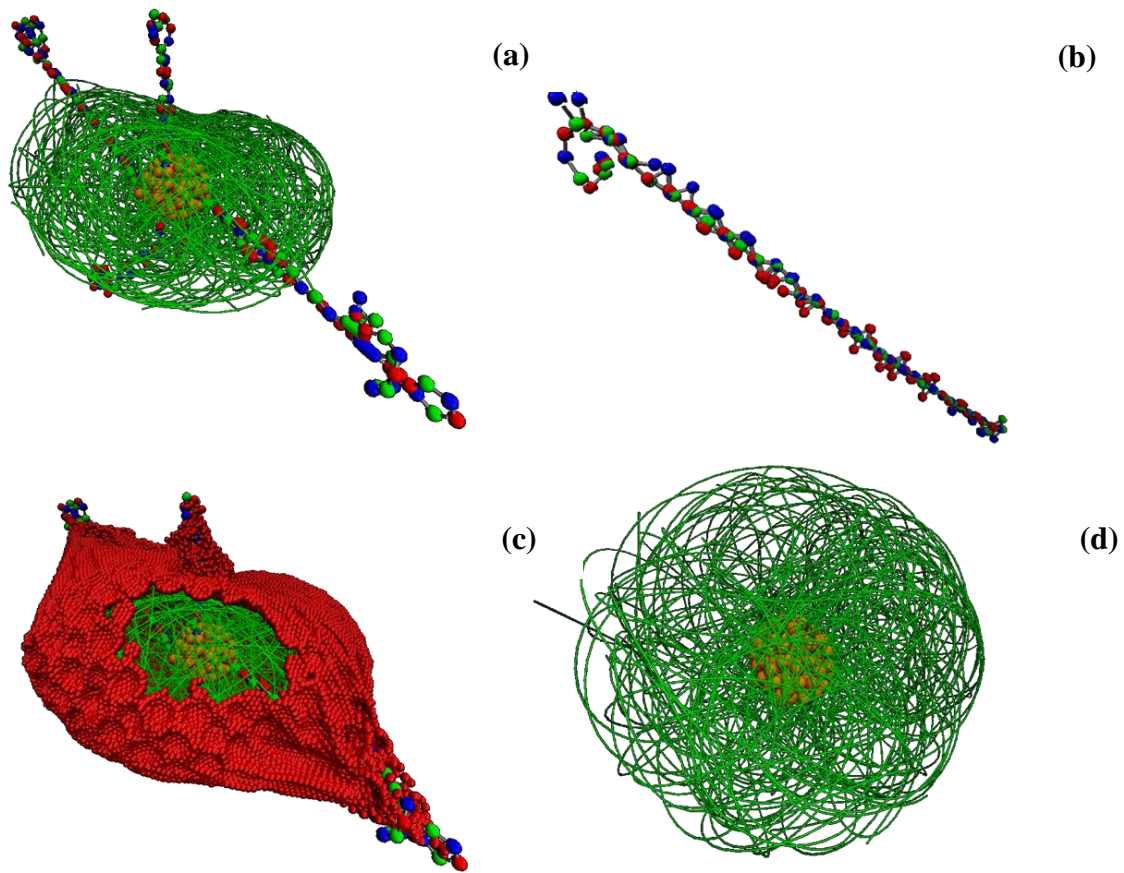


Figure V-4. Illustration of platelet activation model. (a) Cytoskeleton with five elongated actin filaments. (b) A single protrusible filament. (c) Whole activated platelet model with five pseudopodia. (d) Description of actin network composed of non-protrusible filaments.

5.3.2 Morphological analysis of pseudopodia formation

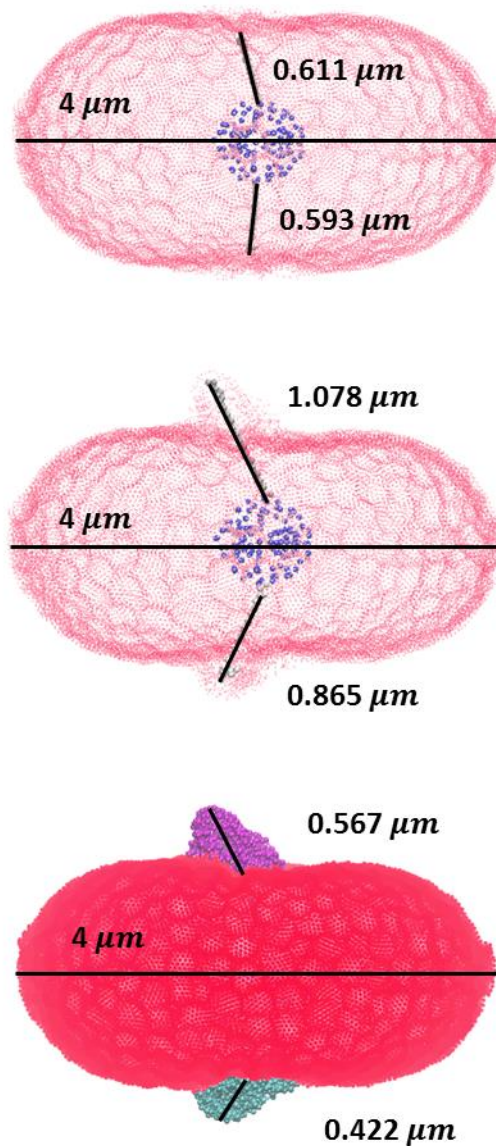
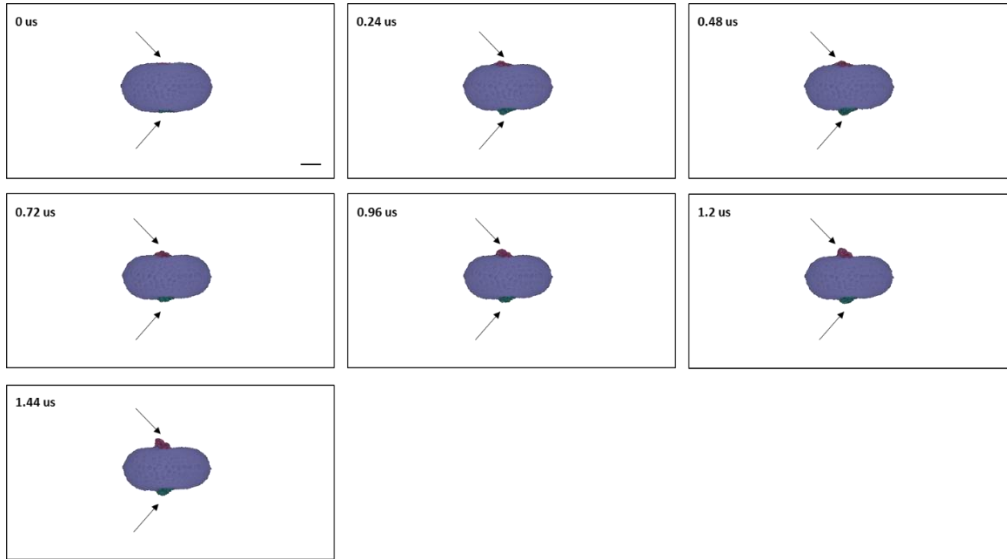


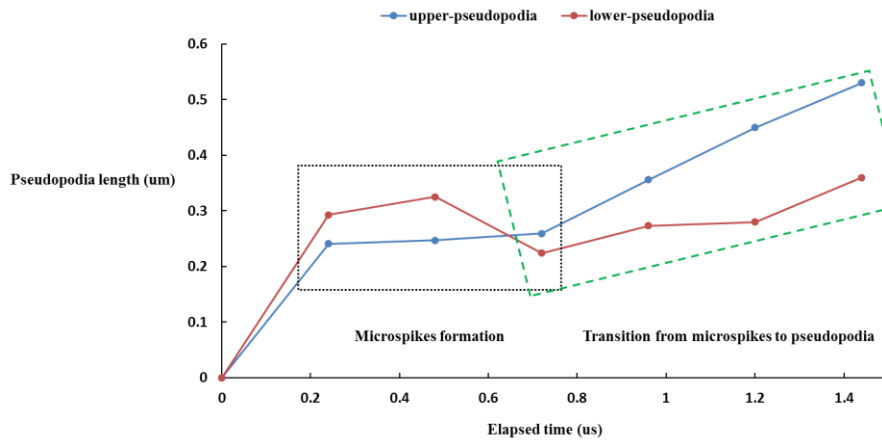
Figure V-5. Two pseudopodia formation on top and bottom surfaces of platelet. The pseudopodia lengths are 0.567 and $0.422 \mu\text{m}$, respectively. The diameter of platelet remains $4 \mu\text{m}$.

In the case of two pseudopodia formation, the top filament elongates from $0.611 \mu\text{m}$ to $1.078 \mu\text{m}$, an 76% increase in length, and the bottom filament elongates from $0.593 \mu\text{m}$ to $0.865 \mu\text{m}$, corresponding to 46% increase in length (Figure V-5). Observing platelet from exterior, the

top pseudopod has a length of 0.567 μm , and bottom one has a length of 0.422 μm . The overall shape of platelet remains similar before and after activation. The SEM images of activated platelets under shear stresses 10, 30, and 50 dyne/cm^2 and exposure times 30, 60, 120, 180 and 240 seconds show that the length of pseudopodia ranges from 0.4 to 1.5 μm . The top and bottom pseudopodia in our simulation have a length within the range observed in experiments.



(a)



(b)

Figure V-6. (a) Time-lapse sequence of two pseudopodia formation (arrowheads). The platelet membrane initially maintains ellipsoidal shape (0 us). Two microspikes protrude from platelet membrane (0.24 us), continue to elongate and transit to short pseudopodia (0.24 to 1.44 us). Bars, 1 μm . (b) Pseudopodia growth length. Microspikes form as result of initial protrusion of

actin filament bundles (0.2 to 0.3 μm). Withdrawal is observed during the protrusion process (lower pseudopodia). Microspikes then transit to pseudopodia formation with end length of 0.5 to 0.6 μm .

Figure V-6 shows the protrusion process of two short pseudopodia, in which the platelet keeps ellipsoidal shape at initial observation point. Two microspikes then appear at top and bottom sides of platelet membrane, elongate and transit to short pseudopodia at final time points (1.44 μs).

5.4 Discussion and conclusions

Platelet shape change upon activation can be observed experimentally by atomic force microscopy (AFM) on unfixed and living platelet adhered to glass over the full lifetime of platelet from early activation to apoptosis⁶⁶. Such observation can achieve nanometer lengthscale and minutes timescale. The platelets are observed to go through a sequence of morphological changes, i.e., first phase with filopodia formation, cell blebbing, second phase with filopodia formation, cell shrinkage and apoptosis. With the absence of chemical agonists such as vWF, collagen and ADP, the morphological changes are significantly slowed down. Furthermore, platelet dynamic shape change is observed during adhesive process to thrombogenic surface under physiological flow environment (1500 s^{-1})³⁷. Besides chemical agonists, platelets can also be activated by fluid shear in cardiovascular diseases and prosthetic devices. The shear-induced platelet activation is studied in-vitro by exposing platelets to different levels of shear stress for various exposure time in a hemodynamic shearing device (HSD), then measuring the rate of thrombin generation with platelet activation state assay (PAS)⁷⁵. To visualize the platelet shape change, activated platelets are withdrawn and fixed to be imaged by SEM microscope, from which the number and size of pseudopodia can be determined for observed platelets⁶⁷. While AFM traces the platelet shape change on single platelet level, the shear-induced platelet activation experiments involve a large number of platelets (20,000/ μl).

In the current work, an in-silico multiscale shear-induced platelet activation model was developed to complement the in-vitro experiments and furthermore provide prediction to guide future experiments. In this model, a reductionist approach is adopted which only focuses on the mechanical stress transmission from blood plasma to platelet membrane and cytoskeleton. Despite excluding biochemical pathways involved in platelet activation, it remains the predictive capabilities of the phenomena.

The platelet model here serves as an “average” of all platelets with various sizes, shapes, and ages. Essential components on the mechanotransduction pathways are modeled, i.e., the blood plasma flow, the platelet membrane, actin filaments and core, and cytoplasm. Multiple scales are naturally incurred in this model, where the blood plasma is presented by a mesoscopic particle ensemble on the μm scale, and the platelet is described on the nm scale.

In our cytoskeleton model, the 44 coarse grained actin filaments have lengths from 100 to 800 nm. In vitro, actin filaments are able to polymerize to form long rigid filaments with contour lengths up to $20 \mu m$ ²². Instead of directly modeling actin polymerization and treadmilling, we employed the alpha helix structure to represent bundled actin filaments and by elongating the alpha helix structure, simulated the process of actin polymerization and pseudopodia formation on μm scale. Using a coarse grained filament model here minimizes the computational burden yet is able to model the desired phenomena.

Actin filaments are able to sense fluid shear stress and experience reorganization through signaling pathways induced by fluid shear^{28,61}. In the current work, the mechanosensing of actin filaments is described quantitatively by the stress accumulation level on individual actin filament. In consequence, the actin filaments polymerize through a conformational change of uncoiling, straightening, and elongation, and interact with platelet membrane to form pseudopodia. The

pseudopodia formation occurs on a length scale (μm) three orders larger than the scale of actin monomers (nm), and polymerization of actin filaments can be modeled by the conformational change of coarse grained filament model with much less degrees of freedom.

VI. Conclusions and future work

Thrombosis in cardiovascular diseases and prosthetic cardiovascular devices can be potentiated by pathological flow patterns that enhance the propensity of platelets to be activated. In the past, the phenomena of fluid shear-induced platelet activation are investigated on separate physical scales: on the top scale, the hemodynamics in blood vessels and prosthetic devices are assumed to be continuum and are studied based on Navier-Stokes equations; on the bottom scale, the platelet activation is represented by measuring the thrombin generation and expression of platelet surface thrombogenic markers. Though shear stress and exposure time have been correlated to platelet activation in vitro, the mechanotransduction process underneath the phenomena remains unclear. In the current work, the mechanotransduction process during shear-induced platelet activation is studied by employing a multiscale modeling approach spanning from the macroscopic blood flow phenomena to the microscopic actin filaments elongation and pseudopodia formation. Such multiscale approach is based on discrete particle dynamics, including dissipative particle dynamics (DPD) that addresses the viscous fluid flow phenomena, and coarse grained molecular dynamics (CGMD) that models individual platelet with sub-components, i.e., membrane, cytoskeleton, and cytoplasm. This multiscale method contributes to bridge the gap between continuum model described by the N-S equations and fully atomistic model described by the molecular dynamics.

On macroscopic scale relevant to arterioles and capillaries, the viscous fluid flow behaviors are reproduced by DPD. The dynamic viscosity can be extracted from the particle simulation by fitting the simulation results with analytical solution of N-S equations. The no-slip boundary condition on 3D complex geometries is imposed by discretizing the wall geometry to triangular elements, on which the boundary forces contributing to no-slip BC are locally applied. A coarse-

grained platelet model is developed with single layer membrane. Besides DPD force field, the membrane particles interact with neighbors through harmonic bond potential that represents the membrane elasticity and harmonic dihedral potential that provides the bending rigidity. The platelet suspensions through 3D stenotic microchannel is studied. The platelet-platelet and platelet-wall interactions are observed. Platelets along the centerline of microchannel have higher velocity than platelets near the wall. Platelets experience acceleration and de-acceleration when passing through the stenotic throat. The slow-down of platelet transport near the boundary increases the opportunity for platelets to interact with wall. In the case of damaged blood vessel walls, this increases the propensity of platelets to be activated. The inflow/outflow boundary condition is developed to enable the pressure gradient driven fluid flow. The mass is conserved by inserting new fluid particles at inlet and removing old fluid particles at outlet. Boundary force schemes are applied to maintain correct particle interaction near inlet/outlet. Due to the compressible effect of DPD fluid flow, increasing the flow rate would lead to unbalanced density distribution along flow direction.

In the presence of severe stenosis, the compressible effect of DPD fluid flow becomes evident because of the soft interaction potential of DPD force field. This is mitigated by using the DPD-Morse fluid model, where the short range repulsive term of Morse potential serves as a hard core of DPD fluid particle to sustain large compression. If the fluid system does not experience any compression, such as in the counter-Poiseuille flow, the DPD and DPD-Morse fluid models demonstrate similar fluid dynamic and equilibrium properties such as velocity, number density, shear stress and radial distribution function. The only difference is observed in fluid pressure, where the DPD-Morse potential has a relative higher pressure than DPD fluid. These observations indicate that the Morse potential only alters the system pressure of the fluid, without changing the

viscous properties. In severe stenotic microchannel, the DPD-Morse fluid model demonstrates a mild density gradient as opposed to large density gradient found in DPD fluid. A rigid platelet model is embedded into two types of fluids. As platelet traverses through the microchannel, the shear stress along its traversing trajectory is similar in between DPD and DPD-Morse fluids. However, the platelet in DPD fluids traverses faster than in the DPD-Morse fluids as a result of significant density gradient. The DPD-Morse fluid was verified against CFD simulation results and compared favorably with the continuum simulations. The DPD-Morse fluid model offers a more accurate description of shear stress accumulation along platelet traversing trajectory through severe stenotic microchannel, where the original DPD fluid model underestimates the platelet's exposure time to shear stress.

To couple the microscale blood plasma model to the nanoscale platelet model, a hybrid potential is employed between fluid particle and membrane particle including Lennard-Jones term that addresses the interaction on molecular scale, and the DPD thermostat to maintain local temperature. To parameterize the hybrid potential, the flipping motion of a rigid platelet model under linear shear flow is studied and validated against analytical solution by Jeffery. The platelet flipping is driven by the external force and torque provided by fluid system via the hybrid potential. The simulation results show that the parameters of Lennard-Jones term play dominant roles in platelet flipping frequency, whereas DPD thermostat does not affect the flipping motion.

Furthermore, the surface stress of platelet membrane is computed and compared in between rigid and deformable platelets. For each membrane particle, the virial stress is computed at every timestep, and is averaged over time to get the time-averaging observable. The rigid platelet demonstrates 2.6 times higher in surface stress than the deformable platelet. As real platelets have

certain deformability, this result indicates that the rigid platelet model presents an overestimated surface stress accumulation compared to the deformable platelet.

The spatial-temporal coarse graining effects are further investigated. At smaller timescale such as nanosecond, the platelet membrane only demonstrates the particle fluctuations. By applying time-averaging over a larger timescale, certain patterns appear on the platelet membrane, meaning that such pattern in membrane velocity or stress can only be observed at microsecond scale. The effects of spatial coarse-graining are studied by applying a coarser mesh to platelet membrane and averaging particle information within the neighborhood of each mesh vertex. The velocity/stress patterns are very clear when the initial mesh with 19675 nodes are employed. As the number of mesh nodes are gradually reduced, the patterns are deteriorated. The spatial-temporal averaging analysis gives us a good sense of the physical scales we need in order to get the desired membrane properties.

Furthermore, the stress accumulation of 44 coarse grained actin filaments is computed. The actin filaments with highest stress accumulation values go through a conformational change to elongate and enforce the protrusion of membrane. 1-5 pseudopodia are formed in the simulation of platelet under shear flow, and can be validated by the SEM images of shear-induced platelet activation at fixed time points.

The future work can be conducted on both top and bottom scales. On top scale, the DPD fluid model can be coupled to the continuum fluid model by exchanging boundary information between DPD fluid particles and continuum mesh grids. On bottom scale, the platelet-platelet aggregation through GPIIb α -vWF-GPIIb α can be modeled by applying Morse potential with attractive term between membrane particles of different platelets. The platelet activation will further extend the contact area between two platelets and facilitate the aggregation process. These

improvements would strengthen our multiscale model to address the platelet-mediated thrombus formation at nm resolution induced by fluid shear in μm scale.

References

1. Alemu, Y. and D. Bluestein. Flow - induced Platelet Activation and Damage Accumulation in a Mechanical Heart Valve: Numerical Studies. *Artificial Organs*. 31:677-688, 2007.
2. Backer, J. A., C. P. Lowe, H. C. J. Hoefsloot, and P. D. Iedema. Poiseuille flow to measure the viscosity of particle model fluids. *Journal of Chemical Physics*. 122, 2005.
3. Besold, G., I. Vattulainen, M. Karttunen, and J. M. Polson. Towards better integrators for dissipative particle dynamics simulations. *Physical Review E*. 62:R7611-R7614, 2000.
4. Bluestein, D. Research approaches for studying flow-induced thromboembolic complications in blood recirculating devices. *Expert Review of Medical Devices*. 1:65-80, 2004.
5. Boromand, A., S. Jamali, and J. M. Maia. Viscosity measurement techniques in Dissipative Particle Dynamics. *Computer Physics Communications*. 196:149-160, 2015.
6. Brown, C. H., L. B. Leverett, C. W. Lewis, C. P. Alfrey, and J. D. Hellums. Morphological, biochemical, and functional changes in human platelets subjected to shear stress. *The Journal of Laboratory and Clinical Medicine*. 86:462-471, 1975.
7. Chandran, K. B., S. E. Rittgers, and A. P. Yoganathan. Biofluid mechanics: the human circulation: CRC Press; 2012.
8. Chesnutt, J. K. and H.-C. Han. Platelet size and density affect shear-induced thrombus formation in tortuous arterioles. *Physical Biology*. 10:056003, 2013.
9. Chiu, S.-W., H. L. Scott, and E. Jakobsson. A Coarse-Grained Model Based on Morse Potential for Water and n-Alkanes. *Journal of Chemical Theory and Computation*. 6:851-863, 2010.
10. Dzwinel, W., K. Boryczko, and D. A. Yuen. A discrete-particle model of blood dynamics in capillary vessels. *Journal of colloid and interface science*. 258:163-173, 2003.
11. Einav, S. and D. Bluestein. Dynamics of blood flow and platelet transport in pathological vessels. *Cardiac Engineering: From Genes and Cells to Structure and Function*. 1015:351-366, 2004.
12. Fedosov, D. A., B. Caswell, and G. E. Karniadakis. A Multiscale Red Blood Cell Model with Accurate Mechanics, Rheology, and Dynamics. *Biophysical journal*. 98:2215-2225, 2010.
13. Fedosov, D. A., M. Dao, G. E. Karniadakis, and S. Suresh. Computational biorheology of human blood flow in health and disease. *Ann Biomed Eng*. 42:368-387, 2014.
14. Fedosov, D. A., W. Pan, B. Caswell, G. Gompper, and G. E. Karniadakis. Predicting human blood viscosity in silico. *Proceedings of the National Academy of Sciences*. 108:11772-11777, 2011.
15. Fedosov, D. A., I. V. Pivkin, and G. E. Karniadakis. Velocity limit in DPD simulations of wall-bounded flows. *Journal of Computational Physics*. 227:2540-2559, 2008.
16. Feghhi, S. and N. J. Sniadecki. Mechanobiology of platelets: techniques to study the role of fluid flow and platelet retraction forces at the micro- and nano-scale. *Int J Mol Sci*. 12:9009-9030, 2011.
17. Feng, R., M. Xenos, G. Girdhar, W. Kang, J. W. Davenport, Y. Deng, and D. Bluestein. Viscous flow simulation in a stenosis model using discrete particle dynamics: a comparison between DPD and CFD. *Biomech Model Mechanobiol*. 11:119-129, 2012.
18. Feng, R., M. Xenos, G. Girdhar, W. Kang, J. W. Davenport, Y. F. Deng, and D. Bluestein. Viscous flow simulation in a stenosis model using discrete particle dynamics: a comparison between DPD and CFD. *Biomechanics and Modeling in Mechanobiology*. 11:119-129, 2012.
19. Filipovic, N., M. Kojic, and A. Tsuda. Modelling thrombosis using dissipative particle dynamics method. *Philos Trans A Math Phys Eng Sci*. 366:3265-3279, 2008.
20. Finkenstaedt-Quinn, S. A., S. C. Ge, and C. L. Haynes. Cytoskeleton dynamics in drug-treated platelets. *Analytical and Bioanalytical Chemistry*. 407:2803-2809, 2015.

21. Flamm, M. H. and S. L. Diamond. Multiscale Systems Biology and Physics of Thrombosis Under Flow. *Annals of Biomedical Engineering*. 40:2355-2364, 2012.
22. Gardel, M. L., J. H. Shin, F. C. MacKintosh, L. Mahadevan, P. Matsudaira, and D. A. Weitz. Elastic Behavior of cross-linked and bundled actin networks. *Science*. 304:1301-1305, 2004.
23. Groot, R. and P. Warren. Dissipative particle dynamics: Bridging the gap between atomistic and mesoscopic simulation. *The Journal of Chemical Physics*. 107:4423-4435, 1997.
24. Guo, J., X. Li, Y. Liu, and H. Liang. Flow-induced translocation of polymers through a fluidic channel: A dissipative particle dynamics simulation study. *The Journal of chemical physics*. 134:134906, 2011.
25. Haga, J., A. Beaudoin, J. White, and J. Strony. Quantification of the Passive Mechanical Properties of the Resting Platelet. *Annals of Biomedical Engineering*. 26:268-277, 1998.
26. Hartwig, J. H. a. M. D. The cytoskeleton of the resting human blood platelet: structure of the membrane skeleton and its attachment to actin filaments. *The Journal of Cell Biology*. 112:407-425, 1991.
27. Hatch, H. W. and P. G. Debenedetti. Molecular modeling of mechanical stresses on proteins in glassy matrices: Formalism. *Journal of Chemical Physics*. 137, 2012.
28. Honjo, T., S. Kubota, H. Kamioka, Y. Sugawara, Y. Ishihara, T. Yamashiro, M. Takigawa, and T. Takano-Yamamoto. Promotion of Ccn2 expression and osteoblastic differentiation by actin polymerization, which is induced by laminar fluid flow stress. *Journal of Cell Communication and Signaling*. 6:225-232, 2012.
29. Idiris, A., M. T. Alam, and A. Ikai. Spring mechanics of alpha-helical polypeptide. *Protein Eng*. 13:763-770, 2000.
30. Janostiak, R., A. C. Pataki, J. Brabek, and D. Rosel. Mechanosensors in integrin signaling: The emerging role of p130Cas. *European Journal of Cell Biology*. 93:445-454, 2014.
31. Jeffery, G. B. The Motion of Ellipsoidal Particles Immersed in a Viscous Fluid. *Proceedings of the Royal Society of London. Series A*. 102:161-179, 1922.
32. Jesty, J., W. Yin, P. Perrotta, and D. Bluestein. Platelet activation in a circulating flow loop: combined effects of shear stress and exposure time. *Platelets*. 14:143-149, 2003.
33. Karplus, M. and J. A. McCammon. Molecular dynamics simulations of biomolecules. *Nature Structural & Molecular Biology*. 9:646-652, 2002.
34. Kesmarky, G., P. Kenyeres, M. Rabai, and K. Toth. Plasma viscosity: A forgotten variable. *Clinical Hemorheology and Microcirculation*. 39:243-246, 2008.
35. Koutsiaris, A. G., S. V. Tachmitzi, and N. Batis. Wall shear stress quantification in the human conjunctival pre-capillary arterioles in vivo. *Microvascular Research*. 85:34-39, 2013.
36. Ku, D. N. Blood flow in arteries. *Annual Review of Fluid Mechanics*. 29:399-434, 1997.
37. Kuwahara, M., M. Sugimoto, S. Tsuji, H. Matsui, T. Mizuno, S. Miyata, and A. Yoshioka. Platelet shape changes and adhesion under high shear flow. *Arteriosclerosis Thrombosis and Vascular Biology*. 22:329-334, 2002.
38. Lam, W. A., O. Chaudhuri, A. Crow, K. D. Webster, T. D. Li, A. Kita, J. Huang, and D. A. Fletcher. Mechanics and contraction dynamics of single platelets and implications for clot stiffening. *Nature Materials*. 10:61-66, 2011.
39. Le Clairche, C. and M. F. Carlier. Regulation of actin assembly associated with protrusion and adhesion in cell migration. *Physiological Reviews*. 88:489-513, 2008.
40. Lei, H. A., D. A. Fedosov, and G. E. Karniadakis. Time-dependent and outflow boundary conditions for Dissipative Particle Dynamics. *Journal of Computational Physics*. 230:3765-3779, 2011.

41. Letort, G., A. Z. Politi, H. Ennomani, M. Thery, F. Nedelec, and L. Blanchoin. Geometrical and Mechanical Properties Control Actin Filament Organization. *Plos Computational Biology*. 11, 2015.
42. Leung, S. L., Y. Lu, D. Bluestein, and M. J. Slepian. Dielectrophoresis-Mediated Electrodeformation as a Means of Determining Individual Platelet Stiffness. *Ann Biomed Eng*. 2015.
43. Li, J., M. Dao, C. T. Lim, and S. Suresh. Spectrin-level modeling of the cytoskeleton and optical tweezers stretching of the erythrocyte. *Biophys J*. 88:3707-3719, 2005.
44. Li, X. J., A. S. Popel, and G. E. Karniadakis. Blood-plasma separation in Y-shaped bifurcating microfluidic channels: a dissipative particle dynamics simulation study. *Physical Biology*. 9, 2012.
45. Lipowsky, H. H. Microvascular rheology and hemodynamics. *Microcirculation*. 12:5-15, 2005.
46. Liu, Y. L., L. Zhang, X. D. Wang, and W. K. Liu. Coupling of Navier-Stokes equations with protein molecular dynamics and its application to hemodynamics. *International Journal for Numerical Methods in Fluids*. 46:1237-1252, 2004.
47. Lloyd-Jones, D., R. Adams, M. Carnethon, G. De Simone, T. B. Ferguson, K. Flegal, E. Ford, K. Furie, A. Go, K. Greenlund, N. Haase, S. Hailpern, M. Ho, V. Howard, B. Kissela, S. Kittner, D. Lackland, L. Lisabeth, A. Marelli, M. McDermott, J. Meigs, D. Mozaffarian, G. Nichol, C. O'Donnell, V. Roger, W. Rosamond, R. Sacco, P. Sorlie, R. Stafford, J. Steinberger, T. Thom, S. Wasserthiel-Smoller, N. Wong, J. Wylie-Rosett, Y. L. Hong, W. G. MEMBERS, A. H. A. S. Comm, and S. S. Subcomm. Heart Disease and Stroke Statistics-2009 Update A Report From the American Heart Association Statistics Committee and Stroke Statistics Subcommittee. *Circulation*. 119:480-486, 2009.
48. Lykov, K., X. J. Li, H. Lei, I. V. Pivkin, and G. E. Karniadakis. Inflow/Outflow Boundary Conditions for Particle-Based Blood Flow Simulations: Application to Arterial Bifurcations and Trees. *Plos Computational Biology*. 11, 2015.
49. Mairey, E., A. Genovesio, E. Donnadieu, C. Bernard, F. Jaubert, E. Pinard, J. Seylaz, J.-C. Olivo-Marin, X. Nassif, and G. Duménil. Cerebral microcirculation shear stress levels determine *Neisseria meningitidis* attachment sites along the blood–brain barrier. *The Journal of experimental medicine*. 203:1939-1950, 2006.
50. Mar, S., F. Gianni De, E. Pep, G. F. Eirik, and V. C. Peter. Mesoscopic dynamics of Voronoi fluid particles. *Journal of Physics A: Mathematical and General*. 35:1605, 2002.
51. Mody, N. A. and M. R. King. Platelet adhesive dynamics. Part I: Characterization of platelet hydrodynamic collisions and wall effects. *Biophysical Journal*. 95:2539-2555, 2008.
52. Mody, N. A. and M. R. King. Platelet adhesive dynamics. Part II: High shear-induced transient aggregation via GPIb alpha-vWF-GPIb alpha bridging. *Biophysical Journal*. 95:2556-2574, 2008.
53. Mody, N. A. and M. R. King. Three-dimensional simulations of a platelet-shaped spheroid near a wall in shear flow. *Physics of Fluids*. 17, 2005.
54. Mody, N. A., O. Lomakin, T. A. Doggett, T. G. Diacovo, and M. R. King. Mechanics of transient platelet adhesion to von Willebrand factor under flow. *Biophysical Journal*. 88:1432-1443, 2005.
55. Moiseyev, G. and P. Z. Bar-Yoseph. Computational modeling of thrombosis as a tool in the design and optimization of vascular implants. *Journal of Biomechanics*. 46:248-252, 2013.
56. Morse, P. M. Diatomic molecules according to the wave mechanics. II. Vibrational levels. *Physical Review*. 34:57-64, 1929.
57. Moses, K. B., S. G. Advani, and A. Reinhardt. Investigation of fiber motion near solid boundaries in simple shear flow. *Rheologica Acta*. 40:296-306, 2001.
58. Omori, T., Y. Imai, K. Kikuchi, T. Ishikawa, and T. Yamaguchi. Hemodynamics in the Microcirculation and in Microfluidics. *Annals of Biomedical Engineering*. 43:238-257, 2015.

59. Pan, D., N. Phan-Thien, N. Mai-Duy, and B. C. Khoo. Numerical investigations on the compressibility of a DPD fluid. *Journal of Computational Physics*. 242:196-210, 2013.
60. Pastorino, C., K. Binder, and M. Muller. Coarse-Grained Description of a Brush-Melt Interface in Equilibrium and under Flow. *Macromolecules*. 42:401-410, 2009.
61. Pavalko, F. M., N. X. Chen, C. H. Turner, D. B. Burr, S. Atkinson, Y. F. Hsieh, J. Y. Qiu, and R. L. Duncan. Fluid shear-induced mechanical signaling in MC3T3-E1 osteoblasts requires cytoskeleton-integrin interactions. *American Journal of Physiology-Cell Physiology*. 275:C1591-C1601, 1998.
62. Pivkin, I. V. and G. E. Karniadakis. Coarse-graining limits in open and wall-bounded dissipative particle dynamics systems. *Journal of Chemical Physics*. 124, 2006.
63. Pivkin, I. V. and G. E. Karniadakis. A new method to impose no-slip boundary conditions in dissipative particle dynamics. *Journal of Computational Physics*. 207:114-128, 2005.
64. Plimpton, S. Fast Parallel Algorithms for Short-Range Molecular-Dynamics. *Journal of Computational Physics*. 117:1-19, 1995.
65. Plimpton, S., A. Thompson, and P. Crozier. LAMMPS Molecular Dynamics Simulator. 2014.
66. Posch, S., I. Neundlinger, M. Leitner, P. Siostrzonek, S. Panzer, P. Hinterdorfer, and A. Ebner. Activation induced morphological changes and integrin alpha IIb beta 3 activity of living platelets. *Methods*. 60:179-185, 2013.
67. Pothapragada, S., P. Zhang, J. Sheriff, M. Livelli, M. J. Slepian, Y. Deng, and D. Bluestein. A phenomenological particle-based platelet model for simulating filopodia formation during early activation. *Int J Numer Method Biomed Eng*. 31, 2015.
68. Potters, W. V., H. A. Marquering, E. VanBavel, and A. J. Nederveen. Measuring wall shear stress using velocity-encoded MRI. *Current Cardiovascular Imaging Reports*. 7:1-12, 2014.
69. Qin, Z. and M. J. Buehler. Molecular Dynamics Simulation of the alpha-Helix to beta-Sheet Transition in Coiled Protein Filaments: Evidence for a Critical Filament Length Scale. *Physical Review Letters*. 104, 2010.
70. Qin, Z., L. Kreplak, and M. J. Buehler. Hierarchical Structure Controls Nanomechanical Properties of Vimentin Intermediate Filaments. *Plos One*. 4, 2009.
71. Rudd, R. E. and J. Q. Broughton. Coarse-grained molecular dynamics and the atomic limit of finite elements. *Physical Review B*. 58:R5893, 1998.
72. Samijo, S., J. Willigers, R. Barkhuysen, P. Kitslaar, R. Reneman, P. Brands, and A. Hoeks. Wall shear stress in the human common carotid artery as function of age and gender. *Cardiovascular research*. 39:515-522, 1998.
73. Satoh, A. and T. Majima. Comparison between theoretical values and simulation results of viscosity for the dissipative particle dynamics method. *Journal of colloid and interface science*. 283:251-266, 2005.
74. Shanmugavelayudam, S. K., D. A. Rubenstein, and W. Yin. Effect of Geometrical Assumptions on Numerical Modeling of Coronary Blood Flow Under Normal and Disease Conditions. *Journal of Biomechanical Engineering-Transactions of the Asme*. 132, 2010.
75. Sheriff, J., D. Bluestein, G. Girdhar, and J. Jesty. High-shear stress sensitizes platelets to subsequent low-shear conditions. *Ann Biomed Eng*. 38:1442-1450, 2010.
76. Sheriff, J., J. S. Soares, M. Xenos, J. Jesty, and D. Bluestein. Evaluation of Shear-Induced Platelet Activation Models Under Constant and Dynamic Shear Stress Loading Conditions Relevant to Devices. *Ann Biomed Eng*. 41:1279-1296, 2013.
77. Sheriff, J., J. S. Soares, M. Xenos, J. Jesty, M. J. Slepian, and D. Bluestein. Evaluation of shear-induced platelet activation models under constant and dynamic shear stress loading conditions relevant to devices. *Ann Biomed Eng*. 41:1279-1296, 2013.

78. Shiozaki, S., S. Takagi, and S. Goto. Prediction of Molecular Interaction between Platelet Glycoprotein Iba and von Willebrand Factor using Molecular Dynamics Simulations. *Journal of Atherosclerosis and Thrombosis*. 2015.
79. Siess, W. Molecular Mechanisms of Platelet Activation. *Physiological Reviews*. 69:58-178, 1989.
80. Simon, H. A., L. Ge, F. Sotiropoulos, and A. P. Yoganathan. Numerical investigation of the performance of three hinge designs of bileaflet mechanical heart valves. *Annals of Biomedical Engineering*. 38:3295-3310, 2010.
81. Soares, J. S., C. Gao, Y. Alemu, M. Slepian, and D. Bluestein. Simulation of platelets suspension flowing through a stenosis model using a dissipative particle dynamics approach. *Ann Biomed Eng*. 41:2318-2333, 2013.
82. Soares, J. S., J. Sheriff, and D. Bluestein. A novel mathematical model of activation and sensitization of platelets subjected to dynamic stress histories. *Biomechanics and Modeling in Mechanobiology*. 12:1127-1141, 2013.
83. Soddemann, T., B. Dünweg, and K. Kremer. Dissipative particle dynamics: A useful thermostat for equilibrium and nonequilibrium molecular dynamics simulations. *Physical Review E*. 68:046702, 2003.
84. Svitkina, T. M., E. A. Bulanova, O. Y. Chaga, D. M. Vignjevic, S. Kojima, J. M. Vasiliev, and G. G. Borisy. Mechanism of filopodia initiation by reorganization of a dendritic network. *Journal of Cell Biology*. 160:409-421, 2003.
85. Sweet, C. R., S. Chatterjee, Z. L. Xu, K. Bisordi, E. D. Rosen, and M. Alber. Modelling platelet-blood flow interaction using the subcellular element Langevin method. *Journal of the Royal Society Interface*. 8:1760-1771, 2011.
86. Symeonidis, V. and G. E. Karniadakis. A family of time-staggered schemes for integrating hybrid DPD models for polymers: Algorithms and applications. *Journal of Computational Physics*. 218:82-101, 2006.
87. Takeishi, N., Y. Imai, K. Nakaaki, T. Yamaguchi, and T. Ishikawa. Leukocyte margination at arteriole shear rate. *Physiological reports*. 2:e12037, 2014.
88. Thompson, A. P., S. J. Plimpton, and W. Mattson. General formulation of pressure and stress tensor for arbitrary many-body interaction potentials under periodic boundary conditions. *J. Chem. Phys*. 131, 2009.
89. Tian, M., W. Gu, J. Pan, and M. Guo. Performance analysis and optimization of PalaBos on petascale Sunway BlueLight MPP Supercomputer. *Parallel Computational Fluid Dynamics: Springer*; 2013:311-320.
90. Tolouei, E., C. J. Butler, A. Fouras, K. Ryan, G. J. Sheard, and J. Carberry. Effect of Hemodynamic Forces on Platelet Aggregation Geometry. *Annals of Biomedical Engineering*. 39:1403-1413, 2011.
91. Vahidkhah, K., S. L. Diamond, and P. Bagchi. Platelet Dynamics in Three-Dimensional Simulation of Whole Blood. *Biophysical Journal*. 106:2529-2540, 2014.
92. Vattulainen, I., M. Karttunen, G. Besold, and J. M. Polson. Integration schemes for dissipative particle dynamics simulations: From softly interacting systems towards hybrid models. *The Journal of chemical physics*. 116:3967-3979, 2002.
93. Visser, D. C., H. C. J. Hoefsloot, and P. D. Iedema. Modelling multi-viscosity systems with dissipative particle dynamics. *Journal of Computational Physics*. 214:491-504, 2006.
94. Wang, W., T. G. Diacovo, J. Chen, J. B. Freund, and M. R. King. Simulation of platelet, thrombus and erythrocyte hydrodynamic interactions in a 3D arteriole with in vivo comparison. *PLoS ONE*. 8:e76949, 2013.
95. Wang, W. W. and M. R. King. Multiscale Modeling of Platelet Adhesion and Thrombus Growth. *Annals of Biomedical Engineering*. 40:2345-2354, 2012.

96. Wheeler, M. E., A. C. Cox, and R. C. Carroll. Retention of the Glycoprotein IIB-IIIa Complex in the Isolated Platelet Cytoskeleton - Effects of Separable Assembly of Platelet Pseudopodal and Contractile Cytoskeletons. *Journal of Clinical Investigation*. 74:1080-1089, 1984.
97. Willemsen, S. M., H. C. J. Hoefsloot, and P. D. Iedema. NO-SLIP BOUNDARY CONDITION IN DISSIPATIVE PARTICLE DYNAMICS. *International Journal of Modern Physics C*. 11:881-890, 2000.
98. Wood, N. B., S. J. Weston, P. J. Kilner, A. D. Gosman, and D. N. Firmin. Combined MR imaging and CFD simulation of flow in the human descending aorta. *Journal of Magnetic Resonance Imaging*. 13:699-713, 2001.
99. Wootton, D. M. and D. N. Ku. Fluid mechanics of vascular systems, diseases, and thrombosis. *Annual Review of Biomedical Engineering*. 1:299-329, 1999.
100. Wootton, D. M., C. P. Markou, S. R. Hanson, and D. N. Ku. A mechanistic model of acute platelet accumulation in thrombogenic stenoses. *Annals of Biomedical Engineering*. 29:321-329, 2001.
101. Wu, Z., Z. Xu, O. Kim, and M. Alber. Three-dimensional multi-scale model of deformable platelets adhesion to vessel wall in blood flow. *Philos Trans A Math Phys Eng Sci*. 372, 2014.
102. Xenos, M., G. Girdhar, Y. Alemu, J. Jesty, M. Slepian, S. Einav, and D. Bluestein. Device Thrombogenicity Emulator (DTE) - Design optimization methodology for cardiovascular devices: A study in two bileaflet MHV designs. *Journal of Biomechanics*. 43:2400-2409, 2010.
103. Yamaguchi, T., T. Ishikawa, Y. Imai, N. Matsuki, M. Xenos, Y. F. Deng, and D. Bluestein. Particle-Based Methods for Multiscale Modeling of Blood Flow in the Circulation and in Devices: Challenges and Future Directions. *Annals of Biomedical Engineering*. 38:1225-1235, 2010.
104. Yamaoka, H., S. Matsushita, Y. Shimada, and T. Adachi. Multiscale modeling and mechanics of filamentous actin cytoskeleton. *Biomech Model Mechanobiol*. 11:291-302, 2012.
105. Yazdani, A., M. G. Deng, B. Caswell, and G. E. Karniadakis. Flow in complex domains simulated by Dissipative Particle Dynamics driven by geometry-specific body-forces. *Journal of Computational Physics*. 305:906-920, 2016.
106. Yin, W., Y. Alemu, K. Affeld, J. Jesty, and D. Bluestein. Flow-induced platelet activation in bileaflet and monoleaflet mechanical heart valves. *Ann Biomed Eng*. 32:1058-1066, 2004.
107. Yin, W., S. Gallocher, L. Pinchuk, R. T. Schoepfoerster, J. Jesty, and D. Bluestein. Flow-induced platelet activation in a St. Jude mechanical heart valve, a trileaflet polymeric heart valve, and a St. Jude tissue valve. *Artif Organs*. 29:826-831, 2005.
108. Yin, W., S. K. Shanmugavelayudam, and D. A. Rubenstein. The effect of physiologically relevant dynamic shear stress on platelet and endothelial cell activation. *Thrombosis Research*. 127:235-241, 2011.
109. Yuan, H., C. Huang, J. Li, G. Lykotrafitis, and S. Zhang. One-particle-thick, solvent-free, coarse-grained model for biological and biomimetic fluid membranes. *Phys Rev E Stat Nonlin Soft Matter Phys*. 82:011905, 2010.
110. Zhang, D., D. E. Smith, D. A. Jack, and S. Montgomery-Smith. Numerical evaluation of single fiber motion for short-fiber-reinforced composite materials processing. *Journal of Manufacturing Science and Engineering*. 133:051002, 2011.
111. Zhang, J. F., P. C. Johnson, and A. S. Popel. Red blood cell aggregation and dissociation in shear flows simulated by lattice Boltzmann method. *Journal of Biomechanics*. 41:47-55, 2008.
112. Zhang, J. N., A. L. Bergeron, Q. Yu, C. Sun, L. McBride, P. F. Bray, and J. F. Dong. Duration of exposure to high fluid shear stress is critical in shear-induced platelet activation-aggregation. *Thromb Haemost*. 90:672-678, 2003.
113. Zhang, L. and Y. Deng. A Molecular Model for Platelets at Multiple Scales and Simulations on Supercomputers. SC14: The International Conference for High performance Computing, Network, Storage and Analysis New Orleans, LA; 2014.

114. Zhang, L. L., J. Jasa, G. Gazonas, A. Jerusalem, and M. Negahban. Extracting continuum-like deformation and stress from molecular dynamics simulations. *Computer Methods in Applied Mechanics and Engineering*. 283:1010-1031, 2015.
115. Zhang, N., P. Zhang, W. Kang, D. Bluestein, and Y. Deng. Parameterizing the Morse Potential for Coarse-Grained Modeling of Blood Plasma. *J Comput Phys*. 257:726-736, 2014.
116. Zhang, N., P. Zhang, W. Kang, D. Bluestein, and Y. Deng. Parameterizing the Morse potential for coarse-grained modeling of blood plasma. *Journal of computational physics*. 257:726-736, 2014.
117. Zhang, P., C. Gao, N. Zhang, M. Slepian, Y. Deng, and D. Bluestein. Multiscale Particle-Based Modeling of Flowing Platelets in Blood Plasma Using Dissipative Particle Dynamics and Coarse Grained Molecular Dynamics. *Cellular and Molecular Bioengineering*. 7:552-574, 2014.

Appendix – build, run, and debug LAMMPS

Building LAMMPS on CPU

LAMMPS contains two levels of makefiles, a top-level Makefile and a low-level Makefile.machine. The low-level makefile is called by the top-level makefile. The following code is the essential part of `./src/Makefile`. When typing the command `make comet` in `./src`, the contents of Makefile are executed. The `src` directory contains the C++ source and header files for LAMMPS. Here, “comet” is the name of a machine on which LAMMPS is being built. The Makefile does the following things:

1. Define variables and generate folder `$(objdir)/`;
2. Copy the low-level makefile from `./src/MAKE/MACHINES/Makefile.comet` to `$(objdir)/Makefile`;
3. Execute the low-level makefile in `$(objdir)/Makefile`;
4. Generate the final executable file `lmp_comet`;
5. Use `make clean-all` to remove all built information.

Top-level makefile

```
# LAMMPS multiple-machine Makefile
SHELL = /bin/bash
#.IGNORE:
# Definitions
ROOT =      lmp
EXE =      lmp_$$@
OBJDIR =    Obj_$$@
SRC =      $(wildcard *.cpp)
INC =      $(wildcard *.h)
OBJ =      $(SRC:.cpp=.o)
# Command-line options for mode: exe (default), shexe, lib, shlib
mode = exe
objdir = $(OBJDIR)
.DEFAULT:
    if [ $$@ = "serial" -a ! -f STUBS/libmpi_stubs.a ]; \
```

```

    then $(MAKE) mpi-stubs; fi
test -f MAKE/Makefile.$@ -o -f MAKE/OPTIONS/Makefile.$@ -o \
    -f MAKE/MACHINES/Makefile.$@ -o -f MAKE/MINE/Makefile.$@
if [ ! -d $(objdir) ]; then mkdir $(objdir); fi
$(SHELL) Make.sh style
if [ -f MAKE/MACHINES/Makefile.$@ ]; \
    then cp MAKE/MACHINES/Makefile.$@ $(objdir)/Makefile; fi
if [ -f MAKE/OPTIONS/Makefile.$@ ]; \
    then cp MAKE/OPTIONS/Makefile.$@ $(objdir)/Makefile; fi
if [ -f MAKE/Makefile.$@ ]; \
    then cp MAKE/Makefile.$@ $(objdir)/Makefile; fi
if [ -f MAKE/MINE/Makefile.$@ ]; \
    then cp MAKE/MINE/Makefile.$@ $(objdir)/Makefile; fi
if [ ! -e Makefile.package ]; \
    then cp Makefile.package.empty Makefile.package; fi
if [ ! -e Makefile.package.settings ]; \
    then          cp          Makefile.package.settings.empty
Makefile.package.settings; fi
    cp Makefile.package Makefile.package.settings $(objdir)

ifeq ($(mode),exe)
    @cd $(objdir); \
    $(MAKE) $(MFLAGS) "OBJ = $(OBJ)" "INC = $(INC)" "SHFLAGS ="
\
    "EXE = ../$(EXE)" ../$(EXE)
endif
# Remove machine-specific object files
clean:
    @echo 'make clean-all          delete all object files'
    @echo 'make clean-machine       delete object files for one
machine'
clean-all:

```

```

    rm -rf Obj_*
clean-%:
    rm -rf Obj_$(@:clean-%=) Obj_shared_$(@:clean-%=)
# Create Makefile.list
makelist:
    @$ (SHELL) Make.sh style
    @$ (SHELL) Make.sh Makefile.list

```

Low-level makefile

The low-level makefile specifies the compiler and linker settings.

```

CC =          mpicxx
CCFLAGS =    -Wall -g -O3
DEPFLAGS =   -M
LINK =       mpicxx
LINKFLAGS =  -g -O3

```

In the compilation phase, the following command is executed for each C++ source file,

```
mpicxx -Wall -g -O3 -L. -c *.cpp
```

After the compilation, the object files corresponding to each source file are generated inside \$(objdir) folder. Then these object files are linked together via the command:

```
mpicxx -g -O3 angle_charmm.o angle_cosine.o ... main.o ...
write_restart.o -o ../lmp_comet
```

The dynamic dependencies of executable lmp_comet can be examined by `ldd lmp_comet`, which shows the dependent shared libraries for this executable.

Package management of LAMMPS

The modules for no-slip and inflow/outflow boundary conditions are implemented in package USER-WALRUS, which includes both *.cpp and *.h files. Before building LAMMPS, this package needs to be incorporated by typing the command `make yes-user-walrus`.

The output of this command is:

```

if [ ! -e USER-WALRUS ]; then \
    echo "Package user-walrus does not exist"; \
elif [ -e USER-WALRUS/Install.sh ]; then \
    echo "Installing package user-walrus"; \

```

```
    cd USER-WALRUS; /bin/bash Install.sh 1; cd ..; \  
        /bin/bash Depend.sh USER-WALRUS 1; \  
else \  
    echo "Installing package user-walrus"; \  
    cd USER-WALRUS; /bin/bash ../Install.sh 1; cd ..; \  
        /bin/bash Depend.sh USER-WALRUS 1; \  
fi;
```

If USER-WALRUS/Install.sh exists, it then execute Install.sh, which copies the C++ source file and header file to the ./src directory:

```
cp -p fix_wall_trireflectv3.cpp ..  
cp -p fix_wall_trireflectv3.h ..
```

Then ./src/Depend.sh is executed, which resolves the dependencies between packages.

Running LAMMPS

LAMMPS acts as a molecular dynamics solver, with both input and output in txt format. The input file specifies input parameters for simulation, i.e., number of processors, types of inter-particle potentials, parameter set for these potentials, integration methods, temperature control, output. The input file reads a separate data file, in which the simulation domain is specified, i.e., size of simulation box, atom number, atom type, potential parameters. Once the simulation is finished, LAMMPS writes output data which includes the atom position, velocity, force and other information to enable post-processing.

LAMMPS sample input file

```
# specify number of MPI tasks in each dimension
processors 1 * 1
variable d equal 3.3
# flag to turn on Newton's 3rd law for pairwise and bonded interactions
newton on
# specify dimensionless units
units lj
# specify three dimensional simulation
dimension 3
# set up boundary types
boundary p s p
# parameters for building neighbor list
neighbor 0.2 multi
neigh_modify page 1000000 one 100000 every 1 delay 0
# set up atom, pair, bond, angle, dihedral, improper styles
atom_style molecular
pair_style hybrid/overlay morse 1.0 lj/cut 1.0 dpd 1.0 1.6 34387
dpd/tstat 1.0 1.0 1.6 34387
pair_modify mix arithmetic
bond_style harmonic
angle_style hybrid harmonic class2
```

```

dihedral_style charmm
improper_style harmonic
# read data file
read_data ./dump3.3/restart.4500K.data
# set up pairwise potential coefficients, 15 atom types
pair_coeff 1 1 morse 5.0 8.33 0.42
pair_coeff 1 1 lj/cut 0.1 0.4
pair_coeff 2 2 lj/cut 0.025 0.1875
pair_coeff 3 3 lj/cut 0.025 0.1836
pair_coeff 2 3 lj/cut 0.025 0.1875
pair_coeff 4 4 lj/cut 0 0.05
pair_coeff 5 5 lj/cut 0.1 0.05
pair_coeff 6 6 lj/cut 0.1 0.05
pair_coeff 7 7 lj/cut 0.1 0.05
pair_coeff 8 8 lj/cut 0.1 0.05
pair_coeff 9 9 lj/cut 0.1 0.05
pair_coeff 10 10 lj/cut 0.1 0.05
pair_coeff 11 11 lj/cut 0.1 0.05
pair_coeff 12 12 lj/cut 0.1 0.05
pair_coeff 13 13 lj/cut 0.1 0.05
pair_coeff 14 14 lj/cut 0 0.05
pair_coeff 15 15 dpd 25 67.5
pair_coeff 1 2*14 lj/cut 0.1 0.21
pair_coeff 2*3 4*13 lj/cut 0.1 0.65
pair_coeff 2*3 14 lj/cut 0.1 0.21
pair_coeff 1 15 morse 15.0 8.75 0.42
pair_coeff 4*14 15 dpd 0 0
#hybrid potential
pair_coeff 2*3 15 lj/cut 6 0.6
pair_coeff 2*3 15 dpd/tstat 67.5
# dihedral change for membrane, set to 0
dihedral_coeff 22 0 2 180 0

```



```

comm_modify      vel yes cutoff 5.0
# assign atoms to groups
group            FLOW      type 15
group            PLAT      type 1 2 3 4 5 6 7 8 9 10 11 12 13 14
group            core      type 4 8 13
group            noncore   type 1 2 3 5 6 7 9 10 11 12 14
group            NVE       union FLOW noncore
group            mem       type 2 3
# include extra fixes, such as no-slip BC
include          fixes.PL-Blood
fix SAFE FLOW wall/reflect ylo -47 yhi 47 units box
# integration timestep
timestep 5.0E-7
# integration method and temperature control
fix INTE NVE nve
fix TEMPCTRL NVE temp/rescale 1 1.05 1.06 0.01 1
fix INTECORE core rigid single
# set up thermo output
thermo_style custom step cpu temp vol epair ke pe etotal
thermo_modify lost warn
thermo 100
# set up dynamic bond between membrane and protrusible filament
#group TIPMEM union TIP1 IMEM
# t = [ bondtype ] type of bonds to create/break
# f = [ Nevery   ] attempt bond creating/breaking every this many
steps
#variable t equal 15
#variable f equal 100
#variable Rmin equal 0.5
#fix FM25 TIPMEM bond/create ${f} 2 5 $98 ${t} prob 0.5 85786
#fix FM26 TIPMEM bond/create ${f} 2 6 $98 ${t} prob 0.5 85786
#fix FM27 TIPMEM bond/create ${f} 2 7 $98 ${t} prob 0.5 85786

```

```

# fix FM211 TIPMEM bond/create ${f} 2 11 $98 ${t} prob 0.5 85786
#fix FM35 TIPMEM bond/create ${f} 3 5 $98 ${t} prob 0.5 85786
#fix FM36 TIPMEM bond/create ${f} 3 6 $98 ${t} prob 0.5 85786
#fix FM37 TIPMEM bond/create ${f} 3 7 $98 ${t} prob 0.5 85786
# fix FM311 TIPMEM bond/create ${f} 3 11 $98 ${t} prob 0.5 85786
# Rmax from 1.2 to 2.0
# fix 99 TIPMEM bond/break ${f} ${t} 2.0 prob 1.0 49829
#####
#####
fix FIXBALANCE all balance 200 1.2 shift y 20 1.05
# set up simulation loops
# start loop function...
label loop
variable ii loop 5
variable i equal $50+45
log dump${d}/log.${i}00K
print "input : loop = ${i}"
# inner, outer, inner-outer membrane
variable b08 equal 50000
bond_coeff 8 ${b08} 0.19
bond_coeff 9 ${b08} 0.20
bond_coeff 10 ${b08} 0.19
# bond_13: membrane for small filament 34 and 43 and 7 and 12
variable b13 equal 10000
bond_coeff 13 ${b13} 0.4
# bond_14: bonds between filament_34 and filament_43 and
membrane...
variable b14 equal 50000
variable r14 equal 0.40
bond_coeff 14 ${b14} ${r14}
# bond_15: membrane for large filament 19...
variable b15 equal 10000

```

```

variable r15 equal 0.4
bond_coeff          15 ${b15} ${r15}
# supportive filaments
variable r11 equal 0.5
variable r12 equal 0.315
bond_coeff          11 2000000    ${r11}
bond_coeff          12 2000000    ${r12}
variable r1 equal 0.093*(2.5+$50*0.1)
variable r4 equal 0.0865*(2.5+$50*0.1)
bond_coeff          1      1.46018e+07 ${r1}
bond_coeff          4      2.01505e+07 ${r4}
print "input  : bond_coeff    1  1.46018e+07  ${r1}"
print "input  : bond_coeff    4  2.01505e+07  ${r4}"
print "input  : bond_coeff    8  ${b08}  0.19"
print "input  : bond_coeff    9  ${b08}  0.20"
print "input  : bond_coeff   10  ${b08}  0.19"
print "input  : bond_coeff   11  50000   ${r11}"
print "input  : bond_coeff   12  50000   ${r12}"
print "input  : bond_coeff   13  ${b13}  0.20"
print "input  : bond_coeff   14  ${b14}  ${r14}"
#print "input  : bond_coeff   15  ${b15}  ${r15}"
# # Angles
variable k27 equal 675
variable k28 equal 1080
# modify angle coeffs for filament protrusion
# angle coeff
angle_coeff 1          harmonic 702.1541798          108
angle_coeff 2          harmonic 702.1541798          108
angle_coeff 3          harmonic 675.1492116          120
angle_coeff 4          harmonic 720.3842213          108.5
angle_coeff 5          harmonic 720.3842213          114
angle_coeff 6          harmonic 459.101964           123

```

angle_coeff 7	harmonic	472.6031978	117
angle_coeff 8	harmonic	479.355065	110.1
angle_coeff 9	harmonic	675.1492116	109.5
angle_coeff 10	harmonic	675.1492116	109.5
angle_coeff 11	harmonic	472.6031978	111
angle_coeff 12	harmonic	594.1318064	109.5
angle_coeff 13	harmonic	1080.238739	116.5
angle_coeff 14	harmonic	675.1492116	107
angle_coeff 15	harmonic	675.1492116	107
angle_coeff 16	harmonic	945.2088963	113.5
angle_coeff 17	harmonic	695.4023126	108
angle_coeff 18	harmonic	590.080686	110
angle_coeff 19	harmonic	1080.238739	121
angle_coeff 20	harmonic	1080.238739	122.5
angle_coeff 21	harmonic	540.1193693	118
angle_coeff 22	harmonic	1350.298423	124
angle_coeff 23	harmonic	675.1492116	120
angle_coeff 24	harmonic	1080.238739	116.5
angle_coeff 25	harmonic	675.1492116	107
angle_coeff 26	harmonic	0	180
angle_coeff 27	harmonic	$\{k27\}$	180
angle_coeff 28	harmonic	$\{k28\}$	180
angle_coeff 29	harmonic	$\{k27\}$	180
angle_coeff 30	harmonic	675.149	180
angle_coeff 31	harmonic	50000	180
angle_coeff 32	harmonic	300000	180
angle_coeff 33	harmonic	1080.238739	180
angle_coeff 34	harmonic	20000	180
angle_coeff 35	class2	180	300000
0		300000	
angle_coeff 35	class2	bb	0 0 0

```

angle_coeff 35                class2  ba                0 0 0
0
print "input : angle_coeff    34 20000  180"
print "input : angle_coeff    35 180 20000 0 20000 bb 0 0 0 ba 0
0 0 0"
print "input : angle_coeff 27  harmonic ${k27}                180"
print "input : angle_coeff 28  harmonic ${k28}                180"
print "input : angle_coeff 29  harmonic ${k27}                180"
# modify dihedral coeffs for filament protrusion
# # Dihedrals
variable l equal 21600
# dihedral coeff
dihedral_coeff 16 ${l} 1 0 0
dihedral_coeff 19 ${l} 1 0 0
dihedral_coeff 20 ${l} 1 0 0
dihedral_coeff 21 ${l} 1 0 0
# dihedral output
print "input  : dihedral_coeff 16 ${l} 1 0 0"
print "input  : dihedral_coeff 19 ${l} 1 0 0"
print "input  : dihedral_coeff 20 ${l} 1 0 0"
print "input  : dihedral_coeff 21 ${l} 1 0 0"
print "output : dump      = dump${d}/dump.${i}00K"
print "output : restart = dump${d}/restart.${i}00K"
# set up output
# # platelet: 5 frames per 100K-steps = 20K-step/frame...
# # all      : 5 frames per 100K-steps = 20K-step/frame...
dump ICDUMPA FLOW  custom 8000 dump${d}/dump_flow.${i}00K  id type
x y z
dump ICDUMPP PLAT  custom 8000 dump${d}/dump_plat.${i}00K  id type
x y z vx vy vz
run 40000
undump ICDUMPA

```

```
undump ICDUMPP
write_restart dump${d}/restart.${i}00K
next i
jump SELF loop
print "all done successfully."
print "-----"
```

LAMMPS sample data file

number of atoms, bonds, angles, dihedrals, impropers, and corresponding types

680707 atoms

15 atom types

275199 bonds

15 bond types

78540 angles

35 angle types

188308 dihedrals

22 dihedral types

4956 impropers

3 improper types

dimension of simulation box

-2.2500000000000000e+01 2.2500000000000000e+01 xlo xhi

-4.4576805953714455e+01 4.4765700255483083e+01 ylo yhi

-2.2500000000000000e+01 2.2500000000000000e+01 zlo zhi

atom mass

Masses

1 0.0381

2 0.0381

3 0.0381

4 0.0286

5 0.0333

6 0.0286

7 0.0286

8 0.0286

9 0.0381

10 0.0286

11 0.0286

12 0.0024

13 0.0286

14 0.0286

15 1

bond coeffs

Bond Coeffs # harmonic

1 1.46018e+07 0.093

2 1.29956e+07 0.095

3 1.92744e+07 0.069

4 2.01505e+07 0.0865

5 3.62126e+07 0.077

6 2.56992e+07 0.062

7 2.35382e+07 0.065

8 30000 0.19

9 30000 0.2

10 30000 0.19

11 10000 0.5

12 50000 0.315

13 500 0.2

14 10000 0.5

15 500 0.2

dihedral coeffs

Dihedral Coeffs # charmm

1 2.7 1 180 0

2 2.7 1 180 0

3 33.75 2 180 0

4 24.3 1 0 0

5 33.75 2 180 0

6 8.1 1 0 0

7 8.1 1 0 0

8 18.9 1 0 0

9 33.75 2 180 0

10 33.75 2 180 0

11 0 1 0 0


```

12 2.7 3 0 0
13 2.7 3 0 0
14 1.35 3 0 0
15 2.7 1 180 0
16 21600 1 0 0
17 33.75 2 180 0
18 8.1 1 0 0
19 21600 1 0 0
20 21600 1 0 0
21 21600 1 0 0
22 0 2 180 0
# improper coeffs
Improper Coeffs # harmonic
1 270.05 0
2 1620.32 0
3 1296.25 0
# position and velocity of atoms
Atoms # molecular
668370 0 15 -1.8812304742882894e+01 -4.3583499158733261e+01 -
2.2356008079745905e+01 -10 0 0
# topological structure list for bonded potentials
Bonds
1 9 81475 81478
Angles
1 8 24137 24139 24140
Dihedrals
1 22 49846 50156 50158 50472
Impropers
1 2 24147 24135 24149 24148

```

Command for running LAMMPS

A bash script is written to submit jobs to the queue, which specifies the job name, number of nodes, number of MPI tasks per node, the queue name, the proposed running time, the email alert upon job finish, command to run the job. To execute LAMMPS, first type the executable name, then type the input file name.

```
#!/bin/bash
#SBATCH -J name          # job name
#SBATCH -o name.o%j      # output and error file name (%j expands
to jobID)
#SBATCH --nodes=4
#SBATCH --ntasks-per-node=24 # total number of mpi tasks requested
#SBATCH -p compute       # queue (partition) -- normal,
development, etc.
#SBATCH -t 48:00:00      # run time (hh:mm:ss) - 1.5 hours
#SBATCH --mail-user=gaochaodct@hotmail.com
#SBATCH --mail-type=begin # email me when the job starts
#SBATCH --mail-type=end   # email me when the job finishes
ibrun lmp_10Aug15_IOBC_small -in in.periodic
```

Debugging LAMMPS

LAMMPS debugging is performed using a parallel debugger Allinea-DDT which is able to point out the location of memory error.

The command to launch this debugger is:

```
ddt -offline report.html -n 4 ./lmp_10Aug15_IOBC_small -in
in.hybrid
```

A HTML file is generated that records the error information.

▼ Stacks

Processes	Function	Source
... (48 total)	main (main.cpp:31)	▸ lammps->input->file();
... (48 total)	LAMMPS_NS::Input::file (input.cpp:241)	▸ if (execute_command()) {
... (48 total)	LAMMPS_NS::Input::execute_command (input.cpp:657)	▸ else if (!strcmp(command,"fix")) fix();
... (48 total)	LAMMPS_NS::Modify::add_fix (modify.cpp:779)	▸ fix[ifix] = fix_creator(lmp,narg,arg);
... (48 total)	LAMMPS_NS::Modify::fix_creator(LAMMPS_NS::FixWallTriReflectv3> (modify.cpp:834)	▸ return new T(lmp,narg,arg);
... (48 total)	LAMMPS_NS::FixWallTriReflectv3::FixWallTriReflectv3 (fix_wall_trireflectv3.cpp:72)	▸ mp[0] = atof(arg[iarg+13]);
... (48 total)	atof (stdlib.h:281)	▸ return strtod (_nptr, (char **) NULL);
... (48 total)	__strtod_l_internal	